Factors Affecting Recognition and Chemical Reactivity at the Macromolecular Scale

A DISSERTATION
SUBMITTED TO THE FACULTY OF THE GRADUATE SCHOOL
OF THE UNIVERSITY OF MINNESOTA
BY

William C. Isley III

IN PARTIAL FULFILLMENT OF THE REQUIREMTNS
FOR THE DEGREE OF
DOCTOR OF PHILOSOPHY

Professor Christopher J. Cramer

July 2015

Acknowledgements

There a great many individuals that I would like to thank for their support during my pursuit of a doctoral degree. First and foremost, I would like to express my deepest gratitude to my doctoral advisor, Prof. Christopher J. Cramer. Without his sage advice and contagious enthusiasm, none of the work in this thesis would have been possible. Under his mentorship I have been provided opportunities to grow as a scientist and person, for which I am extremely grateful. If I have come away with half of the poise, focus, and knowledge that Chris possesses, it would be a monumental personal achievement.

I will also take this opportunity to thank Prof. Laura Gagliardi for her mentorship, especially the stimulating discussions and for providing the opportunity to get my feet wet in chemistry at the University of Minnesota. I would also like to thank my other collaborators and instructors within the faculty of the University of Minnesota, especially Profs. Philippe Bühlmann, William Pomerantz, Ilja Siepmann, and Donald Truhlar, for the experience and lessons they have left with me. For starting me off on the path of chemistry at Lafayette College, I would like thank the guidance of Profs. Kenneth Haug, Yvonne Gindt, and Chip Nataro.

I would like to thank all of my collaborators from outside the University of Minnesota for the very useful discussions, especially Drs. Eric Olsen, Salvatore Zarra, Rana Bilbeisi, Pritha Gosh, Michael Katz,. Tanya Ronson, Peilin Liao, and Profs. Jonathan Nitschke, Joseph Mondloch, Omar Farha, Joseph Hupp, and Randall Snurr. I cannot say how much I valued my brief, by extremely insightful, internship at Proctor and Gamble Corp. I benefited greatly from working with Drs. Casey Kelly, Bill Laidig, Lucy Gildea, and Yogita Manti.

I owe a debt of gratitude to current and past Cramer group members for all the scientific help, friendship, and conversation that we've had over the past several years. Thank you (in no particular order) to Pere, Zahid, David, Stuart, Aaron, Ashley, Kelly, Samat, Hugo, Aga, Busra, Soumen, Josh, Manuel, Christine and Andreas. I would like to offer special thanks to Pere Miro, Bess Vlaisavljevich, Nora Planas, Allison Dzubak, and Zahid Ertem for putting up with all of those pesky questions.

Finally, thanks go to my family and friends. Time spent with you was hardly time spent at all. Thank you Becca, Mayank, Andy, Eric, Di, Laura, Aaron, Bess, Pere, Nora, Toni, Allison, Josh, Chad, Ben, Scott, Eric, Chris, Jesse, Jeff, Evgenii, David, and Manuel for the sharing the distractions that keep you focused during the work day.

I would particularly like to thank my parents and sisters for all that they have done to help me along the way. You're the bright inspiration that drives me forward. It has been a very long journey, and I owe it all to you. Your support and care have let me excel to achieve my doctoral dreams. You all are the best support I could ask for!

Abstract

As chemists characterize molecular systems in greater detail, it becomes clear that some observables can only be properly studied at the macromolecular scale. However, elucidating the physical principles behind such phenomena as molecular recognition or chemical reactivity can be difficult when moving into the macromolecular regime. The objective of this work is to provide insights and predictions to complement experimental undertakings. The work is divided into two categories: 1) modeling molecular recognition through prediction of intermolecular interactions with highly accurate methods and 2) the modeling of chemical reactivity.

The separation of N_2 and CH_4 is particularly pertinent for the natural gas industry, and improved materials for performing this separation would provide an enormous cost savings. This work is focused on the prediction of a new material capable of performing this separation. Through application of multiple tiers of quantum chemical methods, and comparison to similar known experimentally synthesized materials, a novel material is predicted to effect the separation of N_2 and CH_4 through selective binding of N_2 to an open vanadium metal site.

A particularly valuable tool for monitoring target delivery or guest encapsulation in macromolecular systems is an easily observed signal that indicates the status of a host-guest complex. Guest complexation can alter the observable properties of the host, including the spin crossover properties of a host macromolecule. Particular care was taken to correlate guest recognition to changes in paramagnetic NMR chemical shifts induced in the host system.

The monitoring of subtle changes in a protein's environment is a challenging and complex problem; however, the observation of ligand complexation in biomolecular systems is extremely important in the design of new medicinal therapeutic drugs. This work aims to develop a quantum chemical method to assist experimental assignment of challenging ^{19}F NMR spectra in proteins. The importance of accurately modeling the hydration environment is extremely critical for accurate comparison to experimental measurements.

Selective detection of chemical impurities is an attractive capability to have for any chemical process. A key impurity in industrially synthesized explosive TNT is DNT. Given the high prevalence of DNT in TNT, detection of DNT through electrochemistry is a useful sensor for explosives. This work characterizes the mechanism of DNT electrochemical reduction

A new material was found to rapidly catalyze the decomposition of extremely toxic chemical warfare agents. The macromolecular metal organic framework NU-1000 was demonstrated to be extremely effective in catalyzing the hydrolysis of phosphoester based chemical warfare agents. Predictive computations were performed on a nerve agent simulant DMNP, and toxic nerve agents GD (Soman) and VX agents, uncovering the key role that the metal nodes of NU-1000 play in activation of the phosphoester bonds for hydrolytic attack.

Table of Contents

List of Tables

List of Figures and Schemes

Figures

Schemes

List of Abbreviations

BET	:	Bromodomain and extra terminal domain
CASPT2	:	Complete active space second-order perturbation theory
CASPT2-CP	:	Complete active space second-order perturbation theory with counterpoise corrections
CM5	:	Charge model 5
BNPP	:	Bis(4-nitrophenyl) phosphate
DAAP	:	Dialkylaminopyridine
DENP	:	Diethyl 4-nitrophenyl phosphate
DFT	:	Density functional theory
DMNP	:	dimethyl 4-nitrophenyl phosphate
DNA	:	deoxyribonucleic acid
DNF	:	2,4-dinitrotoluene
DRIFTS	:	Diffuse reflectance infrared Fourier transform spectroscopy
dobdc	:	2,5-dioxido-1,4-benzenedicarboxylate
ETS-NOCV	:	Extended transition state - natural orbitals for chemical valence
FC	:	Fermi contact
GD	:	Soman (*O*-pinacolyl methylphosphonofluoridate)
GGA	:	Generalized gradient approximation
HF	:	Hartree Fock
HFC	:	Hyperfine coupling
HK	:	Hohenberg Kohn
HS	:	High spin
HSQC	:	Heteronuclear single quantum coherence
KS	:	Kohn-Sham
LDA	:	Local density approximation

LPNO-CCSD	:	Local-pair natural-orbital coupled cluster theory with single and double excitations
LS	:	Low spin
meta-GGA	:	meta-Generalized gradient approximation
MOF	:	Metal organic framework
MSD	:	Mean signed deviation
MUD	:	Mean unsigned deviation
NBO	:	Natural bond order
NMR	:	Nuclear magnetic resonance
PC	:	Pseudocontact
PMPA	:	pinacolyl methylphosphate
PrO	:	Protein observed
PrOF	:	Protein observed fluorine
PXRD	:	Powder X-ray diffraction
RNA	:	Ribonucleic acid
SCO	:	Spin-crossover
SD	:	Spin-dipole
SO	:	Spin-orbit
$TBAPy^{4-}$	:	Tetratopic 1,3,6,8(*p*-benzoate)pyrene linkers
TMS	:	Tetramethylsilane
TNT	:	2,4,6-trinitrotoluene
TOF	:	Turnover frequency
VX	:	*O*-ethyl S-[2-ethyl] methylphosphonothioate
VT	:	Variable temperature
WTF	:	Wave function theory
XC	:	Exchange-correlation
ZFS	:	Zero field splitting

Preface

Citations from previously published work in this thesis are as follows:

Chemical Recognition at the Macromolecular Scale

2.1 Design of a Metal – Organic Framework with Enhanced Back Bonding for the Separation of N2 and CH4

Adapted with permission from:

Lee, Kyuho; Isley III, William C.; Dzubak, Allison; Verma, Pragya; Stoneburner, Samuel J.; Lin, Li-Chiang; Howe, Joshua D.; Block, Eric D.; Reed, Douglas A.; Hudson, Matthew R.; Brown, Craig M.; Long, Jeffery R.; Neaton, Jeffery B.; Smit, Berend; Cramer, Christopher J.; Truhlar, Donald G.; Gagliardi, Laura

J. Am. Chem. Soc. **2014**, 136 (2), pp 698-704.

Link: http://dx.doi.org/10.1021/ja4102979

2.2 Predicting Paramagnetic ^{1H} NMR Chemical Shifts and State-Energy Separations in Spin-Crossover Host-Guests Systems

Reproduced by permission of the PCCP Owner Societies

Isley III, William C.; Zarra, Salvatore; Carlson, Rebecca K.; Bilbeisi, Rana A.; Ronson, Tanya K.; Nitschke, Jonathan R.; Gagliardi, Laura; Cramer, Christopher J.

Phys. Chem. Chem. Phys. **2014**. 16, pp 10620-10628.

Link: http://dx.doi.org/10.1039/C4CP01478B

Chemical Reactivity at the Macromolecular Scale

3.1 Electrochemical Reduction of 2,4-Dinitrotoluene in Aprotic and pH-Buffered Media

Adapted with permission from:

Olson, E.; Isley III, W.C.; Brennan, J.; Cramer, C.; Buhlmann, P.

J. Phys. Chem. C, **2015**.*119* (23), pp 13088-13097.

Link: http://dx.doi.org/1 0.1021/acs.jpcc.5b02840

3.2 Decomposing Chemical Warfare Agents Utilizing Metal–Organic Frameworks

Adapted with permission from:

Mondloch, Joe; Katz, Michael J.; Isley III, W. C.; Gosh, Pritha; Liao, Peilin; Bury, Wojciech; Wagner, George W.; Hall, Morgan G.; DeCoste, Jared B.; Peterson, Gregory W.; Snurr, Randall Q.; Cramer, Christopher J.; Hupp, Joseph T.; Farha, Omar K.

Nature Materials. **2015**, 14, pp 512-516.

Link: http://dx.doi.org/10.1038/NMAT4238

Chapter 1

Introduction

1.1 Overview

The ability to selectively control the course of chemical processes is essential for many modern scientific technologies. Chemical separations rely on the principles of selectivity to achieve the necessary isolation of the desired chemical from the remaining constituents. Effective separations are essential for the purification of fuels, alcohol, and other commonly used products. In the absence of selectivity, chemical separations would be extremely difficult, industrial syntheses could yield costly, dangerous, or unintended products, and even the regulation of biological functions would be impossible. It is clear that separations and chemical reactions could be improved with greater selectivity; however, many of the key principles underlying selective chemistry remain unexplored. Throughout my thesis work in chemistry, I have attempted to provide insight into chemical selectivity, including: the prediction of a new selective material for gas separations, using predictive spectroscopy to elucidate physical relations in host-guest binding selectivity and in fluorochemical protein environments, selective sensing of chemical impurities, and the discovery of a material for selective nerve agent decomposition. The fundamentals of the systems described below may vary (gases interacting with solids, or solutes interacting in solution), but the research collected in this thesis shares a common interest in understanding the fundamental way in which guests interact with a macromolecular system.

One way to improve our understanding of selective chemistry is to study the physical components of chemically selective systems, and then identify which inter-fragment interactions are responsible for strength and selectivity. My research has chiefly used modern quantum chemical methodologies to study the physical properties of a chemical system. Modern quantum chemistry is well suited to study an approximate, static *model* system that is limited to the system's critical components. One key feature for the use of highly accurate quantum chemical methods is the ability to decompose chemical interactions into fundamental physical interactions and this can provide greater insight into selectivity. However, the challenge with quantum chemical models is that model systems are static, and limited to a few dozens of atoms. This is a critical obstacle to overcome in the treatment of a macromolecular system, which are

typically much larger than can be treated holistically with quantum methods. This leads to the non-trivial role of scientists in choosing the appropriate model to accurately represent the macromolecular system, while still being able to accurately predict the material's properties.

Much of my thesis work applies predictive modeling methods to address problems or questions that experiments cannot easily answer. Herein, I will discuss several projects relating to the chemical recognition and catalytic selectivity in macromolecular systems. Now let us discuss the necessary theoretical framework which has been used study these systems.

1.2 Computational Methods

1.2.1 Density Functional Methods

The advent of computational chemistry gave scientists a molecular camera to examine the finest details of chemistry. The groundwork was laid by quantum mechanics, particularly via the time independent Schrodinger Equation

$$\hat{H}\Psi = E\Psi \qquad (1.2.1)$$

where $\hat{H}$ is the Hamiltonian operater that returns the energy eigenvalue E of a system described by a wavefunction Ψ. However, a complete *a priori* formulation of an electronic system is exceedingly difficult for molecular systems; one can approximate this through the use of density functional theory (DFT). While Ψ contains all of the information about a system, working with Ψ can be computationally challenging given that is contains $4N$ variables, where N is the number of electrons. We can dramatically reduce the cost by considering the electron probability density

$$\rho(r) = \Psi^*(r)\Psi(r) \qquad (1.2.2)$$

which depends only on three coordinates, or six coordinates if we consider alpha and beta spin densities separately. The Hohenberg-Kohn (HK) theorems and the Kohn-Sham (KS) approach established the foundation for utilizing the electronic density instead of the wavefunction to determine electronic structure and properties.[1]

Within the KS density functional framework, one approximates a fictitious system of non-interacting electrons. This crucial approximation allows for the expression of the Hamiltonian operator as a sum of one electron operators, and then accounting for the difference from the real system with a correction term.

$$E[\rho(r)] = T_{ni}[\rho(r)] + V_{ne}[\rho(r)] + V_{ee}[\rho(r)] + \underbrace{\Delta T[\rho(r)] + \Delta V[\rho(r)]}_{E_{xc}} \qquad (1.2.3)$$

where the terms refer respectively to the kinetic energy (T) of the non-interacting system, the potential energy (V) of the classical nuclear-electron and electron-electron interaction potentials, and the correction terms to the kinetic energy of an interacting density and to the

electron-electron potential of a self-interacting density, respectively. The correction terms can be described as the exchange-correlation (XC) energy E_{xc}, which is often approximated in a semiempirical fashion since the exact formulation is unknown. Since the exchange-correlation term contains the residual part of the true kinetic energy, non-classical form of the self-interaction correction, and the exchange and correlation interactions, there have been numerous attempts at formulating exchange correlation functionals. The exchange and correlation terms come from the instantaneous effects that the many electron system have on each other through the exchange effect of indistinguishable quantum particles and correlation of simultaneously moving electrons experiencing Coulomb interactions.

Current exchange-correlation functionals are chiefly of the following varieties: local, gradient corrected, kinetic energy corrected, and hybrid functionals. Within the local density approximation (LDA), the functional only has spatial dependence on the density. The use of LDA has significantly depreciated since its inception in favor of the more accurate generalized gradient approximation (GGA). The gradient corrected functionals include additional dependence on the gradient of the density. These are commonly used functionals, and examples include PBE or BLYP. The meta functionals additionally include functional dependence on the up and down spin kinetic energy densities. These functionals are among the most complex of available functionals; an example of a meta-GGA functional is M06L. A hybrid functional includes some fraction of exact Hartree-Fock (HF) exchange ranging from 10% to 100% (depending on the functional). For example, the widely used B3LYP functional is a hybrid GGA functional with 20% HF exchange or the hybrid meta-GGA functional M06 with 27% HF exchange.

There are currently a large variety of functionals available in the literature, and without some guidance one can quickly become overwhelmed by choices. Functionals were chose in this work by examining the functional performance for a given application. When previous performance was unknown, additional benchmarking was performed to compare modeling results to experimental measurements.

1.2.2 Computation of Nuclear Magnetic Resonance[†]

Diamagnetic NMR. In nuclear magnetic resonance (NMR), one can observe atomistic detail in molecular and macromolecular systems. Each atom's unique magnetic environment generated by moving charges of the local electronic and nuclear structure, gives rise to radio frequency resonances for nuclear spin flips in the presence of a magnetic field. This is called the nuclear Zeeman effect, and has an energy splitting

$$\Delta E = \hbar \gamma_I (B_0 - B_e) \qquad (1.2.4)$$

where the nuclear spin splitting energy is described by ΔE, $\hbar$ is the Planck constant over 2π, γ_I is the gyromagnetic frequency of nucleus I, B_0 is the applied magnetic field and B_e is the local magnetic field. The strength of the B_e at a nucleus opposing the applied magnetic field is called the chemical shielding. These resonance frequencies are dependent on the strength of the applied magnetic field, so there is a standardized way to report this called the chemical shift

$$\delta = \frac{\nu_{sample} - \nu_{ref}}{\nu_{ref}} \qquad (1.2.5)$$

where ν_{sample} is the resonance frequency of your sample's nucleus in Hz, and ν_{ref} is the resonance frequency of a reference nucleus in Hz. The denominator is in units of MHz, giving rise to units of ppm typically reported.

Theoretically, one can predict the local magnetic field at a nucleus opposing an applied magnetic field (termed the orbital chemical shielding σ_{orb}^{iso}) by taking the second mixed derivative with respect to the nuclear magnetic moment and the magnetic field. Since solution based experimental measurements only measure the isotropic contributions, we do not have to consider the anisotropic contributions to the chemical shielding tensor. Given that σ_{orb}^{iso} is an

---

[†] Parts of this section are Reproduced by permission of the PCCP Owner Societies

Isley III, William C.; Zarra, Salvatore; Carlson, Rebecca K.; Bilbeisi, Rana A.; Ronson, Tanya K.; Nitschke, Jonathan R.; Gagliardi, Laura; Cramer, Christopher J.

Phys. Chem. Chem. Phys. **2014**. 16, pp 10620-10628.

Link: http://dx.doi.org/10.1039/C4CP01478B

absolute chemical shielding and must be referenced relative to a known compound, the observable orbital chemical shift becomes

$$\delta_{orb} = \sigma_{ref}^{iso} - \sigma_{orb}^{iso} \quad (1.2.6)$$

where σ_{ref}^{iso} is the isotropic chemical shielding of a reference compound, typically tetramethylsilane (TMS) for ^{1}H and ^{13}C with a δ_{exp} = 0 ppm. For ^{19}F NMR, trifluoroacetate (δ_{exp} = -76.55 ppm relative to $CFCl_3$) is typically used as the reference compound.

Paramagnetic NMR. When unpaired electronic spin density is present in a paramagnetic molecular system, this gives rise to a magnetic dipole, and Zeeman orbital contribution to the chemical shift is no longer the dominant term. The presence of the magnetic dipole requires that additional terms must be accounted for to accurately predict the NMR chemical shift of a paramagnetic system. The paramagnetic NMR chemical shift can be approximated[2] for S = ½ as

$$\delta = \delta_{orb} + \delta_{FC} + \delta_{SD} \quad (1.2.7)$$

where the three contributors to the total isotropic chemical shift are an orbital term, computed analogously as for diamagnetic systems, a Fermi contact term, and a spin–dipole term. The Fermi contact (FC) shift originates from the Fermi contact interaction between the nuclear magnetic moment and the average spin density at the nucleus.[2] The spin–dipole (SD) term derives from the dipolar interaction between the magnetic moment of unpaired electron density and the nuclear magnetic moment of interest. The spin-dipole term has unfortunately been termed the "pseudocontact" shift; and has been the cause of some confusion in the literature. The pseudocontact interaction originates from the spin-orbit correction to the FC interaction.

For an S = ½ system, the absolute chemical shielding can be expressed as

$$\boldsymbol{\sigma}_K = \boldsymbol{\sigma}_{K,orb} - \frac{S(S+1)}{3k_BT}\frac{\mu_B}{g_{N,K}\mu_{N,K}}\boldsymbol{g}\cdot\boldsymbol{A}_K^T \quad (1.2.8)$$

where $\boldsymbol{\sigma}_{K,orb}$ is the orbital shielding for nuclei K, S is the effective spin, μ_B and $\mu_{N,K}$ are the Bohr and nuclear magneton, respectively, $g_{N,K}$ is the nuclear *g*-value of nucleus K (note that the nuclear *g*-value is commonly substituted for the nuclear gyromagnetic ratio $\gamma_K = \mu_{N,K}g_{N,K}/\hbar$), k_B is the Boltzmann constant, T is the temperature, the $\boldsymbol{g}$ tensor is the electronic *g*-tensor, and A_K is the hyperfine coupling tensor at nucleus K, the T superscript denotes the transpose. The

non-relativistic hyperfine coupling tensor can be separated into the isotropic Fermi contact term, and the anisotropic dipolar coupling term. There are other terms arising from spin-orbit coupling (SOC) which can be separated into the isotropic pseudocontact (PC) term, the anisotropic symmetric and anti-symmetric contributions.

Since solution based experimental measurements only measure the isotropic contributions, by removing the anisotropic and anti-symmetric terms equation 2 can be reduced to (omitting K for simplicity)

$$\sigma^{iso} = \sigma_{orb}^{iso} - \frac{S(S+1)}{3k_BT}\frac{2\pi\mu_B}{g_N\mu_N}\left[g_{iso}A_{FC} + g_eA_{PC} + \frac{1}{3}\mathrm{Tr}(\widetilde{\boldsymbol{\Delta g}} \cdot \boldsymbol{A}_{SD})\right] \quad (1.2.9)$$

where A_{FC} is the isotropic Fermi contact hyperfine coupling constant, A_{PC} is the isotropic pseudocontact hyperfine coupling constant, and the remaining isotropic term is taken from the tensor product between the g-tensor and the spin-dipolar hyperfine coupling tensor (since $\boldsymbol{A}_{SD}$ is symmetric, the transpose idempotent).

For isotropic systems $3d$ metal systems,[3-5] the Fermi contact term is presumed to massively dominate the pseudocontact and spin-dipolar contributions and thus these spin-orbit and anisotropic contributions are neglected. The pseudocontact term δ_{PC} has previously been shown[3, 4, 6, 7] to be negligibly small in Co- and Fe-containing systems similar to those studied later in this work. Thus the computed absolute chemical shift becomes

$$\sigma^{iso} = \sigma_{orb}^{iso} - \frac{S(S+1)}{3k_BT}\frac{2\pi\mu_B}{\gamma}g_{iso}A_{FC} \quad (1.2.10)$$

where γ is the gyromagnetic ratio for nucleus K, g_{iso} is the isotropic g-factor, μ_B is the Bohr magneton, $A_{FC}$is the isotropic hyperfine coupling constant for nucleus K in frequency units (multiply by $\hbar$ if the HFC is in energy units), S is the electronic total spin, k_B is Boltzmann's constant, and T is temperature.

The isotropic chemical shielding constants should be computed with the appropriate solvent model, and the work below uses the SMD solvation model.[8] The B3LYP functional has previously demonstrated good NMR and EPR performance for metal-containing systems like those studied here,[6] although we do *not* consider electronic energies computed from this level of

theory as Swart has shown B3LYP to do poorly for the prediction of spin-state-energy splitting in iron coordination compounds.[9]

While the costly pseudocontact spin-orbit correction to the hyperfine tensor can be neglected, inclusion of the spin-orbit correction to the *g*-tensor is critical. Hyperfine coupling constants and the *g*-tensor are recommended to be computed using the DFT level of theory in gas phase within the spin orbit mean field approximation SOMF(1X).[10]

Zero Field Splitting. For systems with S > ½, the magnetic fields generated by more than one unpaired electron cause additional orbital splitting energies through the effect that each electron has on another. This effect is called the zero field splitting (ZFS) due to the appearance of additional electronic state from magnetic interactions in absence of magnetic field. ZFS is known to affect molecular properties, particularly through appearance of additional energetic states that cannot be predicted without spin-orbit coupling. However, this zero field splitting separations are typically quite small and described as the property D (in cm^{-1}).The extension for systems with S > ½ using the zero-field splitting interaction is neglected in the work in *2.2 Predicting Paramagnetic ^{1H} NMR Chemical Shifts and State-Energy Separations in Spin-Crossover Host-Guests Systems* on paramagnetic NMR; discussion of why we neglect this follows. The above formalism for paramagnetic NMR is derived for the S = ½ spin state, and extensions for systems having S > ½ involve incorporation of the zero field splitting (ZFS) phenomenon. Several methods have been derived to account for ZFS effects on paramagnetic shifts,[11-13] and we examined the ZFS effect from the extended formulation for the Kurland and McGarvey [11, 12]

$$\sigma_{con}^{iso} = \frac{2\pi}{\gamma}\frac{S(S+1)}{3kT}\mu_B\left[1 + \lambda_{KMcG}^{(1)} + \lambda_{KMcG}^{(2)}\right]g_{iso}A_{FC} \qquad (1.2.11)$$

where σ_{con}^{iso} is the ZFS corrected isotropic contact shielding, the first order ZFS correction term $\lambda_{KMcG}^{(1)}$ is given in from Hrobarik *et al.*[12] equation 39 , and the second order ZFS correction term $\lambda_{KMcG}^{(2)}$ is spin dependent and selected from Hrobarik *et al.*[12] equations 40(a-d) according to the S quantum number. The magnetic anisotropy was computed using the coupled-perturbed spin orbit correction method of Neese.[14] The ZFS correction to paramagnetic chemical shifts was

examined for a computed ZFS parameter D = -3.65 cm^{-1} for quintet Fe^{II} was found to change σ_{con}^{iso} by 0.02%. Since the Kurland and McGarvey approximation method is known to underestimate the D value,[15, 16] additional estimates for the upper limit of the ZFS correction were performed with larger D values. For the Fe^{II} quintet, a D = -45 cm^{-1} yields a change in σ_{con}^{iso} by -0.87%. Given the small magnitude of this correction and the expense of computing D, we determined that the ZFS correction can be neglected for the iron systems examined in this thesis.

1.3 Organization of the Thesis

As chemists characterize molecular systems in greater detail, it becomes clear that some observables can only be properly studied at the macromolecular scale. However, elucidating the physical and structural principles behind such phenomena as molecular recognition or chemical reactivity can be difficult when moving into the macromolecular regime. The objective of this work is to provide insights and predictions from theory to complement experimental undertakings. The work is divided into two categories: *Chapter 2: Chemical Recognition at the Macromolecular Scale* modeling molecular recognition through prediction of intermolecular interactions with highly accurate methods and *Chapter 3: Chemical Reactivity at the Macromolecular Scale* the modeling of chemical reactivity in macromolecular systems. First, the types of macromolecular systems that are examined in this thesis are described. Then, an overview of each section presented in this thesis is detailed.

Macromolecular Materials. Porous macromolecular systems, such as zeolites, have played an important role in industrial processes for decades.[17] Part of the success of zeolites has been the ability to select the proper material for its intended application. Zeolites can be generated within a large topological space, and the chemical interactions can be tuned through cation doping.[18-22] More recently, a new type of material, metal organic frameworks (MOFs), has been introduced, that allows for even greater variation and design in topological space and tuning of chemical interactions in contrast to zeolites. Metal organic frameworks are porous materials that are made up of metal nodes bound together by organic linkers (see Figure 1.3.1). These metal organic frameworks have demonstrated potential for applications in separations, catalysis, batteries, and gas storage. [17, 23-26] This thesis will highlight the predictive power of theory to aid synthetic efforts in the face of the enormous MOF configurational space. This thesis additionally includes a particularly promising application where catalytic activity of a MOF is utilized for the degradation of toxic chemical agents.

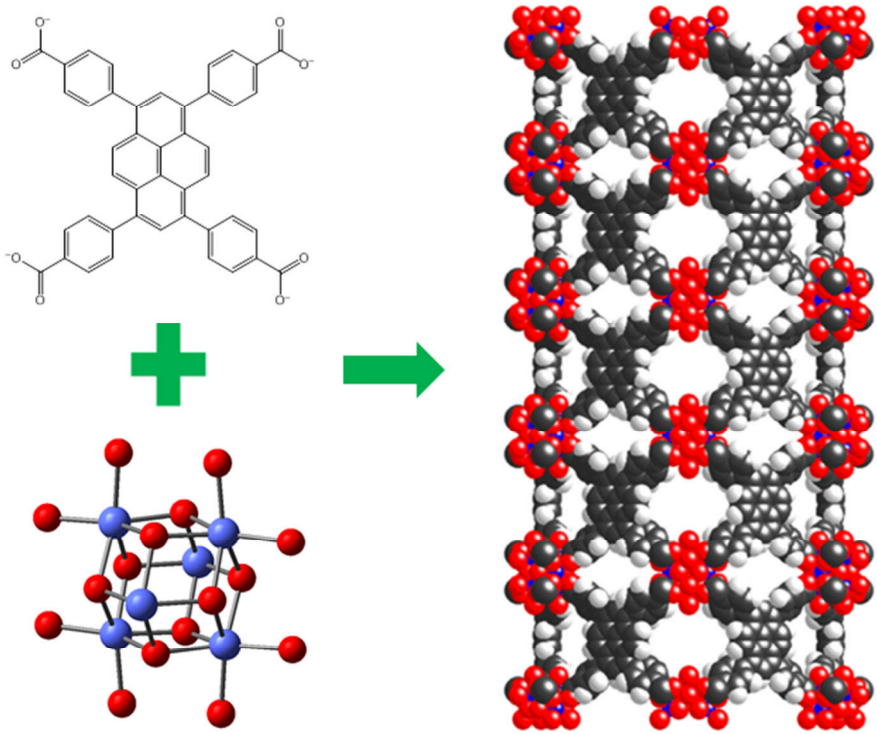

Figure 1.3.1: Schematic Representation of an organic ligand (top left) and a metal node (bottom left) being combined to generate a 3D topology (right).

Biomimetic and Biomolecular Macromolecules. In addition to the macromolecular materials systems presented above, a significant portion of my research has been in the area of biomimetic host-guest chemistry, and more recently protein spectroscopy. Host-guest chemistry emphasizes the design of a host molecule that will selectively bind a target guest. One host complex that I studied is a molecular cage, shown in Figure 1.3.2, first made in the group of Prof. Jonathan Nitschke.[27] The cage is a large tetrahedron where metal atoms, the blue spheres labeled M^{2+} at the corners, are connected by organic linkers. These cages feature an interior pocket for a guest molecule, which enters through the cages' porous faces.

These cages have demonstrated promising functionality as strong and discriminating binders of single organic guest molecules in solution.[27] As such, these cages offer promise for applications like targeted delivery. During targeted delivery, the encapsulated target is wrapped by the cage to protect the guest from damage until it reaches some intended target location.[28] The delivery of the guest can be induced through addition of a more strongly binding alternative

guest, or through the dissolution of the cage. The work in this thesis will examine the relationship between observable NMR signals and the ability to identify the encapsulated target or unique protein environment.

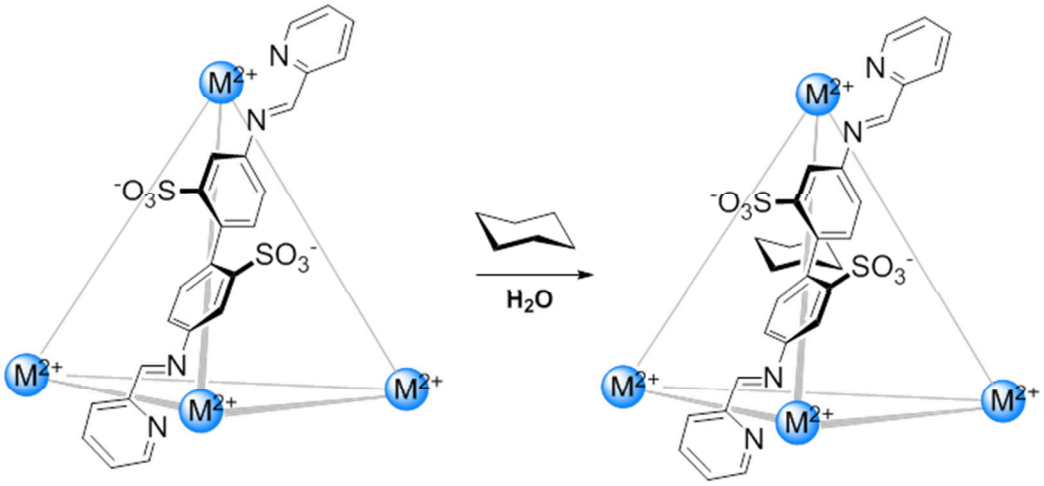

Figure 1.3.2: Sulfonated tetrahedral $[M_4L_6]^{4-}$ cage, self-assembles in water. Each edge of the tetrahedron connecting metal centers (M^{2+}) represents the ligand L shown. Each metal center has three ligands. Upon addition of an organic guest (shown above the arrow) in water, the guest becomes encapsulated inside the cage.

In addition to the biomimetic host-guest systems discussed above, this thesis will also examine biomolecular macromolecules known as proteins. Proteins are essential functional units in living organisms, yet the complexity of protein-protein interactions in biomolecular processes is staggering. Protein-protein interactions play a significant role in the Histone Code Hypothesis, where multi-protein complexes assemble to compose the machinery that transcribes DNA.[29] Without the transcription process, no RNA could be encoded to make the proteins that serve critical biological functions. Malfunction of the assembly of the multi-protein complex during transcription has been implicated in some disease processes.[30] The work in this thesis will examine the predictive power of theory for spectroscopic properties of fluorine in different protein environments, which can aid experimental studies of protein-protein interactions and the design of therapeutic targets from small molecular fragments.

2.1 Design of a Metal – Organic Framework with Enhanced Back Bonding for the Separation of N2 and CH4. This chapter presents a comprehensive quantum chemical analysis to a challenging, but industrially relevant gas phase separation. This important modern gas separation involves the removal of atmospheric nitrogen gas from natural gas. The sudden growth of fracking technology and its application to the extraction of natural gas from subterranean deposits has reduced energy costs and increased the availability of low-cost natural gas in the United States. Currently, nitrogen gas (N_2) introduced by fracking must be separated from natural gas based on physical properties via cryogenic separations. Such separations are very costly due to their low selectivity. An alternative approach is to design a material tailored to form a chemical bond with N_2, e.g., through introduction of a metal with an open bonding site. If methane, the main constituent of natural gas, cannot form an equivalent bond to the metal, the material should be able to selectively filter N_2 from natural gas, and dramatically reduce the purification cost.

Through a comprehensive theoretical investigation, a new material has been designed that is predicted to be capable of separating N_2 from methane.[31] This new material is a variant of a known metal-organic framework, in which vanadium (V) is substituted in the newly designed system for iron (Fe) in the known system. The V-based material is predicted to selectively bind N_2 by forming a significantly stronger interaction with N_2 than to methane. Whereas the Fe-based material does not form the chemisorption interaction with N_2, resulting in a similar strength metal-gas interaction for both methane and N_2.

My role in this project was to understand and exploit the physical bases for the formation of the stronger V–N_2 bond. To accomplish this, I surveyed many metal-N_2 interaction energies as a function of distance using highly accurate quantum chemical methods for a representative model system. I analyzed the resulting potential energy curves (see Figure 1.3.3) and elucidated the importance of a subtle feature of the electronic configuration of V that made this metal optimal for the separation. The chemisorption interaction is a result of increased back bonding from V to N_2, which can only occur for metals with three or fewer *d* electrons. This understanding should accelerate design efforts in alternative materials.

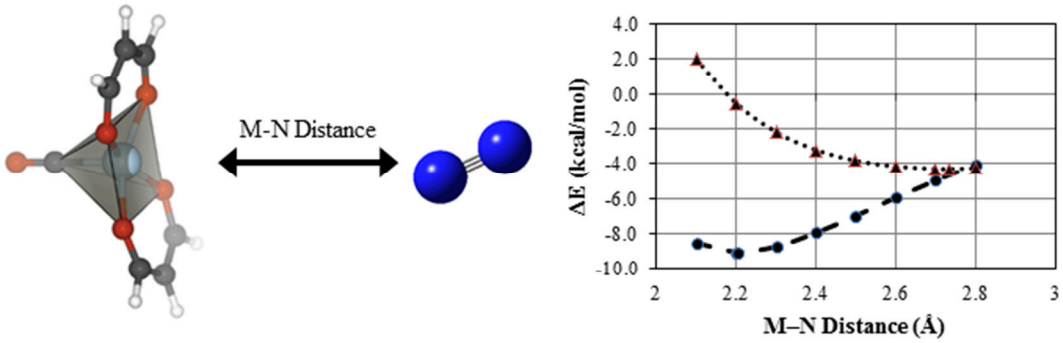

Figure 1.3.3: The potential energy curve as a function of M–N_2 distance. The curve for M = V(II) is shown as a dashed line with circular points. The curve for M = Fe(II) is shown as a dotted line with triangular points. Figure adapted from Lee *et al.*[31]

2.2 Predicting Paramagnetic ^{1H} NMR Chemical Shifts and State-Energy Separations in Spin-Crossover Host-Guests Systems. A particularly valuable tool for monitoring targeted delivery or guest encapsulation is an easily observed signal that indicates the status of a host-guest complex. For example, the detection of munitions in complex environments might be accomplished through targeted binding and signaling. In the above cage systems, experiments have determined that guest encapsulation induces observable changes in the electronic and magnetic properties of the iron centers. This process, called spin-crossover (SCO), involves a change in the electronic configuration of iron that is accompanied by an observable change in magnetic properties. The prevalence and magnitude of SCO was observed to depend on the identity of encapsulated guests, but the cages do not survive over a sufficient temperature range to permit full characterization of the SCO process. To supplement the experimental data, I have applied quantum chemical models to help characterize and understand this behavior.[32]

My research on this project began by successfully reproducing the well-defined magnetic properties of an analogous cobalt cage. I used this validated model to compute magnetic properties for the iron cage in order to determine the energy required to affect SCO (ΔH_{SCO}). The ΔH_{SCO} inferred from experiment also presented a puzzle; it was much lower ($\approx$ 8 kcal mol^{-1}) than was predicted by our computational model ($\approx$ 30 kcal mol^{-1}). Knowing that the

SCO product would be dependent on *dynamically* varying metal-ligand bond distances, I surveyed the X and Y bond coordinates for the cage corners as shown in Figure 1.3.4. A region where experiment and theory are found to be consistent is indicated by the red star, which is far from the lowest energy structure expected for a *static*, empty cage. This result indicates that dynamic configurations will play a crucial role in SCO, which is further reinforced by the unique effect on the local metal coordination induced from each guest upon binding.

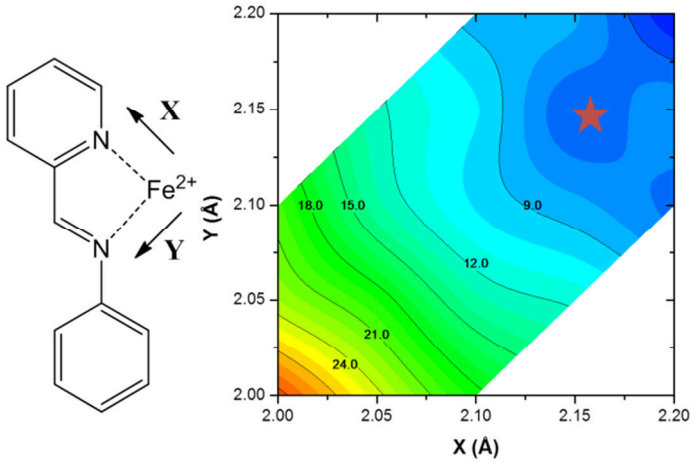

Figure 1.3.4: The predicted enthalpy (kcal/mol) of spin-crossover at a cage corner (one metal center from the cage in Figure 1.3.2). Increasing metal–ligand distances are shown on X and Y, schematically shown for one ligand. Figure adapted from Isley III *et al.*[32]

2.3 The Prediction of ^{19F} NMR in Proteins. The monitoring of subtle changes in a protein's environment is a challenging and complex problem given the size and non-uniformity of biomolecular systems which leads to complex data interpretation. However, the observation of ligand complexation in biomolecular systems is extremely important in the design of new medicinal therapeutic drugs. Great advances have been made in understanding chemical recognition and reactivity in biomolecular systems with small ligands. Yet, the design of small molecule drugs that target protein-protein interfaces poses a particularly challenging problem. These sites have historically been considered undruggable in an important class of protein domains called bromodomains. Bromodomains are key players in the assembly of DNA transcriptional machinery, and malfunctioning bromodomains have been implicated in various

diseases. The primary challenge for developing medicinal targets for bromodomains is that high throughput detection of fragment binders is extremely difficult.

A recent advance in detection capabilitiy has been to label residues near the inhibitor's binding site with fluorine atoms, which are magnetically active, and can be used in fragment screening studies to discover new inhibitor designs for medicinal purposes. This method provides a significant advancement in the ability of experiments to selectively test for new drug fragment binding effects. The hurdle for this method lays in the assignment of the protein's fluorine NMR spectra. Through collaboration with the Pomerantz group at the University of Minnesota, my work in this area has focused on the development of a method to predict ^{19}F NMR spectra. Current results have demonstrated that the prediction of ^{19}F NMR in proteins is a challenging problem due the model's sensitivity to hydration environment, but an automated procedure for spectral assignment is within reach.

3.1 Electrochemical Reduction of 2,4-Dinitrotoluene in Aprotic and pH-Buffered Media. Selective detection of undesirable impurities is an attractive capability to have for any chemical process. A key impurity in the industrially synthesized explosive 2,4,6-trinitrotoluene (TNT) is 2,4-dinitrotoluene (DNT). DNT has a higher volatility and is easier to detect through electrochemical reduction than TNT. Electrochemical sensors rely on detection of DNT, a prevalent contaminant in TNT, making selectivity fundamentally important in sensors of explosive devices. A mechanistic understanding of the electrochemical reduction of DNT has previously been lacking. Characterization of the pathway for DNT's electrochemical reduction has confirmed the appearance of a bishydroxylamine species, its signature spectra, and should be helpful in developing improved sensor devices. Through application of density functional methods, the full electrochemical reduction pathway has been characterized for DNT, and supports experimental findings reported.

Through collaboration with the Buhlmann group at the University of Minnesota, my work in this area has focused on the characterization of the mechanism for the electrochemical decomposition of DNT.[33] Given that the reduction of DNT goes through an 8 electron/8

proton process there are a staggering number of intermediates possible. We have determined that instead of full reduction of one nitro group into amines (leaving one nitro group untouched, see Figure 1.3.5), the system dramatically favors the generation of a bishydroxylamine species. Knowledge of this pathway for reduction can be applied to improve sensors of DNT to selective recognition of spectral features after an 8 electron reduction.

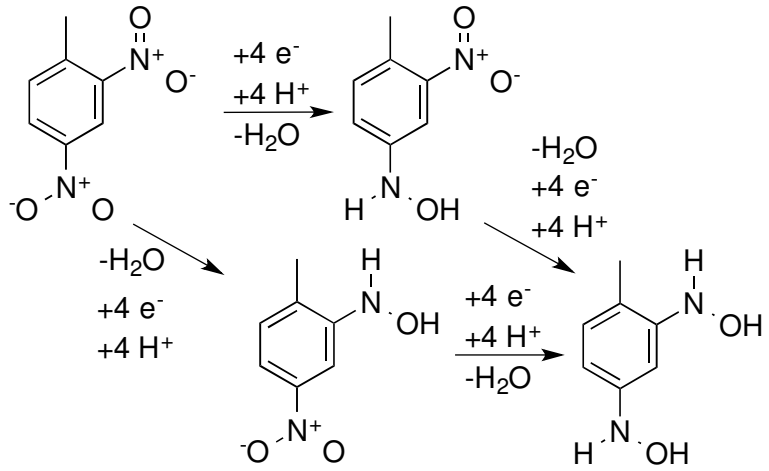

Figure 1.3.5 Pathway for the Electrochemical Reduction of 2,4-Dinitrotoluene. Reduction of DNT proceeds through a hydroxylamine intermediate after 4 electron and proton equivalents, then to a dihydroxylamine final species.

3.2 Decomposing Chemical Warfare Agents Utilizing Metal–Organic Frameworks This chapter presents a new material found to rapidly catalyze the decomposition of extremely toxic chemical warfare agents. Rapid decomposition of chemical warfare agents would be beneficial in numerous applications, such as personnel protection or stockpile disarmament. The macromolecular metal organic framework NU-1000 was demonstrated to be extremely effective in catalyzing the hydrolysis of phosphoester based chemical warfare agents. Predictive computations were performed on a nerve agent simulant DMNP, and toxic nerve agents GD (Soman) and VX, uncovering the key role that the metal nodes of NU-1000 play in activation of the phosphoester bonds for hydrolytic attack. Experimental confirmation of the catalytic activity of NU-1000 was demonstrated in this work, as well in subsequent work.

Chemical warfare agents (*e.g.,* GD and VX) containing phosphate ester bonds are among the most toxic chemicals known to mankind. For some applications, rapid destruction of agents is essential.[34, 35] Not only is the reactivity critical for these materials, but so is selectivity in the production of non-toxic products. Figure 1.3.6a shows the two possible products of VX hydrolysis, one of which is non-toxic, whereas the other is still an active agent. The toxic product of VX hydrolysis is harder to hydrolyze to a nontoxic molecule, which can dramatically increase the half-life the decomposition in non-selective materials.

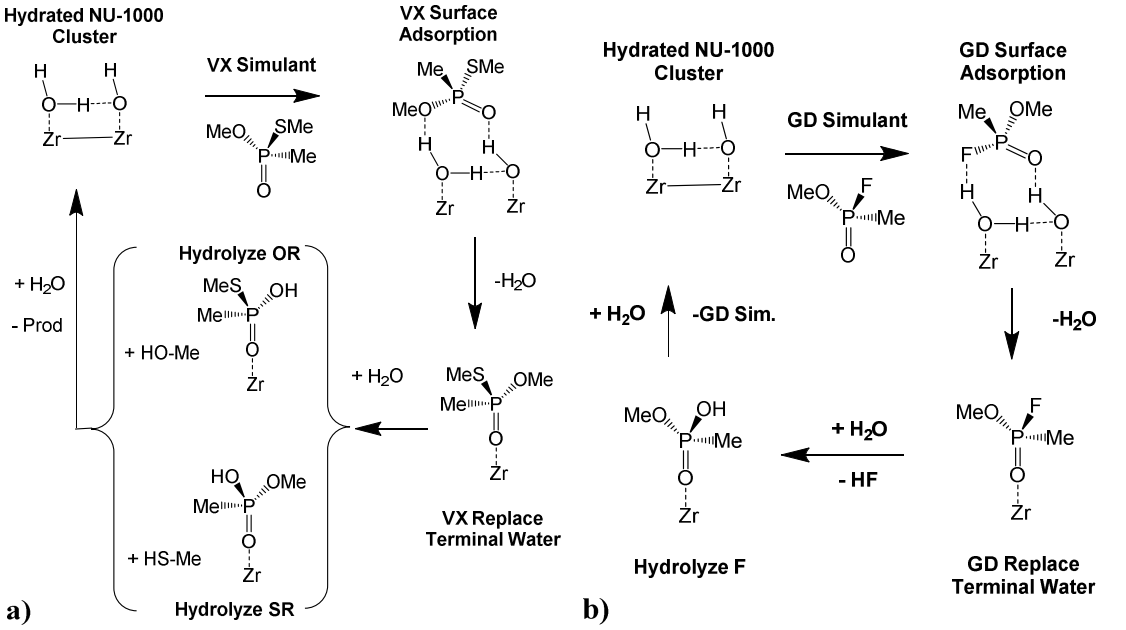

Figure 1.3.6: Schematic Catalytic cycle showing a hydrated MOF cluster, to surface adsorption of the a) VX analog or b) GD analog, to the agent replacing a surface bound H_2O molecule, to deactivation of the agent, and finally to regeneration of the MOF. Hydrolysis of the VX thioester (SR) results in a non-toxic product, whereas hydrolysis of the ester (OR) yields a toxic product.

My work on this project involved theoretical predictions for carefully chosen metal-organic framework (MOF) material featuring high porosity and exceptional chemical stability that is extraordinarily effective for the degradation of nerve agents and their simulants. [36] Through collaboration with the Hupp and Farha groups at Northwestern University, a new material was designed and studied for the catalytic decomposition of phosphate ester chemical warfare agents. While the material had been previously demonstrated to hydrolyze nerve agent

simulants,[37] experiments with nerve agents are extremely dangerous. Our methods predicted that GD and VX would show the same reactivity as the nerve agent simulants giving further justification for undertaking the dangerous experiments. Computational models pointed to Lewis acidic Zr^{IV} ions as the active site and to their accessibility as a defining element of their efficacy, which have a very similar structure and predicted energetics to the biologically active phosphotriesterase enzyme which affect the same reaction.[38] The proposed catalytic cycle for the GD nerve agent simulant is shown in Figure 1.3.6b. In addition to showing the utility of the Zr^{IV} Lewis acid active sites, computations also predicted that this material would be much more selective for detoxification of VX than previous industrial scale methods. Further explorations into the catalytic ability of the Zr node within other MOFs to degrade phosphate ester based agents was demonstrated,[39, 40] and experimental evidence supporting the prediction of selective VX hydrolysis[36] to produce the non-toxic product has been found.[41]

Chapter 2

Chemical Recognition at the Macromolecular Scale

2.1 Design of a Metal – Organic Framework with Enhanced Back Bonding for the Separation of N_2 and CH_4[†]

2.1.1 Introduction

The coordination of dinitrogen to transition metal cations is important both fundamentally and industrially. Dinitrogen is highly inert and generally considered to be a poor ligand. In 1965, however, it was shown that a simple coordination complex, $[Ru(NH_3)_5]^{2+}$, could reversibly bind N_2.[42] In subsequent years, a number of dinitrogen–transition metal complexes have been isolated for metals in varying oxidation states with various coordination numbers.[43, 44] These complexes typically feature low-valent, relatively reducing metal cations coordinated to dinitrogen in an end-on binding mode. Activating dinitrogen at a metal center to promote its reduction by hydrogen to ammonia under moderate conditions remains a critical goal for homogeneous catalysis. Somewhat weaker metal-dinitrogen binding, however, may be useful for the adsorptive separation of gas mixtures. An example is provided by the need to remove dinitrogen (an omnipresent but noncombustible contaminant) from natural gas or other methane-rich gases. This is an extraordinarily difficult separation based on physical properties alone, as both gases lack a permanent dipole and have similar polarizabilities, boiling points, and kinetic diameters. Although cryogenic distillation is currently utilized for the separation of these gases, the cost- and capital-intensive nature of this separation has led to the development of a number of competing processes, such as membrane- or kinetics-based separations, which generally suffer from low selectivities.[45]

Adsorptive separations utilizing porous solids containing transition-metal cations capable of reversibly binding dinitrogen may result in highly selective and efficient

---

[†] Adapted with permission from:

Lee, Kyuho; Isley III, William C.; Dzubak, Allison; Verma, Pragya; Stoneburner, Samuel J.; Lin, Li-Chiang; Howe, Joshua D.; Block, Eric D.; Reed, Douglas A.; Hudson, Matthew R.; Brown, Craig M.; Long, Jeffery R.; Neaton, Jeffery B.; Smit, Berend; Cramer, Christopher J.; Truhlar, Donald G.; Gagliardi, Laura *J. Am. Chem. Soc.* **2014**, 136 (2), pp 698-704.

Link: http://dx.doi.org/10.1021/ja4102979

dinitrogen/methane separations. Metal–organic frameworks are particularly promising in this regard, as they offer a myriad of materials design opportunities and have already shown great potential for a number of gas separation applications.[23, 24] These materials typically display high internal surface areas that can be decorated with both ligand- and metal-based functionalities.[46] In principle, this permits the rational design of local environments tuned for the selective binding of specific gases. The M-MOF-74 series of compounds having formula M_2(dobdc) (where $dobdc^{4-}$ is 2,5-dioxido-1,4-benzenedicarboxylate) is an especially versatile and intensively studied structure type.[47-52] This structure features 12 Å-wide hexagonal channels, lined at the vertices with helical chains of five-coordinate divalent metal ions connected through $dobdc^{4-}$ bridging ligands. Upon activation, these materials have an extremely high density of open metal coordination sites, leading to the possibility of a high working capacity for storage or separation applications.

M-MOF-74 structures containing Mg^{2+}, Mn^{2+}, Fe^{2+}, Co^{2+}, Ni^{2+}, Cu^{2+}, and Zn^{2+} have been synthesized. CH_4 and N_2 adsorption enthalpies reported for a number of these materials indicate they are likely not useful methane/nitrogen separation materials. For example, Mg-MOF-74 displays CH_4 and N_2 adsorption enthalpies of 4.4[53] and 5.0[54] kcal/mol, respectively. However, in principle other dicationic metals could be incorporated into this structure type. As the synthesis of pure M-MOF-74 phases is often quite challenging, it would be advantageous to know *a priori* which variations are the best candidates for a given gas separation application. This is a predictive challenge appropriate for the application of computational quantum chemistry, which can be used to pinpoint which cations might be anticipated to have interactions of significantly different strengths with competing guests. The interactions between M-MOF-74, corresponding to different M, and various adsorbates were investigated theoretically, which suggested that V-MOF-74 could be promising in the N_2/CH_4 separation. We thus decided to study V-MOF-74 in detail. Here, we show, based on three models (Figure 2.1.1 a, b, and c) of the MOF, that selective back bonding interactions[55, 56] from the vanadium(II) cation centers in V-MOF-74 to the unoccupied π^* orbitals of N_2 can be used to separate N_2/CH_4 mixtures. We further use calculations by Kohn–Sham density functional theory[57] (DFT) and correlated wave-function

theory to put this prediction on a quantitative basis and compare it with the experimentally characterized Fe-MOF-74.

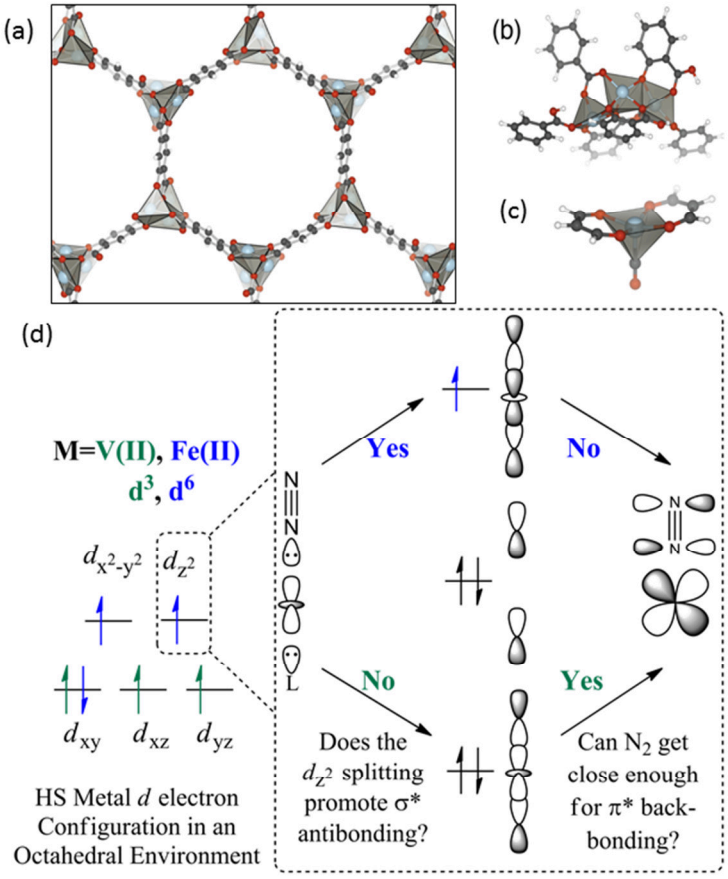

Figure 2.1.1. (a, b, and c) Structural models used in this work. (a) Optimized periodic framework model, based on the symmetry of the experimental primitive cell. (b) 88-atom cluster. (c) Small model. Light blue, red, dark gray, and white spheres represent vanadium, oxygen, carbon and hydrogen atoms, respectively. (d) Three-center bonding diagram between framework O atoms, the metal, and a guest. On the left we show the *d* subshell occupancy of Fe(II) in both blue and green; V(II) would have only three electrons (green alone) in the *d* subshell, and the metal d_z^2 orbital would be empty. On the right, the middle section shows how the d_z^2 orbital splits upon interacting with the four lone pair electrons of two axial Lewis bases; the occupancies shown are for Fe(II) – only four electrons would be present for V(II) because the d_z^2 orbital of V(II) is unoccupied. The right-most orbital diagram shows the nature of the interaction of the ligand unoccupied π* orbitals with the occupied *d*π orbitals of the metal; when the anti-bonding orbital is occupied, the ligand cannot approach the metal as closely, and this interaction is substantially weaker.

2.1.2 *Theoretical Methods*

In order to treat the adsorption process reliably, we need to use electronic structure methods that include dynamical correlation, especially attractive medium-range noncovalent forces. Most exchange-correlation (xc) functionals currently used in DFT do not treat such medium-range correlation energy accurately; however, here we use two kinds of density functionals that overcome this limitation. (1) The Rutgers-Chalmers van der Waals density functionals[58] use a nonlocal formulation of the correlation part of the xc functional and can treat attractive van der Waals interactions both at medium range and long range. We use the vdW-DF2+U functional[59] of this type with Hubbard U corrections,[60] where U is a parameter for metal d electrons that is determined to reproduce oxidation energies. (2) The Minnesota functionals[61] include the local kinetic energy density in the xc functional and have been shown to yield accurate noncovalent attraction at van der Waals distances;[62] we will employ three such functionals, M06-L,[63] M06,[64] and M11-L,[65] because they are based on very different approaches: M06-L is a well validated[61, 62, 64] local functional with global parameters, M11-L is a recent local functional employing different exchange and correlation parameters for short and long interelectronic distances, and M06 employs 27% Hartree–Fock exchange, as justified by adiabatic connection arguments[66] to reduce DFT self-interaction error.

We also employ two wave function theory (WFT) methods, in particular local-pair natural-orbital coupled cluster theory with single and double excitations[67] (LPNO-CCSD) and complete active space second-order perturbation theory with counterpoise corrections (CASPT2-CP).[68] The latter method has been shown to yield accurate energetics in systems containing transition metal compounds.[69, 70]

The DFT and WFT methods used here involve approximations that impose limits on their accuracy. Because they represent very different approaches to the electronic structure problem, confidence in the utility of their quantitative predictions is significantly increased when different models agree, even if the natures of the various approximations employed make it unclear which model is most accurate within the remaining variation.

Orbitals, spin states, cores, relativistic effects, and metal ions. In Kohn-Sham calculations and in the reference state for LPNO-CCSD, the V and Fe ions are in high-spin states (quartet and quintet, respectively), and all other orbitals are doubly occupied. For the CASPT2-CP calculation on the 88-atom cluster, we replace the two outer metal ions by closed-shell Zn(II) ions and treat the central metal in the active space. (None of the DFT calculations involve this Zn substitution.) Descriptions of the active spaces used for all species are given in the SI. The vdW-DF2 calculations with the Hubbard U correction employ the all-electron projector-augmented wave (PAW) method for scalar relativistic core electrons and ionic potentials; all other calculations treat all electrons explicitly. The CASPT2-CP calculations use the Douglas-Kroll-Hess relativistic approximation, and the extended transition state (ETS) method for energy decomposition analysis combined with the natural orbitals for chemical valence (NOCV) theory calculations use the ZORA relativistic approximation. All other calculations are nonrelativistic.

Basis sets. All the vdW-DF2+U calculations employed a plane-wave basis with a 1000 eV kinetic energy cutoff. All other DFT calculations employed the def2-TZVP basis except the ETS-NOCV analysis, which used TZ2P. LPNO-CCSD calculations are extrapolated to a complete basis set from def2-TZVP and def2-QZVP. CASPT2-CP calculations for the small model employed the ANO-RCC-TZVP basis for all atoms, and for the 88-atom cluster they employed the ANO-RCC-DZVP basis for all atoms.

Coordinates. We used a triclinic primitive unit cell containing 54 atoms including 6 metal centers, and simultaneously optimized the lattice vectors and the atomic positions in the unit cell with variable cell dynamics with PBE+U for bare MOFs and with vdW-DF2+U for adsorbates. The 88-atom clusters were taken out of these periodic structures. Optimization of binding geometry of adsorbates in the periodic MOFs and on the 88-atom cluster involved freezing the MOF and optimizing only the coordinates of the adsorbate; this was carried out with all DFT calculations. The structure of the small model was fully optimized by M06-L and these structures were used for the LPNO-CCSD and CASPT2-CP calculations. Full coordinates and absolute energies in hartrees of selected structures are in SI.

The starting geometries for the periodic model were based on the experimental structures[47-49, 51, 71] of M-MOF-74 (Figure 2.1.1a) and further optimized by DFT; the experimental unit cell contains 54 atoms, including 6 metal centers. We defined two other models of M-MOF-74 to be studied at additional levels of theory. The cluster (Figure 2.1.1b) has 88 atoms, including three metal centers, and it was designed[52] to retain the local structure of MOF-74 about the central metal ion while remaining small enough for high-level electronic structure calculations. The small model (Figure 2.1.1c) has 19 atoms, including one metal center and is small enough to conduct calculations by expensive wave function methods for comparison.

All iron and vanadium ions were modeled in their respective ground (high-spin) state. To maintain charge neutrality with all oxide ligands in the small model, we included a *trans* carbonyl ligand. Although carbonyl groups are usually considered to be strong-field ligands, the small model nevertheless maintains a high-spin ground state and an electronic structure consistent with the larger model. Indeed, the insensitivity of our conclusions to the nature of the *trans* ligand in the M-MOF-74 model provides particularly strong support for our analysis.

Charges. Partial atomic charges were calculated by charge model 5(CM5).[72, 73]

Software. Minnesota functionals: Gaussian 09;[74, 75] vdW-DF2+U: VASP;[76] LPNO-CCSD: ORCA 2.9.[77] CASPT2-CP: Molcas 7.8;[78] ETS-NOCV: ADF.[79-81]

2.1.3 Results and Discussion

N_2 bonding motif to V-MOF-74 and Fe-MOF-74. A molecular orbital picture can be used to predict selective adsorption of N_2 over CH_4 with V-MOF-74. The model exploits the square-pyramidal coordination geometry of the metal in desolvated M-MOF-74 (Figure 2.1.1d). A key consideration is the d^3 electronic configuration of V(II). In the case of N_2 binding, our DFT calculations show that a three-center bond is formed between the framework oxo ligand *trans* to dinitrogen, the metal, and N_2 (Figure 2.1.1d). Given an end-on coordination geometry, a pair of nonbonding electrons on N_2 and its respective *trans* framework atom interact with the V(II) d_z^2 orbital, and the net result is a three-center bond with two electrons each in a bonding and

nonbonding orbital. In addition to the resulting σ bond, the unoccupied π* orbitals of N_2 can accept back bonding electrons from the metal *d*π orbitals. This back bonding is *not* present for methane, due to the lack of low-energy π* orbitals on the hydrocarbon. Fe(II), in contrast, has a high-spin d^6 electronic configuration with a singly occupied d_z^2 orbital. In this case, the two doubly occupied lone pairs provide four electrons to the three-center bond and the occupation of the metal d_z^2 orbital provides one electron, for a total of five electrons in the three-center bond; so, one electron is in the antibonding orbital. As the N_2 approaches the metal site, it thus experiences unfavorable σ anti-bonding plus additional exchange-repulsion from the occupied nonbonding orbital. Consequently, N_2 cannot approach the Fe(II) center closely enough to experience π* back-bonding stabilization as favorable as is present in the V(II)–N_2 system.

In subsequent sections of this article, we confirm the differential stabilization effect with local and nonlocal DFT calculations, confirming our molecular orbital prediction that as-yet unsynthesized V-MOF-74 could be used to separate N_2 from CH_4. We also reinforce our DFT results with correlated wave function calculations to rule out the possibility of artificial back-bonding[82] owing to the possible underestimation of the energy gap and the delocalization of *d* electrons in the DFT models. Finally, we analyze single-determinantal Kohn-Sham reference functions to confirm the above explanation of the effect.

N_2 and CH_4 adsorption in V-MOF-74 and Fe-MOF-74. The key quantity we calculated is the differential adsorption energy defined by

$$\Delta E_{ads} = E_{ads}(N_2) - E_{ads}(CH_4) \qquad (2.1.1)$$

where E_{ads} is the energy of adsorption (here defined as a positive number to denote that deadsorption is endoergic); thus ΔE_{ads} is more positive when N_2 binds more strongly. The results are in Table 2.1.1. Across all levels of theory and all models, CH_4 binding is comparable between the two metals, but N_2 is predicted to bind significantly more strongly than CH_4 to the coordinatively unsaturated metal site when the metal is V rather than Fe.

We noted above the consistent trend observed for calculated ΔE_{ads} values; the trends in calculated E_{ads} values are also consistent across the methods. Absolute adsorption energies for

the 88-atom cluster and the periodic model are compared in Table 2.1.2. We see remarkable agreement between the adsorption energies calculated with the 88-atom cluster and with the periodic model and further remarkable agreement between the absolute binding energies calculated by DFT with different functionals and by WFT; the good agreement of results obtained with several methods that incorporate the physics in different ways adds confidence to the predictions. Inspection of Table 2.1.2 shows relatively large differences in the absolute binding energies between the large and small clusters. The enhanced attraction in the 88-atom cluster model can partially be attributed to greater medium-range correlation effects. One should also consider that the two models have different ligand coordination environments, and this too has an influence on the absolute binding energies.

Table 2.1.1: N_2/CH_4 adsorption energy differences, ΔE_{ads}, in kcal/mol

	Small Model		Large Models[a]	
Level of Theory	V	Fe	V	Fe
DFT, vdW-DF2+U			6.0	0.4
DFT, vdW-DF2+U	4.9	0.4	5.8	0.3
DFT, M06-L	4.3	0.0	10.1	0.9
DFT, M06	4.5	0.1	6.9	0.4
DFT, M11-L	4.2	-0.8	5.9	-1.7
DFT, LPNO-CCSD/CBS	4.8	0.7	*b*	*b*
WFT, CASPT2 CP	3.8	0.3	2.1	0.3

[a]The first row is for the periodic model and the other large-model calculations are for the 88-atom cluster. [b]Impractically computationally intensive.

In order to further verify the validity of these predictions, isosteric heats of CH_4 and N_2 adsorption in Fe_2(dobdc) were obtained experimentally from adsorption isotherms at 175 K. (Details of the experiment are in SI.) As seen in Figure 2.1.2, the uptake of N_2 in Fe-MOF-74 is relatively steep and approaches one N_2 molecule per iron cation site at 1 bar and 175 K. Methane uptake, while similar at low pressure, reaches a higher value of approximately 1.5 CH_4 molecules per iron at 1 bar. These plots yield isosteric heats of adsorption for methane and

dinitrogen that are both relatively low and quite similar; in particular they are 5.3±0.2 and 5.5±0.2 kcal/mol, respectively, which yields an experimental difference of 0.2±0.3 kcal/mol. These results differ from the previously reported values of 4.8 kcal/mol for CH_4[83] and 8.4 kcal/mol for N_2[51] both because of the lower temperature and because of the change in experimental procedure; the present results should be more accurate for the difference because they were done with isotherms at the same temperature on the exact same batch of sample. An attempt to obtain the same information for V-MOF-74 was not successful.

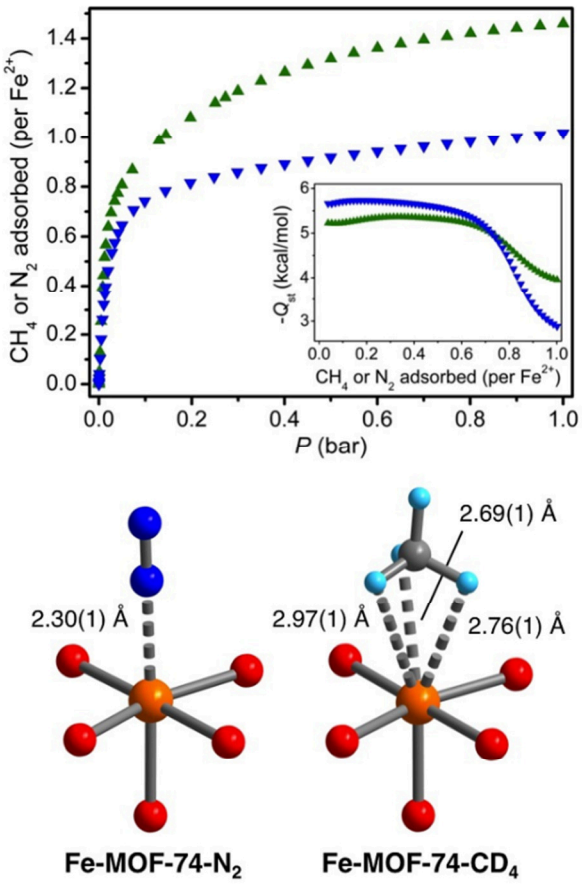

Figure 2.1.2:(Upper) Adsorption of methane (green) and dinitrogen (blue) in Fe_2(dobdc) at 175 K. (Upper Inset) Isosteric heats of adsorption. (Lower) The first coordination spheres for the iron centers in the solid-state structures obtained upon dosing Fe-MOF-74 with dinitrogen or methane; orange, red, blue, gray, and light blue represent iron, oxygen, nitrogen, carbon, and deuterium, respectively.

Experimental *enthalpies* of adsorption should not be compared directly to the *energies* of adsorption in Table 2.1.2. For the 88-atom cluster, however, we computed the enthalpies of adsorption at 175 K by a formula given previously.[52] The M06-L, M06, and M11-L levels of theory give predicted differences in adsorption enthalpy of 1.1, 0.5, and -1.6 kcal/mol, respectively. The average difference in predicted adsorption enthalpy of 0.0 kcal/mol is in good agreement with the 0.2 kcal/mol difference observed experimentally.

Table 2.1.2: Absolute binding energies (kcal/mol)

	V-N_2	Fe-N_2	V-CH_4	Fe-CH_4
Periodic Model				
vdW-DF2+U	13.4	6.6	7.4	6.3
88-atom Cluster				
vdW-DF2+U	12.0	4.5	6.2	4.2
M06-L	19.9	7.8	9.8	6.9
M06	17.5	8.1	10.6	7.7
M11-L	13.4	4.4	7.5	6.1
CASPT2 CP	7.4	3.3	5.3	3.0
Small Model				
vdW-DF2+U	8.5	3.2	3.6	2.9
M06-L	9.1	4.3	4.8	4.3
LPNO-CCSD/CBS	9.6	4.2	4.8	3.6
CASPT2 CP	6.5	3.3	2.7	3.0

Structural parameters, vibrational frequencies, and charges. Table 2.1.3 shows that the M–N distance is shorter in V-MOF-74 than in Fe-MOF-74, as anticipated above; there is also a smaller difference in the M–C distances for CH_4. Neutron powder diffraction experiments on Fe-MOF-74 at 10 K (see figure in SI) indicate excellent agreement between the calculated and experimentally observed structures of methane bound to Fe^{2+}. Specifically, the Fe–C distance of 2.98(1) Å is very close to the distance of 2.96 Å calculated for the 88-atom cluster. Differences in M–N distances are consistent with the energetic results presented above.

The potential energy curves (given in Figure 2.1.3) provide further evidence for qualitatively different kinds of interaction; we give just one example, the interaction of N_2 with M in the small model, calculated by M06-L. Single-point energies were calculated by modifying the M–N_2 distance, but keeping all other geometrical parameters unchanged from the geometric minima. Interestingly, the predicted interaction energy at 2.8 Å is nearly equivalent for N_2 with the Fe and V small models. At an M–N distance of 2.8 Å, the interaction energy is ~–4 kcal/mol for both V and Fe. As N_2 approaches more closely, the potential energy reaches a minimum of –4.3 kcal/mol at 2.73 Å for Fe, but it goes to a much deeper well at –9.1 kcal/mol at 2.21 Å for V. (This further reinforces the conclusion that the binding interaction to vanadium is quite different from that of other metals studied.) For comparison, the Fe–N distance was determined to be 2.30 Å for N_2 adsorbed within Fe-MOF-74 by neutron diffraction experiments at 9 K.[48] The predicted Fe-N distance for the 88-atom cluster compares favorably with the measured value of 2.30 Å.

The N–N stretching frequency is a probe of back bonding, because these shifts result from weakening the bond by $d\pi \rightarrow \pi^*$ back donation. The periodic vdW-DF2+U calculations show that, as compared to the isolated gas-phase diatomic vibrational frequency (2415 cm^{-1}), N_2 bound to V experiences a significant shift in the N–N stretch (–102 cm^{-1}), whereas N_2 bound to Fe shows a negligible change (–6 cm^{-1}). In contrast, the vibrational frequency shifts for C–H modes in CH_4, where no back bonding is predicted, are negligible. For the 88-atom cluster, M06 calculations for N_2 bound to MOF show similar trends—a 103 cm^{-1} shift for V and a 4 cm^{-1} shift for Fe; M11-L also shows similar shifts: 101 and 5, respectively. Table 2.1.3 shows a more complete set of results for M06-L; and these too are consistent with our analysis.

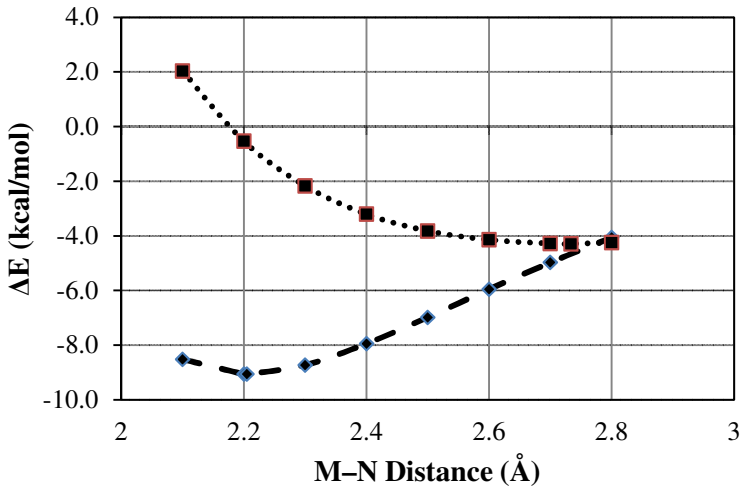

Figure 2.1.3: The potential energy curve as a function of M–N_2 distance for the small model as calculated with the M06-L exchange–correlation functional. The curve for M = V(II) is shown as a dashed line with diamond points indicating single-point energies. The curve for M = Fe(II) is shown as a dotted line with square points indicating single-point energies.

Next we examine in more detail the amount of charge transfer between the metal and the N_2 guest. Key charges in atomic units are given in Table 2.1.3.

The total charge on the guest molecule is computed by summing the partial charges of the individual atoms of the guest molecule; this indicates the magnitude and direction of charge transfer between the MOF and the guest. For each of the three functionals, CM5 partial atomic charges for the 88-atom cluster indicate donation of negative charge from the central metal ion to the nitrogen molecule and an opposite direction of transfer for methane. This is also reflected in the charge on the metal ion being increased for N_2 adsorption and decreased for CH_4 adsorption when compared to the bare MOF. The increase or decrease in the positive charge of the central metal ion with N_2/CH_4 adsorption does not exactly equal the total charge on the guest molecule. This reflects charge change within the rest of the MOF framework.

Table 2.1.3: M06-L bond distances, adsorbate frequencies, and partial atomic charges

	Gas	Small model		88-atom cluster	
	phase	V	Fe	V	Fe
		Structural descriptors: binding N_2			
M-N (Å)	-	2.21	2.73	2.08	2.34
ν_{N-N} (cm^{-1})	2424	2357	2430	2252	2360
		Structural descriptors: binding CH_4			
M-C (Å)	-	3.00	3.15	2.77	2.96
ν_{C-H} (cm^{-1})	3057	3037	3043	3017	3031
		Partial atomic charges: bare MOF			
M	-	0.90	0.69	0.81	0.69
		Partial atomic charges: binding N_2			
M	-	0.89	0.66	0.88	0.70
N_2	0.00	0.01	0.07	-0.09	0.09
		Partial atomic charges: binding CH_4			
M	-	0.85	0.66	0.74	0.66
CH_4	0.00	0.06	0.03	0.05	0.08

We find that the direction of electron transfer from the metal center to the guest molecule for the Fe–N_2 system is *opposite* to what is observed for V–N_2. Specifically, the partial atomic charge on Fe is 0.66 in the presence of either N_2 or CH_4; these values are the same as the values of 0.66 for the bare Fe-MOF-74 framework. The partial atomic charge on the V ions in V-MOF-74 is significantly higher in all structures, and it is not very sensitive to the adsorbates in the small model, but in 88-atom cluster the partial atomic charge on the V increases by 0.07 upon adsorption of N_2 and decreases by 0.07 upon adsorption of CH_4. Overall these changes are consistent with our interpretation of increased back bonding in the V–N_2 case.

Orbital analysis. The nature of the M–N_2 bond of the small model was investigated using the extended transition state (ETS) method for energy decomposition analysis combined with the natural orbitals for chemical valence (NOCV) theory. ETS-NOCV analysis[84] separates bond formation energy into distortion of interacting subsystems, steric interaction (with electrostatic

and exchange-correlation contributions), and an "orbital" term that represents a combination of the interactions between the occupied molecular orbitals on one bonding partner with the unoccupied molecular orbitals of the other and the intrafragment polarization. ETS-NOCV calculations carried out on the small model with M06-L show (see Figure 2.1.4) that both σ donation and π* back bonding interactions are weaker for Fe–N_2 than for V–N_2. Comparing the two largest alpha and beta spin paired NOCV contributions to the bond energy, the σ interactions are about eight times stronger for V than for Fe, and the π* back bonding type interactions are about twice as strong, with all other contributions being less than 1 kcal/mol for V and less than 0.5 kcal/mol for Fe. Such analyses of charge rearrangement are not unique, so we also performed natural bond order (NBO) analysis[85], as described next, to test the robustness of this interpretation.

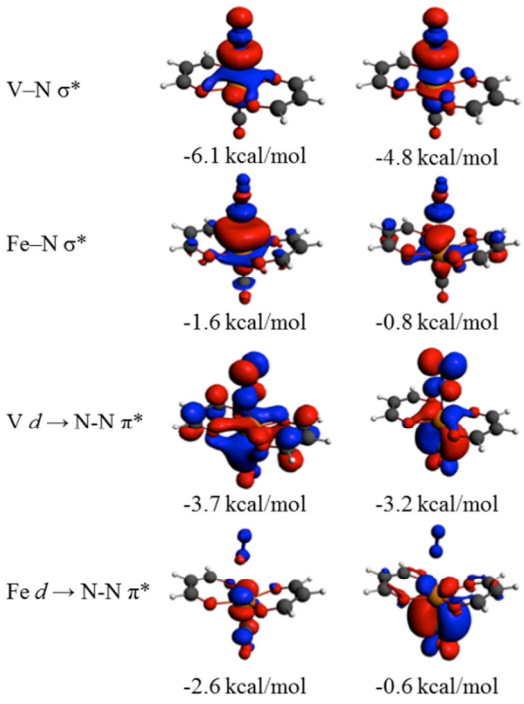

Figure 2.1.4: Contours of NOCVs for N_2 binding with V-MOF-74 and Fe-MOF-74. The four NOCV orbitals with the largest contributions to the binding energy are reported for each case, with the sum of the α and β spin contributions to the bond energy shown immediately below. Only the α orbitals are shown as the β orbitals have the same character.

NBO analysis on the small model identifies a σ bond for V–N_2 but not for Fe–N_2. Second-order perturbation analysis of the Kohn–Sham matrix in the NBO basis shows that back bonding, defined as the interaction between occupied π-type NBO orbitals with unoccupied π*-type NBO orbitals of N_2 is stronger for V than for Fe. Summing the contribution from orbitals with occupations greater than 0.8 electrons, the total back-bonding interaction is 32 kcal/mol for V–N_2 and 13 kcal/mol for Fe–N_2. Given its predicted N_2/CH_4 separation capabilities rationalized above, we have initiated efforts to synthesize V-MOF-74. To date the isolation of crystalline material, rather than amorphous powders (as determined by powder X-ray diffraction), has proven elusive, highlighting another MOF challenge: the need for a greater understanding of the poorly understood mechanisms by which metal-organic frameworks form. The present computational results strongly motivate continued efforts to realize both of these goals.

2.1.4 Conclusions

We predict that nitrogen separation from methane can be effected by the as-yet-unsynthesized V-MOF-74, because the vanadium ions in this MOF have their interaction energies significantly increased by π back bonding with N_2, but not with CH_4. This provides a new M-MOF-74 target as a challenge to synthesis. Our qualitative analysis is placed on a quantitative footing by a variety of density functional and wave function calculations of relative binding energies, using models validated against experimental binding energies for the analogous Fe-MOF-74. Density functional calculations are also analyzed to provide detailed insights into bonding distances, charge transfer, vibrational frequency shifts, and orbital interactions.

2.1.5 Acknowledgements

These authors (KL, WCI, ALD, PV) contributed equally.

We gratefully acknowledge Xuefei Xu, Joshua Borycz, Rémi Maurice, Robert Berger, Roberta Poloni, James Phillips, and Pere Miró for helpful discussions.

This research was supported by the U.S. Department of Energy, Office of Basic Energy Sciences, Division of Chemical Sciences, Geosciences, and Biosciences under award DE-FG02-12ER16362. Portions of this work were performed at the Molecular Foundry, supported by the Office of Science, Office of Basic Energy Sciences, of the U.S. Department of Energy under Contract No. DEAC02-05CH11231. Portions of the computations were performed using NERSC.

W.C.I. is grateful for a Kenneth E. and Marion S. Owens Endowed Fellowship. A.L.D. is grateful for support through the Louise T. Dosdall Fellowship. M.R.H. acknowledges the NIST NRC Postdoctoral Fellowship research program for support. E.D.B. was supported by a Gerald K. Branch fellowship in chemistry. P.V. acknowledges a Phillips 66 Departmental Excellence Fellowship.

2.1.6 Notes and References

Notes

No competing financial interests have been declared.

Supporting Information. More details about the calculations, power diffraction experimental data, and gas adsorption measurements are available free of charge via the Internet at http://dx.doi.org/10.1021/ja4102979.

References have been collected at the end of the thesis.

2.2 Predicting Paramagnetic ^{1}H NMR Chemical Shifts and State-Energy Separations in Spin-Crossover Host-Guests Systems[†]

2.2.1 Introduction

Paramagnetic nuclear magnetic resonance (NMR) spectroscopy can be a useful tool for assessing the structure and speciation of high-spin transition-metal coordination compounds in the solid state and solution.[5, 86-91] In the case of proton-bearing organic ligands coordinating to a high-spin center, the sensitivity of ^{1}H chemical shifts to the distance of individual protons from the paramagnetic nucleus makes this spectroscopic technique well-suited for the evaluation of small structural differences that take place in molecules as a result of an external stimulus, for example, the variation in structure of a metal-organic host that might occur following complexation of a suitable guest.[92]

A reliable magnetic indicator for guest binding would be a valuable tool for studying spin crossover (SCO) phenomena in solution and the solid state, indeed this concept has been applied to study anion complexation to metal receptors.[93, 94] One desirable magnetic response to guest encapsulation would be the transition from a diamagnetic state to a paramagnetic state (or vice versa), as demonstrated by Ono *et al.*, where a Ni^{II}-containing guest changes spin state upon encapsulation.[95] If the spin crossover was to occur in the host upon encapsulation, one could perform a variety of host-guest studies, followed by the magnetic transition. Given that iron(II) has been the focus of many single molecule or nanocrystalline magnet studies,[96-110] and that iron(II) is a fundamental component of many host complexes,[111] an exploration of the influence of guest encapsulation on an iron(II)-based host complex is a natural next step. Since the Fe(II) SCO phenomena typically involves a change in iron-ligand distances due to changes in electronic structure,[112, 113] guest complexation might be leveraged to alter SCO behavior.

[†] Reproduced by permission of the PCCP Owner Societies

Isley III, William C.; Zarra, Salvatore; Carlson, Rebecca K.; Bilbeisi, Rana A.; Ronson, Tanya K.; Nitschke, Jonathan R.; Gagliardi, Laura; Cramer, Christopher J. *Phys. Chem. Chem. Phys.* **2014**. 16, pp 10620-10628.

Link: http://dx.doi.org/10.1039/C4CP01478B

For a species with a diamagnetic ground state and thermally accessible paramagnetic state, the temperature-dependent paramagnetic chemical shift will depend on the spin crossover energy. It has been shown in the literature for density functional methods that the functional choice, and especially the amount of exact Hartree-Fock (HF) exchange, can greatly affect the predicted spin crossover energetics of iron(II) complexes.[9, 114-120] Wave function theory *ab initio* methods, including CASPT2, can be extremely demanding in terms of computational resources but can also produce more accurate results when applied in a fashion that takes advantage of their systematic improvability.[121, 122]

While spectroscopic data are sufficient to make general inferences with respect to relative separations of magnetic nuclei, the combination of paramagnetic NMR spectroscopy and quantum chemical calculations offers the opportunity to gain further insights at the molecular level of detail. Indeed, spectroscopy and computational predictions have been used in conjunction to investigate spin crossover (SCO) complexes previously.[123-125] In the present work we assess the accuracy of a particular density functional protocol for the prediction of ^{1}H chemical shifts in iron(II) and cobalt(II) coordination compounds analogous to those known to be useful as vertices for metal-templated self-assembled molecular cages.[106, 126] The sensitivity of the chemical shifts to local structural changes and the utility of the DFT protocol for interpreting spin-crossover behavior in iron-based systems are also examined. Given the importance of predicting an accurate high-spin (HS) – low-spin (LS) splitting energy ($\Delta E_{\text{HS-LS}}$) and that $\Delta E_{\text{HS-LS}}$ are notoriously difficult to predict for iron spin crossover complexes (SCO),[9] special emphasis is placed on benchmarking and characterizing methodological dependence on $\Delta E_{\text{HS-LS}}$ as a function of the coordination environment.

2.2.2 Results and Discussion

Cobalt(II). We begin by considering the tetrahedral $[M_4L_6]^{4-}$ cobalt-based cage **A**[127] shown in Figure 2.2.1. This tetrahedral cage with sulfonated ligands has been synthesised with other metal cations such as iron, and nickel.[111, 127] The solution-state ^{1}H NMR spectroscopy and the X-ray characterisation of cage **A** were previously described.[127]

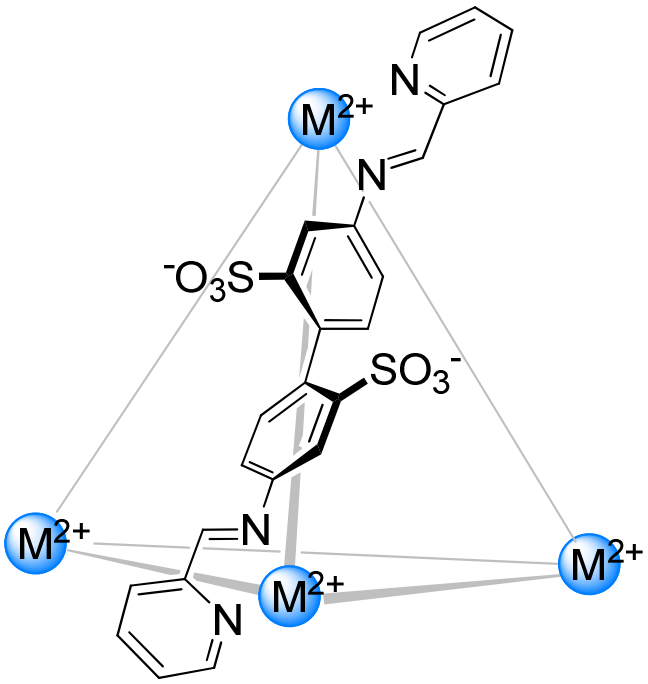

Figure 2.2.1: Sulfonated tetrahedral $[M_4L_6]^{4-}$ cage, where M = Co^{II} (A) or Fe^{II} (B). Each edge of the tetrahedron represents the bis-bidentate ligand L shown.

As quantum chemical computations for the full cage **A** would be extremely demanding and likely multiconfigurational, and as the spin centres are expected to have negligible communication over the distances that separate them,[128] we chose to model the mononuclear complex corresponding to a corner, namely, $[Co(\mathbf{1})_3]^{1-}$ and the non-functionalised analogue $[Co(\mathbf{2})_3]^{2+}$ (see Scheme 2.2.1 for ligand labelling and position numbering scheme). To benchmark the accuracy of the DFT paramagnetic NMR modelling protocol, a high-spin (HS) truncated cage corner model is compared to experimental chemical shift values measured for the cage **A**.

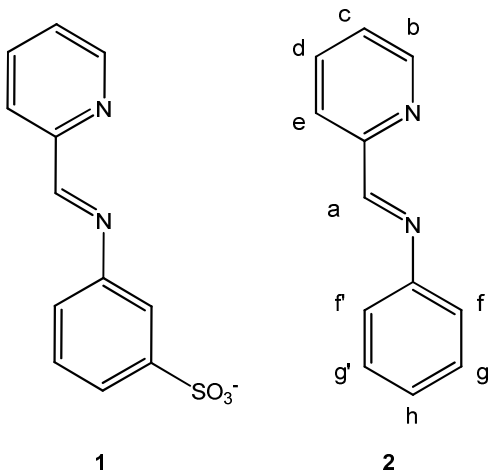

1 2

Scheme 2.2.1

$[Co(1)_3]^{1-}$. The optimised structure for the high-spin quartet state of $[Co(\mathbf{1})_3]^{1-}$ has bond lengths of 2.19 and 2.15 Å averaged over the three equivalent bonds to the imine and pyridine nitrogen atoms, respectively. We note the presence of Jahn-Teller distortion in the optimised geometry. The high-spin quartet state is the only state we have observed *in situ* for cobalt(II) tris(pyridylimine) complexes,[127, 129] and the calculated $[Co(\mathbf{1})_3]^{1-}$ structure compares favourably with experimentally-observed structural features of cage **A**. The X-ray crystal structure of cage **A** with encapsulated tetrahydrofuran (THF)[127] exhibits average Co–N distances of 2.15 and 2.13 Å between imine and pyridine N atoms, respectively.

The ^{1}H NMR chemical shifts for the optimised quartet structure of $[Co(\mathbf{1})_3]^{1-}$ are presented in Table 2.2.1. Due to the presence of Jahn-Teller distortion that breaks the C_3 symmetry, the computed ^{1}H chemical shifts differ for equivalent protons on each linker. Under the assumption that thermal interconversion between equivalent minima will be rapid, we average the chemical shifts for equivalent protons as described in the experimental section. Here we note that the imine (H_a) and py-6 (H_b) protons exhibit the chemical shifts that are most sensitive to the paramagnetic centre. For all Co^{II} systems, predicted H_b chemical shift values were much larger than the experimentally measured ones. Neither increasing the H_b distance from the paramagnetic centre, nor the inclusion of explicit solvent molecules, yielded an

improved agreement of the H_b chemical shift with the experimental shift. This significant over prediction has been observed by Rastrelli *et al.* for the S=1 $[Ni(py)_6]^{2+}$ system.[6]

Paramagnetic NMR predictions reported in the literature tend to overestimate observed chemical shifts;[130] thus, scaling of predicted chemical shifts to match experimental measurements should yield a model with improved predictive abilities. A linear regression (plotted in Figure S1) of the predicted chemical shifts for $[Co(\mathbf{1})_3]^{1-}$ on the ^1H NMR spectra of the host cage **A**[127] yields $\delta_{fit} = 0.9790(\delta_{pred}) - 4.02$ with associated $R^2 = 0.9697$ (additional discussion of the linear regression is provided in the Supporting Information). The linear regression demonstrates that the current modelling protocol has remarkably good agreement with experimental measurements.

The average predicted value for H_a ^1H (δ_{fit} = 251.3 ppm) is referenced to that measured for empty cage **A** (244.0 ppm) and also comparable to cage **A** encapsulating 2-pyridine-carboxaldehyde (238.2 ppm). Given the large paramagnetic shift, and its sensitivity to structural changes (*vide infra*), we consider the agreement within the range of previously reported differences between predicted and experimental ^1H δ.[4, 6] It is noteworthy that upon experimental guest encapsulation, the imine proton signal shifts upfield. This is postulated to result from an expansion of the imine bond ^1H – Co distance upon guest encapsulation.

$[Co(2)_3]^{2+}$. A comparison of the predicted chemical shifts between the sulfonated model complex $[Co(\mathbf{1})_3]^{1-}$ and the unsubstituted model complex $[Co(\mathbf{2})_3]^{2+}$ indicates qualitative agreement.[129] Given that the calculated NMR spectrum of $[Co(\mathbf{2})_3]^{2+}$ shows very close agreement with that of $[Co(\mathbf{1})_3]^{1-}$,[129] we studied the less complex model in the case of iron(II), with the neutral ligand **2** instead of the larger and anionic ligand **1**.

Table 2.2.1 B3LYP chemical shifts for $[Fe(\mathbf{2})_3]^{2+}$ structure for all spin multiplicities, $[Co(\mathbf{1})_3]^{1-}$, $[Co(\mathbf{2})_3]^{2+}$ and experimental ^1H chemical shifts for the cage A[127] analogous to $Co(\mathbf{1})_3^{1-}$. All chemical shifts are reported in ppm.

	Experimental Co^{II}			Predicted Co^{II}		Predicted Fe^{II}				
	Solvated **A**	Guest⊂**A**	$[Co(\mathbf{2})_3]^{2+}$	$[Co(\mathbf{1})_3]^{1-}$	$[Co(\mathbf{2})_3]^{2+}$	$[Fe(\mathbf{2})_3]^{2+}$				
^1H Position[a]	S=3/2 δ_{expt} [b,e]	S=3/2 δ_{expt} [b,e,f]	S=3/2 δ_{expt} [b,g]	S=3/2 δ_{fit} [b,c,d]	S=3/2 δ_{fit} [b,c,d]	S=0 δ [b,c]	S=1 δ_{fit} [b,c,d]	S=2 **Q**$_1$ δ_{fit} [b,c,d,h]	S=2 **Q**$_2$ δ_{fit} [b,c,d,i]	S=2 **Q**$_3$ δ_{fit} [b,c,d,j]
H_a (Imine-C)	244.0	238.2	240.6	251.3	247.0	9.4	68.2	244.5	247.4	259.4
H_b (Py-6)	88.6	88.6	88.5	155.8	172.9	8.2	61.5	175.9	167.2	167.0
H_c (Py-5)	74.3 [k]	74.9 [k]	74.0 [k]	50.0	56.6	8.2	23.8	63.5	65.3	62.0
H_d (Py-4)	17.1	17.1	16.6	15.8	19.8	8.9	21.1	18.2	16.6	10.1
H_e (Py-3)	52.8 [k]	52.8 [k]	52.4 [k]	47.5	52.0	9.0	17.0	59.8	56.4	61.4
H_f (Phe-2)	-7.6 [k]	-5.7 [k]	-21.2	-12.8	-12.8	6.6	-3.8	-10.9	9.4	-10.8
$H_{f'}$ (Phe-2')	-44.0 [k]	-41.6 [k]	-21.2	-15.4	-25.4	4.6	-5.7	-21.9	-7.8	-10.2
H_g (Phe-3)	--	--	10.1	--	11.6	7.8	6.5	12.2	13.7	14.4
$H_{g'}$ (Phe-3')	20.5	20.5	10.1	18.3	23.4	7.6	7.9	21.3	16.2	19.1
H_h (Phe-4)	--	--	-12.0	-10.8	-15.8	8.0	-2.4	-14.4	-4.6	-7.9

[a] See Scheme 2.2.1 for position labelling. Values are averages over the three chemically equivalent positions in the complex. [b] Relative to TMS. [c] Computed for mononuclear cage corner model. [d] Rescaled chemical shifts according to linear regression $\delta_{fit} = 0.9790(\delta_{pred}) - 4.02$. [e] Measured for A.[127] [f] Measured for A with bound 2-pyridinecarboxaldehyde.[127] [g] Measured for $[Co(\mathbf{2})_3]^{2+}$. Chemical shifts for the *facial* isomer are listed.[129] [h] Quintet structure Q_1 [i] Quintet structure Q_2 [j] Quintet structure Q_3 [k] Based on the comparison between theory and experiment, the experimental assignments of the two ^1H pairs (py-3 / py-5) and (phe-2 / phe-2′) are swapped.

Iron(II). Having assessed the quantitative utility of the computational model for the cobalt cage above, we turned next to iron-based systems. These are more difficult to treat in practice than their Co^{II} congeners because at experimental temperatures more than one spin state may be thermally populated for the iron-based systems. Under such circumstances, spin crossover will lead to observation of NMR chemical shifts averaged over the states. The experimental ground state for Fe^{II}-containing cage **B** is largely the singlet diamagnetic state, with a very small population of paramagnetic character affecting NMR spectra. We show below that the S=2 spin state is the most accessible paramagnetic state, and produces a paramagnetic shift that agrees with experimental spin crossover data.

$[Fe(2)_3]^{2+}$. The optimised structure for the low-spin singlet state of the $[Fe(\mathbf{2})_3]^{2+}$ complex has Fe–N bond lengths of 1.99 Å for both pyridine and imine nitrogen atoms, averaged over the three equivalent bonds of each type. These distances agree with experimentally measured bond distances from the X-ray crystal structure of the sulfonated cage[111] (1.986(6) Å and 1.972(5) Å, for the pyridyl and imine bonds respectively), and also reinforces the assumption that the local environment of the metal centre is accurately reproduced after truncation of the cage structure to a single corner.

The vertical triplet-singlet splitting at the singlet global minimum is computed to be 29.6 kcal mol^{-1} at the CASPT2 level and 29.2 kcal mol^{-1} at the M06-L level (see below for further comparison of spin-state energies as a function of computational protocol). Optimisation with M06-L along the S=1 potential energy surface leads to a local triplet minimum that is 16.8 kcal mol^{-1} higher in free energy at the M06-L level than the S=0 ground state. As this large energy separation renders the triplet state effectively inaccessible to thermal population at 298 K, we will not consider it further although predicted chemical shifts are provided in Table 2.2.1 for completeness.

Table 2.2.2: Calculated Properties of the $[Fe(2)_3]^{2+}$ structure for all spin multiplicities.

	S=0	S=1	**Q**$_1$ S=2	**Q**$_2$ S=2	**Q**$_3$ S=2
ΔH_{SCO}[a]	–	16.8	7.7	4.0	3.7
ΔG_{SCO}[a]	–	14.4	4.2	1.3	0.9
Fe – N_{py} (Å)	1.99	2.08	2.17	2.21	2.19
Fe – N_{im} (Å)	1.99	2.08	2.20	2.18	2.21

[a] Adiabatic transitions to the indicated spin state and geometry were computed at the M06-L level of theory for T = 298 K. Free energies and enthalpies of SCO, reported in kcal mol^{-1}, are referenced relative to the S=0 $[Fe(2)_3]^{2+}$ global minimum energy structure.

The vertical $\Delta E_{HS\text{-}LS}$ associated with the quintet state at the singlet global minimum are computed to be 27.7 kcal mol^{-1} at the CASPT2 level and 36.5 kcal mol^{-1} at the M06-L level. Optimisation with the M06-L functional along the quintet potential energy surface leads to significant Jahn-Teller distortion and multiple local minima. These three minima, **Q**$_1$, **Q**$_2$, and **Q**$_3$, were found to have adiabatic ΔH_{SCO} = 7.7 kcal mol^{-1}, 4.0 kcal mol^{-1}, and 3.7 kcal mol^{-1}, respectively, referenced to the singlet global minimum. For these three optimised spin state structures of $[Fe(\mathbf{2})_3]^{2+}$, ^{1}H NMR chemical shifts are presented in Table 2.2.1. Other calculated properties for $[Fe(\mathbf{2})_3]^{2+}$ are summarised in Table 2.2.2.

Topological Influence of the Host. In order to simulate the possible topological influence of the cage **B** superstructure on $\Delta E_{HS\text{-}LS}$, the triangular base of the host tetrahedron's corner was modelled with the distance between the C_h Phe-4 carbon atoms on separate linkers fixed at the distance determined experimentally from X-ray crystallography. The average experimental inter-ligand Phe-4 C–C distance, as measured from cage **B**, is 6.3 ± 0.2 Å; this compares to an average distance of 5.7 Å on the optimised $[Fe(\mathbf{2})_3]^{2+}$ structure. A constrained optimisation of $[Fe(\mathbf{1})_3]^{2+}$ with each Phe-4 C – Phe-4 C′ distance fixed at 6.3 Å yielded a splayed corner (SPC) structure. The free energy required to splay the corner from the ground state structure is predicted to be very small, ΔG_{splay} = 0.2 kcal mol^{-1}. Splaying the corner reduces the vertical spin splitting by 2.1 kcal mol^{-1}, which demonstrates that splaying the corner has a small change in SCO properties. The computed vertical spin state splittings at the M06-L level are ΔE_{HS-LS}^{SPC}= 34.4 kcal mol^{-1} and ΔE_{HS-LS}^{GS} = 36.5 kcal mol^{-1}.

Spin Crossover. Variation of the ^{1}H NMR chemical shifts for the resonances of host **B** and its host-guest complexes with temperature was measured by variable temperature (VT) ^{1}H NMR experiments (see Experimental Methods). In Figure 2.2.2 VT ^{1}H NMR data for the host-guest complex with cyclohexane, $C_6H_{12}\subset$**B**, are reported as a representative example. The protons H_a and H_b were observed to undergo the largest change in chemical shift with temperature due to their proximity to the metal centre (blue and red lines, respectively, in Figure 2.2.2). NMR chemical shifts affected by the spin crossover process have been modelled with Eqn. (1) [124, 131]

$$\delta_{obs} = \delta_{LS} + \left(\frac{C}{T}\right)\frac{1}{1+e^{\Delta G^\circ/RT}} \qquad (2.2.1)$$

where δ_{obs} is the observed chemical shift, δ_{LS} is the low-spin chemical shift, C/T is, to first approximation, the chemical shift of the high-spin state δ_{HS}, T is the temperature, R is the gas constant, and ΔG° is the phenomenological free energy change for the low-spin to high-spin transition. This equation can be used to fit the VT ^{1}H NMR experiments and to extract thermodynamic information about the spin crossover process.

The available experimental temperature range is limited by solvent properties and the degradation of cage **B** at high temperatures. As a result, the fully high-spin chemical shift cannot be obtained experimentally, so theoretical predictions of the chemical shift can be used to improve estimates for the spin crossover thermodynamics. Considering the imine proton, as it did not show any overlap with other signals in the VT NMR experiments, and using the computed values for δ_{HS} of the most stable quintet structure $\mathbf{Q_3}$, fits for the model in Eqn. (1) to VT NMR data obtained from experiment yield ΔH_{SCO} values of 8.8 kcal mol^{-1} and 7.0 kcal mol^{-1} for the empty cage **B** and for **B** encapsulating cyclohexane, respectively. The results for SCO fits of VT imine ^{1}H NMR data are presented in Table 2.2.3 for these and several cases with other guests encapsulated. In each instance, the low-spin chemical shift (δ_{LS}) was taken to be 9.2 ppm as measured experimentally, and the high-spin chemical shift was taken to be 259.4 ppm, which is the theoretically predicted imine shift for the lowest energy quintet state. Further details concerning the fitting procedure can be found in the Supporting Information.

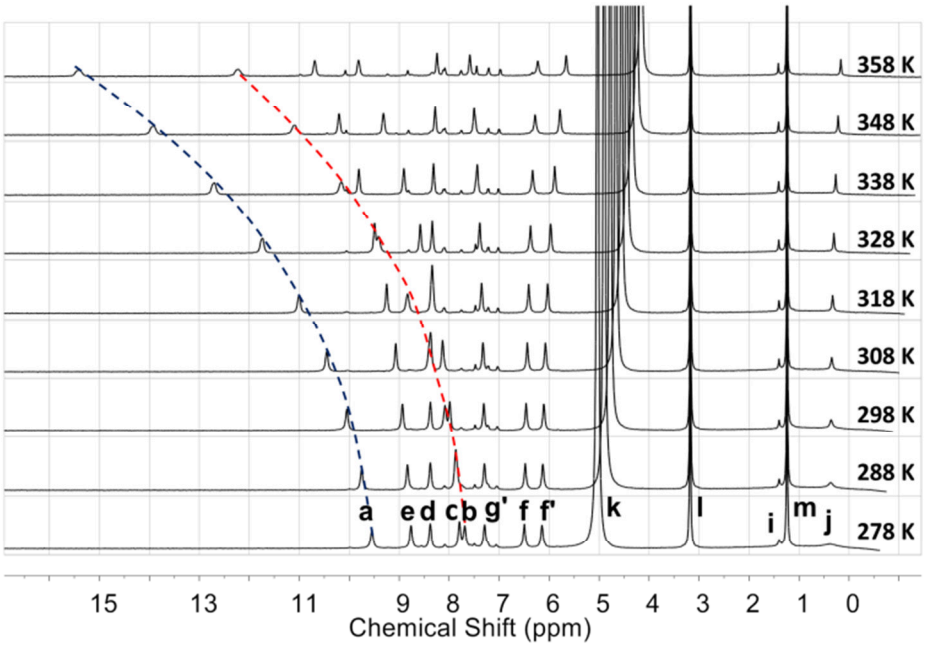

Figure 2.2.2: Stacked plot of ^{1}H NMR spectra for C_6H_{12}⊂B in D_2O acquired at temperatures from 278 (bottom) to 358 K (top) in 10 K steps. Lines are drawn to guide the eye to the changes in chemical shifts of protons H_a (depicted in blue) and H_b (depicted in red). Peak assignments for C_6H_{12}⊂**B** and for free C_6H_{12} are also shown for the spectrum acquired at 278 K. **a-g'**: protons are labelled in Scheme 2.2.1, **i**: free C_6H_{12}, **j**: bound C_6H_{12}, **k**: HDO, **l**: Me_4N^+, **m**: *t*BuOH. At higher temperatures some of the cage (ca. 15% at 358 K) disassembled into its subcomponents through hydrolysis of the imine bonds. The minor peaks corresponding to subcomponents in each spectrum are left unlabelled for clarity.

Guest Influence on Spin Crossover. As indicated in Table 2.2.3, guest binding impacts SCO behaviour; when examining the trends within chemical groups, one can observe trends in ΔH_{SCO} and ΔG_{SCO}. For example, increased Cl substitution on $CH_{4-x}Cl_x$ (x=2,3,4) shows an approximately 10% decrease in ΔG_{SCO} per Cl. Additionally, fluorination of benzene also shows a similar trend, where sequential substitution of F for H yields a sequential reduction in ΔG_{SCO}. However, these effects on SCO are quite small in absolute magnitude and we cannot reliably correlate these variations in SCO with changes in guest volume, polarizability or other guest properties.

We hypothesise that each guest induces a change in the local metal-ligand environment upon binding; however, multi-linear regression analysis to correlate physicochemical properties of the various guest molecules (*e.g.* volume, dipole moment, octanol-water partition coefficient, acidity or basicity) with ΔH_{SCO} did not yield any notable trends. Table S5 contains all physicochemical properties examined, as well as the enthalpy and entropy associated with spin crossover for the iron(II) cage with the listed encapsulated guest.

Table 2.2.3: ΔH_{SCO} and ΔS_{SCO} for the Fe^{II} singlet to quintet transitions as a function of encapsulated guests with the cage B depicted in Figure 2.2.1, fit from VT ^{1}H NMR measurements to Eqn. (1).

Guest	ΔH_{SCO}[a]	ΔS_{SCO}[a]	ΔG_{SCO}[a]
solvent [b]	8.8	14.9	4.4
acetone	6.6	10.7	3.4
tetrahydrofuran	7.0	11.6	3.6
cyclopentane	6.3	10.3	3.2
methylcyclopentane	4.6	7.3	2.4
pyridine	6.5	11.0	3.2
benzene	6.6	11.2	3.2
fluorobenzene	6.1	10.6	3.0
1,2-difluorobenzene	5.8	10.1	2.8
1,4-difluorobenzene	5.1	8.5	2.6
cyclohexane	7.0	12.2	3.4
1,4-dioxane	6.6	10.8	3.3
1,3,5-trioxane	8.4	14.8	4.0
CH_2Cl_2	7.6	12.4	3.9
$CHCl_3$	7.3	12.5	3.5
CCl_4	7.1	12.4	3.3

[a] ΔH_{SCO} and ΔG_{SCO} (T = 298 K) are reported in kcal mol^{-1}. ΔS_{SCO} are reported in cal mol^{-1} K^{-1}. [b] The solvent used was water.

Functional Dependence. We performed a set of tests to improve our understanding of the sensitivity of predicted state-energy splittings to computational protocol, and to validate a practical density functional protocol in order to better survey structural influences on state-

energy splittings. This testing was accomplished through a comparison of various density functional models with the more rigorous CASPT2 model for a series of molecular geometries expected to be relevant to a dynamical cage corner, namely, those associated with systematic variations in the Fe–N_{imine} and Fe–$N_{pyridine}$ distances. Results are presented in Table 2.2.4. When compared to CASTP2 quintet-singlet state-energy splittings, OPBE exhibited the best performance over our 2D surface survey with a mean signed deviation (MSD) of 1.5 kcal mol^{-1} and mean unsigned deviation (MUD) of 2.3 kcal mol^{-1}. Other density functionals that performed reasonably well in comparison to the CASPT2 results were B3LYP with a MSD of 1.9 kcal mol^{-1} and a MUD of 3.1 kcal mol^{-1}, M06-L with a MSD of 6.1 kcal mol^{-1}, a MUD of 6.1 kcal mol^{-1}, and B3LYP* with a MSD of 6.7 kcal mol^{-1}, a MUD of 6.7 kcal mol^{-1}.

The good performance of OPBE for the prediction of state-energy splittings in iron coordination compounds has been previously demonstrated for a number of compounds by Swart.[9] We therefore anticipate that the OPBE predictions for the more expanded corner structures, where CASPT2 predictions become unreliable owing to active space limitations (a symptom of which is demonstrated by the increasingly large difference between the CAS and CASPT2 predicted energy separations), are likely to be the most reliable of those surveyed. M06-L tracks the OPBE predictions for the more expanded corners fairly well, making it a good choice for geometry optimisations that take computational advantage of its local character in these large systems.

B3LYP also tracks OPBE reasonably well for the less expanded corner geometries, but it predicts the quintet state to become the ground state at the largest Fe–N distances. B3LYP* is the only density functional with exact HF exchange that does not predict a quintet ground state at extended coordination shells. In every other case, density functionals containing more exact HF exchange predict an increasingly more stable quintet state. This is consistent with prior literature[114, 115] that have found a linear relationship between $\Delta E_{HS\text{-}LS}$ in iron complexes and the amount of exact exchange included in B3LYP calculations treating exact exchange as a variable, with an optimum functional form for iron $\Delta E_{HS\text{-}LS}$ at 15% exact exchange denoted B3LYP*.[115] Inclusion of the empirical Grimme D3 dispersion correction with Becke-Johnson damping[132] for

B3LYP and PBE increases the favourability of the more compact singlet ground state. This is consistent with previous observations in the literature of spin crossover complexes.[120]

Table 2.2.4: Functional survey of spin crossover electronic energy, $\Delta E_{HS\text{-}LS}$ (kcal mol^{-1}), on a 2D surface of symmetrically varied metal-ligand distances for $[Fe(\mathbf{2})_3]^{2+}$.

X: Fe-Py[a]	GS	2.00	2.00	2.10	2.10	2.10	2.20	2.20
Y: Fe-Im[a]	GS	2.00	2.10	2.00	2.10	2.20	2.10	2.20
CASSCF	20.0	13.6	-5.6	-3.2	[b]	[b]	[b]	[b]
CASPT2	**27.7**	**24.4**	**16.7**	**16.1**	[b]	[b]	[b]	[b]
B3LYP	33.9	28.2	15.0	15.5	4.4	-1.0	-0.6	-3.3
B3LYP+D3	33.9	29.6	18.5	19.2	9.9	1.1	2.2	-1.5
B3LYP*	38.2	32.7	20.3	20.5	10.3	5.7	5.7	3.6
O3LYP	26.8	20.5	7.8	7.3	-3.2	-7.9	-9.1	-10.4
M06-L	36.5	31.7	21.4	19.7	11.2	10.1	7.4	5.0
M06	5.6	0.9	-9.5	-9.7	-18.2	-21.0	-21.3	-23.4
M06-2X	-4.7	-9.5	-24.2	-22.5	-35.6	-42.4	-40.4	-47.0
PBE+D3	48.6	43.9	35.0	34.1	27.1	23.3	22.5	21.0
PBE	48.6	43.0	32.9	31.9	23.9	21.8	20.3	19.6
PBE0	20.1	15.2	3.7	4.1	-5.6	-9.7	-9.4	-12.0
OPBE	**32.9**	**26.9**	**16.5**	**14.7**	**6.3**	**4.2**	**1.1**	**1.7**

[a] Distances are in Å between the metal centre and N atom indicated. GS indicates the unconstrained singlet ground state geometry. [b] In order to treat the expanded coordination system; an active space larger than (10,12) was found to be required, with which further calculations were not undertaken.

Dynamical Effects. Given that ΔH_{SCO} was predicted from the VT NMR data to be 8.8 kcal mol^{-1} for the aqueous cage, and that the predicted *vertical* $\Delta E_{HS\text{-}LS}$ for the ground-state singlet geometry was 27.7 kcal mol^{-1}, we hypothesise that the observed thermal spin crossover must occur as part of a dynamical process. It is well established that high-spin iron(II) complexes have longer metal-ligand bonds than their low-spin counterparts due to the increased ionic radius of the high-spin metal,[133] thus we also explored how systematic variation of Fe–N bond lengths reported in Table 2.2.4 for $[Fe(\mathbf{2})_3]^{2+}$ affects predicted paramagnetic chemical shifts, in addition to state-energy separation. Predicted ^{1}H chemical shifts for the quintet state of $[Fe(\mathbf{2})_3]^{2+}$ along the 2D surface are reported in Table S2.

Spatial variation in the Fe–N_{im} distance correlated strongly with variation in the paramagnetic chemical shift of the imine proton. On average, a 0.05 Å increase in Y, the Fe–N_{im} distance, resulted in a decrease in the imine ^{1}H δ of 38.0 ppm. However, variation in X, the Fe–N_{py} distance, did not strongly correlate with the computed imine ^{1}H chemical shift. On average, a 0.05 Å increase in Y results in a decrease in the imine ^{1}H δ of 0.2 ppm. Considering the sensitivity of the imine ^{1}H δ value to Fe–N_{im} distance, it is important to reconsider the data in Table 2.2.1, which were derived using a single value for imine ^{1}H δ taken from the lowest energy optimised quintet structure. However, if we vary the reference high-spin value from 220 to 280, the variation in the predicted thermodynamic variables of enthalpy and entropy is no more than 0.5% and 5%, respectively. This result indicates low sensitivity to the high-spin chemical shift endpoint in obtaining thermodynamic parameters for SCO using Equation (1).

Figure 2.2.3 plots ΔH_{SCO} as a function of the two Fe–N coordinates. There is a large splitting energy at the ground-state geometry, which is quite close to the symmetrically constrained structure (2.00, 2.00). However, a sharp decrease in ΔH_{SCO} accompanies a slight expansion of the coordination sphere. The high-spin configuration is computed to be much more thermally accessible upon expansion of the coordination sphere to (2.10, 2.10), with ΔH_{SCO} = 9.9 kcal mol^{-1}. Indeed, this predicted ΔH_{SCO} agrees with the measured ΔH_{SCO} from VT NMR within experimental error. From these data, we conclude that spin crossover occurs for expanded corner structures, whose geometries are accessed dynamically at experimental temperatures.

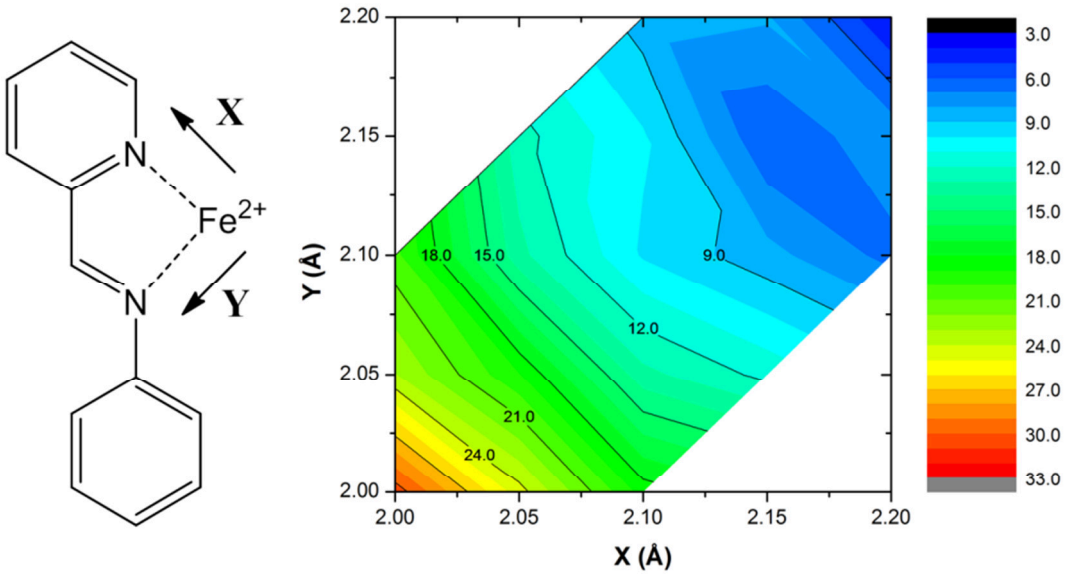

Figure 2.2.3: The M06-L state-energy splitting ΔH_{SCO} for $[Fe(2)_3]^{2+}$ between the singlet ground state structure and the quintet structure optimised with constrained, symmetrically frozen Fe–N bonds. Raw values can be found in the Supporting Information.

Figure 2.2.3 plots ΔH_{SCO} as a function of the two Fe–N coordinates. There is a large splitting energy at the ground-state geometry, which is quite close to the symmetrically constrained structure (2.00, 2.00). However, a sharp decrease in ΔH_{SCO} accompanies a slight expansion of the coordination sphere. The high-spin configuration is computed to be much more thermally accessible upon expansion of the coordination sphere to (2.10, 2.10), with ΔH_{SCO} = 9.9 kcal mol^{-1}. Indeed, this predicted ΔH_{SCO} agrees with the measured ΔH_{SCO} from VT NMR within experimental error. From these data, we conclude that spin crossover occurs for expanded corner structures, whose geometries are accessed dynamically at experimental temperatures.

2.2.3 Conclusions

In this work we have demonstrated the utility of quantum chemical models for the prediction of paramagnetic ^{1}H NMR chemical shifts in molecules incorporating high-spin metal centres. The predicted chemical shifts were consequently used for the prediction of thermodynamic parameters associated with spin-crossover (SCO) processes. We have further

characterised how SCO can be affected by the geometrical expansion of the ligand sphere around Fe^{II} centres. A quantum mechanical survey of spin-state energy splittings suggests that SCO does not occur for molecular geometries near that of the singlet ground state, at which very large state-energy separations are predicted for pyridylimine-based Fe^{II} complexes. However, expansion of the metal coordination sphere reduces ΔH_{SCO} to the point that a high-spin quintet state becomes thermally accessible. This indicates that dynamical access to an expanded metal coordination sphere is necessary for spin crossover. Based on this conclusion, any guest molecule whose encapsulation serves to expand this coordination sphere, or otherwise stabilise the high-spin state, should result in increased high-spin population at a given temperature. We have explored whether variations in ΔH_{SCO} values measured experimentally for different guest molecules correlate with physicochemical properties of the guests themselves, but satisfactory correlations have not been identified. This suggests that the effects of guest binding on SCO properties are more nuanced than may be inferred from static calculations and that further insights will be likely to require dynamical simulations of host-guest complexes in solution and analysis of associated trajectories.

2.2.4 Experimental

Computational Methods.

Optimization and Thermochemistry. Geometry optimisations were performed for all species at the M06-L[63] level of density functional theory. For Fe and Co atoms, the Stuttgart-Dresden (SDD) ECP10MDF [8s7p6d2f | 6s5p3d2f] basis set and associated pseudopotentials[134, 135] were used; the MIDI! basis[136] was used for C, N, and H atoms; the 6-31+G(d) basis was used for S and O atoms. The nature of stationary points was assessed in all cases by computation of analytic vibrational frequencies, which were also used to compute the molecular partition functions necessary to predict 298 K thermochemical quantities using the conventional ideal-gas, rigid-rotator, quantum-mechanical quasi-harmonic-oscillator[137] approximation.[1] Improved electronic energies were computed, as single-point calculations, using the same SDD basis set for Fe and Co but replacing MIDI! or 6-31+G(d), with 6-311+G(2df,p) for all other atoms.

Spin State Separations. Spin state splitting energies were computed at the CASSCF/PT2 level of theory with a (10,12) active space. Further details on these calculations are in the Supporting Information. In addition, several functionals were compared to the CASSCF/PT2 splitting energies including M06-L, M06, M06-2X, PBE, PBE0, B3LYP, B3LYP* O3LYP, and OPBE. The basis set used for these computations was the same as for the improved electronic energies as stated above.

Paramagnetic NMR. For isotropic systems $3d$ metal systems,[3-6, 138] the Fermi contact term is presumed to massively dominate the paramagnetic component of the chemical shift. For further discussion on the nature of the approximations made when computing the paramagnetic chemical shift, please see the Supporting Information. Thus the computed absolute chemical shift becomes

$$\sigma^{iso} = \sigma_{orb}^{iso} - \frac{S(S+1)}{3k_BT}\frac{2\pi\mu_B}{\gamma}g_{iso}A_{FC} \quad (2.2.2)$$

where γ is the gyromagnetic ratio for nucleus K, g_{iso} is the isotropic g-factor, μ_B is the Bohr magneton, A_{FC} is the isotropic hyperfine coupling constant (Fermi Contact HFC) for nucleus K in frequency units (multiply by $\hbar$ if the HFC is in energy units), S is the electronic total spin, k_B is Boltzmann's constant, and T is temperature. σ_{orb}^{iso} is computed, approximately for high spin systems, on the unrestricted system using the diamagnetic formulation for the orbital shielding.[139] The contribution to the orbital chemical shielding introduced by the additional "paramagnetic orbital shielding" term[140] is expected to be small for ^{1}H nuclei, and is not computed in this work. Since σ_{iso} is an absolute chemical shielding, the observable chemical shift becomes

$$\delta = \sigma_{ref} - \sigma_{iso} \quad (2.2.3)$$

where σ_{ref} is the chemical shift of a reference compound, tetramethylsilane (TMS). Before computing δ_{pred}, σ_{orb} and A_{FC} are averaged for equivalent proton groups.

^{1}H chemical shifts δ, referenced to tetramethylsilane (TMS), were computed at the B3LYP level of DFT employing the all-electron 6-311+G basis set[141, 142] for the metal atoms and the EPR-II basis[143] for C, N, H, O and the 6-311+G(2df) basis[144, 145] for S. We chose to use the

B3LYP functional based on previously demonstrated good NMR and EPR performance for metal-containing systems like those studied here.[6]

Hyperfine coupling constants and the *g*-tensor were computed using the DFT level of theory in gas phase within the spin orbit mean field approximation SOMF(1X).[10] The extension for systems with S > ½ using the zero-field splitting interaction is neglected in this work; further discussion on this interaction and its effects on paramagnetic NMR are in the Supporting Information.

Solvation and Software. All optimisation, thermochemistry and σ_{orb} computations were accomplished using the Gaussian09 Rev C.01 suite of electronic structure programs.[74] In all calculations with the Gaussian09 software suite, the effects of aqueous solvation were included using the SMD continuum solvation model.[8] All EPR computations were accomplished in the gas phase using the ORCA 2.9.1 suite[146] of electronic structure programs.

Experimental Methods.

Variable Temperature ^{1}H NMR. Solutions of host cage **B** and its host-guest complexes were prepared as described in the Supporting Information. VT NMR experiments were performed using an automated temperature ramp which consisted of going from 278 K to 358 K in steps of 10 K. After each temperature was reached, 3 minutes for the equilibration of the sample were allowed and a ^{1}H NMR spectrum was acquired (see Figure S6 and Table S4 in the Supporting Information).

2.2.5 Acknowledgements

This work was supported by the UK Engineering and Physical Sciences Research Council (EPSRC), the National Science Foundation (NSF/CHE-1124244) and Schlumberger-Faculty for the Future Fellowship (RAB). W.C. Isley III was supported by the Kenneth E. and Marion S. Endowed Fellowship. We thank Dr P. Mal for preliminary experimental studies and Dr M.M.J. Smulders for useful discussions.

2.2.6 Notes and references

Electronic Supplementary Information (ESI) available. See : http://dx.doi.org/10.1039/C4CP01478B

References have been collected at the end of the thesis.

2.3 The Prediction of ^{19}F NMR in Proteins

2.3.1 Introduction

Protein-protein interactions play a critical role in numerous biological processes, and understanding of these biomolecular interactions can lead to new medical technologies. Of recent interest is the role that protein-protein interactions play in transcriptional regulation and their modulation using small molecules. Bromodomains are a class of protein domains that play a lynchpin role in the DNA transcriptional process; where bromodomains recognize acetylated lysine residues on histones. The acetylation of a lysine on a histone protein is a key signal to start the uncoiling of histone bound DNA increasing its accessibility for transcription Additionally the modification serves as the attachment point of the transcriptional machinery via subsequent -protein-protein interactions with the bromodomain containing protein (see Scheme 2.3.1).[147] A malfunctioning bromodomain can lead to abnormal biomolecular regulation and thus has been observed to play a role in disease pathways.[30] This prevalence in disease has led to the desire to target bromodomain assembly complexes with medicinally active drugs.[148] Bromodomains were considered to be undruggable until 2010 when development of bromodomain and extra terminal domain (BET) inhibitors JQ1[149] and IBET-762[150] sparked development of therapeutic targets for the 61 known bromodomain containing proteins.[151] The JQ1 and IBET-762 molecules showed non-specific inhibition across a subclass of bromodomains, which is undesirable as inhibition to a specific bromodomain is the desired therapeutic target. Since then the bromodomain field has rapidly developed, with five bromodomain inhibitors currently in clinical trials.[148]

In order to design a medicinally active drug targeting bromodomains, one must first understand the protein-protein interface. The intermolecular interfaces between proteins are often large and featureless in nature, specifically lacking the deep hydrophobic pockets that have facilitated development of previous high affinity small molecules[152] and resulting in challenging experimental characterization and even more difficult drug design. A current method to probe this interface is fragment based drug discovery, which focuses on detecting the interactions of small, low-affinity ligands, and further developing those into higher-affinity probes. The

challenges for studying such a weak interaction with a small fragment-like molecule are three fold to determine if and how strongly the probe has bound to the protein-protein interface. 1) The first is to selectively characterize the correct binding site, there are many possible surface binding sites; 2) second is to accurately characterize the complexation strength; 3) and finally, throughput speed is essential given that the molecular fragment screening requires a significant number of experiments.

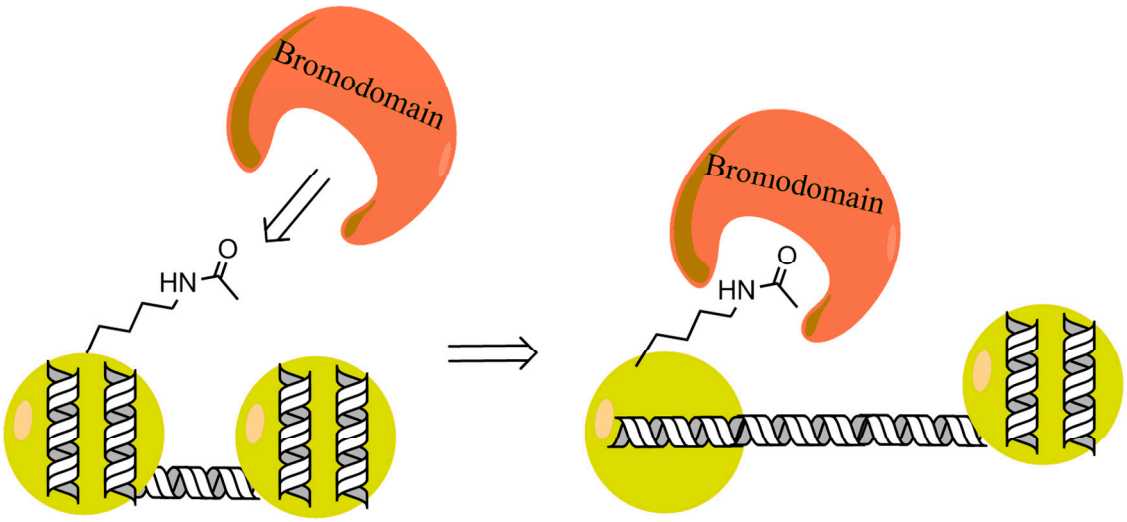

Scheme 2.3.1: Representation of bromodomain binding to DNA wrapped histone, and the subsequent uncoiling of DNA from histone.

These challenges led to the development of a dynamic spectroscopic method that is highly sensitive to changes in the environment at the interface called Protein Observed Fluorine (PrOF) NMR.[153-156] The method achieves the desired selectivity and accuracy through fluorination of aromatic side chain residues. Residues with aromatic side chains have demonstrated enriched population at protein-protein interfaces,[157] therefore a method that is sensitive to changes in this environment would monitor binding interactions. Given that ^{19}F NMR is hyper responsive to local environmental changes and has a strong signal due to fluorine's high gyromagnetic ratio ($\gamma_F / (2\pi) = 40.052$ MHz T^{-1}), rapid acquisition of 1D interpretable spectra is possible.[153] The PrOF NMR method is approximately 2-3 times faster than the commonly used 2D ^{1}H ^{15}N heteronuclear single quantum coherence (HSQC) NMR methods for bromodomain proteins. Collectively, these satisfy the challenges involved in the

detection of weak intermolecular complexes,[153, 154] and have been utilized to screen for new molecular inhibitors.[155]

Unfortunately the PrOF NMR experimental spectra are difficult to characterize, and theoretical prediction of the protein's ^{19}F NMR spectra would greatly assist in the development of new bromodomain inhibitors. The experimental challenge comes from the assignment of each ^{19}F NMR spectral peak, which requires site-directed mutagenesis to modify a single residue such that it will not be fluorinated, and observing which resonance disappears in the PrOF NMR spectrum.[153] Through sequential mutagenesis of residues, one can assign the PrOF NMR spectrum. Overlapping resonances can be extremely challenging to assign, and computational predictions could provide additional assistance.[158] Generation of mutant proteins comes with its own challenges such as protein misfolding or difficulty in protein expression. Once an initial PrOF NMR spectrum has been assigned, screening assays for molecular probes can lead to structural insight into the mode of inhibition of the macromolecular protein-protein interactions. A theoretical method that could assist in the assignment of bromodomain PrOF NMR spectra would provide a significant boon for experimental characterization, and could be extensible to other proteins.

This work will demonstrate that automation of spectral predictions for ^{19}F NMR in bromodomain proteins is possible, but remains a challenging problem to tackle. We will demonstrate that a cluster based method for prediction of ^{19}F NMR shows great promise for further study. While traditional predictions of PrO ^{1}H NMR involve dynamic simulations to sample the large ensemble of configurations, the relative rigidity and availability of X-ray crystal structures for bromodomain proteins lends itself to an exploratory cluster based model.

2.3.2 Results and Discussion

To the best knowledge of the authors, a benchmarking study for the accuracy of ^{19}F NMR predictions of biomolecular moieties is unavailable for density functional methods. To ensure accurate predictions, and validate the protocol chosen for ^{19}F NMR predictions, a training set was used to correlate various modeling protocols with experimental measurements. Once these protocols were determined to correlate strongly with the experiments, we proceeded

to cut clusters cut from proteins and predict the ^{19}F NMR. Here we discuss the modeling challenges and physical insights into the effects of chemical environment on ^{19}F NMR shifts in proteins.

Training a ^{19}F NMR Prediction Protocol. Prior to cluster generation, a method to predict the ^{19}F NMR of aromatic complexes in the range of 3-fluoro-tyrosine NMR chemical shifts was tested. The training set molecules consisted of aromatic complexes with chemical shifts in the expected ranged spanned by fluoro-tyrosines and fluoro-tryptophans in bromodomains (-125 to -145 ppm relative to $CFCl_3$).[154] The training set and experimental NMR data are reported in Table 2.3.5. The protocols tested include, molecular optimization with M06-L/def2-SVP in either the gas phase or with an aqueous SMD solvation model. After these structures were obtained, NMR predictions were performed using either the PBE0[159] or B3LYP[160] density functionals in combination with either the EPR-II or EPR-III basis sets[161]. Additionally, NMR predictions were made at the Hartree Fock level of theory using 6-311++G(2d,2p)[144, 162] basis sets and the aqueous SMD solvation model.

Table 2.3.1: Performance of predicted ^{19}F δ Prediction Protocols in comparison to Experimentally Measured NMR values of Complexes in Training Set (See Table 2.3.5). All protocols use the SMD solvation model.

Protocol	Intercept	Slope	Adj. R^2
PBE0 /EPR-II	-24.6 ± 5.4	0.860 ± 0.039	0.974
PBE0 /EPR-III	-9.2 ± 7.7	0.930 ± 0.057	0.954
B3LYP/EPR-II	-34.4 ± 5.4	0.809 ± 0.040	0.969
B3LYP/EPR-III	-24.3 ± 8.0	0.897 ± 0.058	0.948
HF /6-311++G(2d,2p)	-109.7 ± 27.9	0.285 ± 0.204	0.068

The results for the regressions between computed ^{19}F NMR on the training set and experimental measurements are shown in Table 2.3.1. Plotted in Figure 2.3.1, the strongest correlation between experimental ^{19}F NMR measurements and predicted ^{19}F NMR was found for the protocol using the aqueous SMD solvation model,[8] PBE0 density functional,[159] and the EPR-II basis set[161]. Given the similar statistical performance between PBE0/EPR-II/SMD and

PBE0/EPR-III/SMD, we chose to move forward with the more inexpensive scaling PBE0/EPR-II/SMD protocol. It is worth pointing out that while previous research has indicated the utility of predicting ^{19}F NMR for fluorobenzenes with the Hartree Fock level of theory,[163] our results with this level of theory highlight a danger, and we strongly recommend using more modern methods to obtain accurate predictions for the PrOF NMR models.

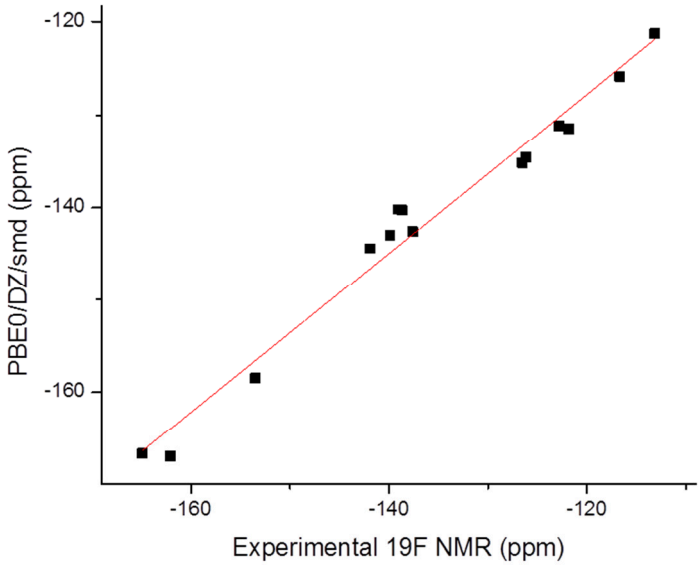

Figure 2.3.1: Predicted δ from PBE0/EPR-II/SMD vs. experimental ^{19}F δ NMR for the training set (see Table 2.3.5).

Cluster Radial Convergence. We note that a more complete representation of the local environment around the 3-fluorotyrosine is optimal for cluster generation cut-off radii between 3.25 Å and 4.00 Å. Residue Y65 of the BRD4 (PDB ID: 4IOR) protein was selected given that is an surface exposed protein which might be subject to dramatically different environments for the different rotamers (interior vs exterior facing fluorine), and particularly relevant for probing surface chemistry. The relative energies and chemical shifts for each conformer are collected in Table 2.3.2. During cluster generation, the proper inclusion of the interior phenolic proton acceptor carbonyl residue occurs after a radial cutoff of 2.75 Å has been reached, and inclusion of external water moieties is reached after 3.25 Å. After both phenolic proton acceptors have been included, convergence of the predicted fluorine NMR begins although the relative stability of each conformer is still in flux. Clusters generated beyond a radial inclusion criteria of 4.0 Å were

found to be prohibitively expensive to compute with the modeling protocol. This leads into some discussion of the various conformers for 3-fluorotyrosine in addition to the fluorine's relative orientations toward the protein interior.

3-Fluorotyrosine Conformer Weights. One challenge for chemical models is to accurately sample all thermodynamically relevant conformers. For the 3-fluorotyrosine systems considered here, there are 2 N accessible conformers, where N is the number of available phenol hydrogen acceptors, and the factor of 2 derives the relative F orientation toward the interior or exterior of the protein. The different conformers expose the fluorine atoms to significant differences in magnetic environments. Figure 2.3.2 highlights the different conformer environments.

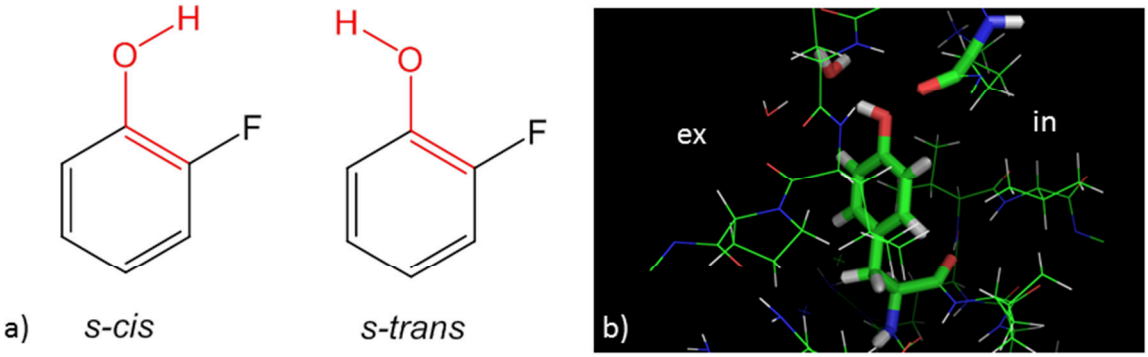

Figure 2.3.2: a) s-*cis* vs s-*trans* conformers b) Brd4 (PDB ID: 4IOR) Residue 65 highlights the difference in environments, interior (in) vs exterior (ex) locations for the fluorine atom.

If there is a single hydrogen bond acceptor, the number of energetically accessible conformers effectively reduces to 2 as non-hydrogen bonded conformers are much higher in energy. When examining the phenol's conformational effect on chemical shift, we notice two different physical effects related to phenolic hydrogen bonding and isomerism. In the absence of any proton acceptors, the s-*cis* (H, F) conformers are slightly favored over the s-*trans* (H, F) conformers. Additionally, it is evident that there is a large difference in the chemical shifts between the relative fluorine-hydrogen orientations. We note that s-*trans* conformers have $\delta_{pred}^{s-trans} \approx$ -130 ppm, whereas the more favorable s-*cis* conformers have $\delta_{pred}^{s-cis} \approx$ -150 ppm.

Once explicit hydrogen bond acceptors are present the disparity in chemical shifts due to the s-*cis* vs s-*trans* isomerism is dramatically reduced.

An example case showing the convergence of the chemical shift with respect to cluster size is shown in Table 2.3.2. For residue Y65, there are four accessible conformers, as there are two phenolic hydrogen acceptors: (1) external water, and (2) interior peptide backbone carbonyl. As the cluster converges radially toward the protein environment, it becomes clear that the most favorable conformer is the external fluorine, with the s-*trans* phenolic proton hydrogen bound to the interior peptide carbonyl.

Accurately Modeling the Phenolic Environment. Accurate modeling of the phenolic proton environment is a critical challenge for the accurate prediction of the 3-fluoro-tyrosine ^{19}F NMR. Indeed, one can see the effect a singular explicit water molecule has on the predicted F NMR (See Table 2.3.2). The influence of the phenolic hydrogen acceptor has a significant impact on the ^{19}F chemical shift. Inclusion of only the proton acceptor is problematic, particularly for charged residues with adjacent ion pairs. This is exemplified by clusters where the target 3-fluorotyrosone has a phenolic hydrogen bond to a negatively charged aspartate or glutamate carboxylic acid residue. The anionic H-acceptor, in absence of the positive ion paired residue, yields more electronic density on the fluorine, and a further upfield shift. For 3FY 118, a cluster of radius 3.00 Å has a chemical shift of -148.5 ppm. Inclusion of the arginine ion pair at a cluster radius of 4.00 Å, dramatically reduces the predicted chemical shift to -140.8 ppm.

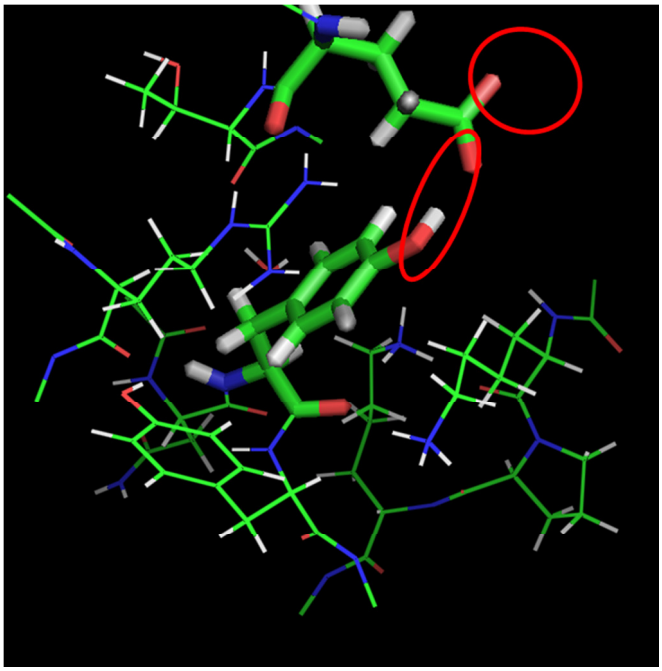

Figure 2.3.3: Brd4 (4IOR) Residue 118 with hydrogen bond to glutamate 49. Note that there is a missing arginine ion pair in the empty circle opposite the carboxylate from the phenol.

^{19}F NMR Predictions for 3-fluorotyrosine mutant BRD4. Using a radial cutoff for cluster generation of 4.0 Å, the ^{19}F NMR spectra was simulated for the entire fluorinated mutant protein. Results are shown in Table 2.3.3. The effects of additionally optimizing nearby water molecules are shown in Table 2.3.4. One can clearly see that optimization of the fluorinated tyrosine is insufficient to predict the relative peak positions. Some residues are predicted quite close to experiments, including Y118 and Y97, however some are dramatically off Y98, Y65, Y137, and Y139.

Closer examination of these clusters revealed that explicit water molecules were quite close to the phenol. While water positions were previously optimized with a molecular dynamic protocol prior to cluster generation, the sensitivity of the chemical shift to the isomerization led us to test further optimization of adjacent water molecules to improve the predictive capabilities of the model. Y65 has two water molecules directly participating in hydrogen bonding interactions. Y97 has no water molecules directly interacting with the phenol. Y98 has one water molecule participating in a hydrogen bond with the phenol. Y118 has one water molecule

directly participating in a hydrogen bond with the phenol. Y119 has one close proximity water molecule, but it does not participate in hydrogen bonding with the phenol. The s-trans-ex configuration converges to the s-cis-ex configuration, as the phenolic hydrogen rotates to bond with the neighboring carboxylate ligand. Y137 has sodium and two waters directly interacting with the phenol. Y139 has two waters and a sodium atom near the residue with water participating in hydrogen bonding to the phenol. Y98 exhibits pathologically different behavior than experimental measurements. For this model of Y98, only one water molecule is found near the residue, compared to the protein XRD where a cluster of four waters is near. Given this, it's possible that an extended hydrogen bonding network to the phenol can influence the chemical shift of this fluorine.

Y137 does not have an "interior" configuration. This is because the fluorine would be pointed directly at a carboxylate side chain, and is an extremely high energy configuration. Let us see the effect that optimizing water has on the chemical shift of the fluorinated tyrosine. If we exclude Y98, which shows pathologically incorrect behavior, the MUD from experimental before optimizing water is 4.3 ppm vs 4.0 ppm. However, we see significant improvements for the protocol when water is optimized along with the target residue if we consider only the conformer that is closest to experimental measurements. The MUD now becomes 1.4 ppm. This demonstrates that the protocol can predict the fluorine environment in the bromodomain quite close to experimental results. However, further benchmarking should be performed on the prediction of relative conformer energetics.

The predicted most stable configurations are shown in Figure 2.3.4. The s-*trans*-ex conformer is predicted to be the most stable conformer for all residues except Y97 and Y98 where the s-*cis*-in conformer is more stable. Interestingly, the predicted environment that matches experiments closest for four out of seven residues is the s-*cis* isomer. The residues where water does not participate in phenolic hydrogen bonding (Y97, Y118) have the only lowest energy configuration with that matches experimental chemical shifts. In applying this to further systems, these peaks should have the highest reliability of prediction.

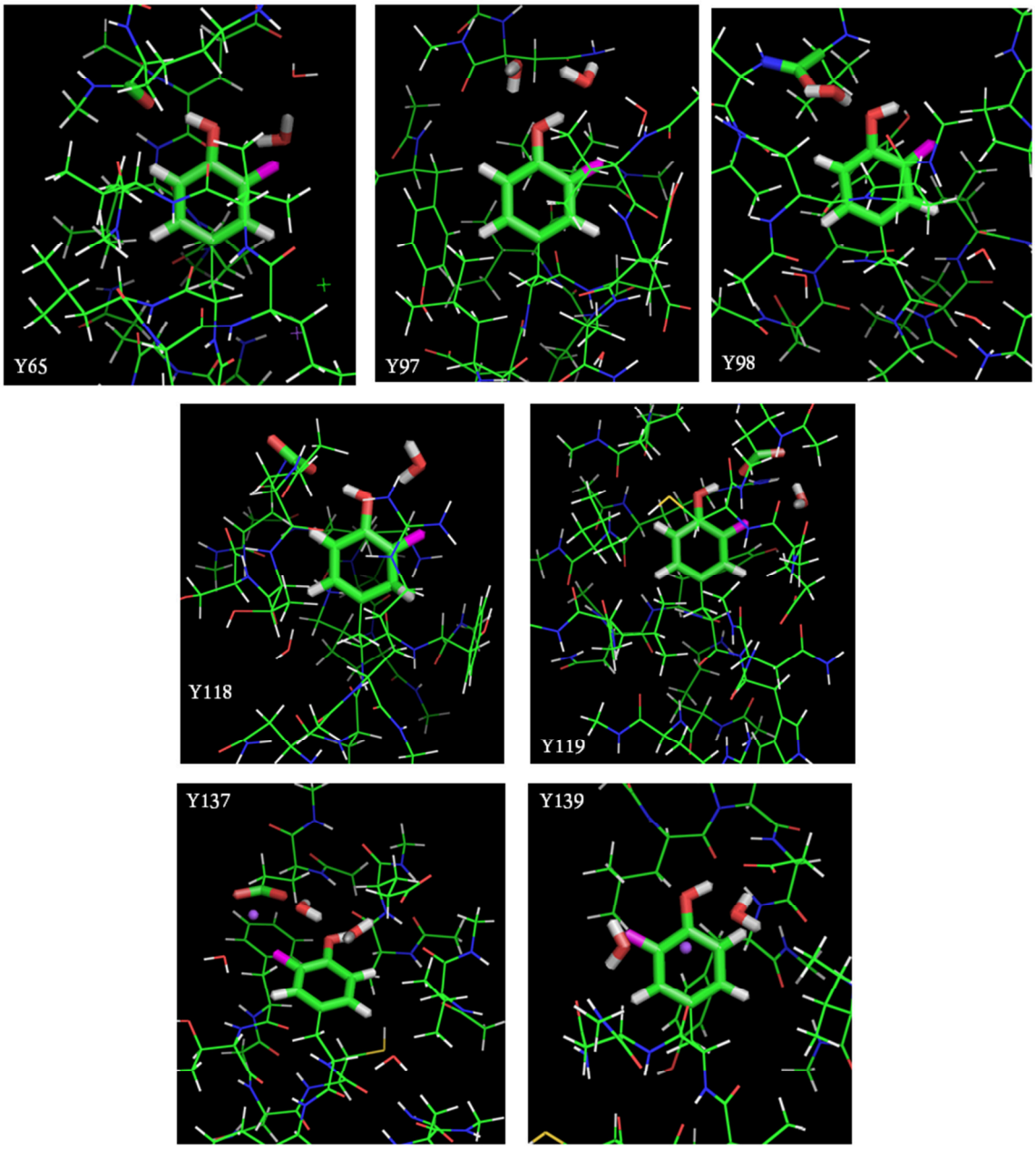

Figure 2.3.4: Lowest energy configurations of 3-fluorotyrosine clusters. Y65 shows the s-cis-ex, Y97 shows the s-trans-ex, Y98 shows the s-trans-ex, Y118 shows the s-cis-in, Y119 shows the s-cis-ex, Y137 shows the s-trans-ex, Y139 shows the s-trans-ex. Fluorine atoms are highlighted in magenta.

Table 2.3.2: Radial convergence of 19F NMR δ (ppm) as a function of isomeric environment.[a]

R (Å)	# AA[a]	# PP[b]	$\Delta E_{(s\text{-}cis\text{-}in)}$ kcal/mol	$\Delta E_{(s\text{-}trans\text{-}ex)}$ kcal/mol	$\Delta E_{(s\text{-}cis\text{-}ex)}$ kcal/mol	^{19}F NMR δ (ppm)[d] s-*trans*-in.	s-*cis*-in	*s-trans*-ex	s-*cis*-ex.	δ_{pred} (ppm)
2.00	2	1	-2.85	0.06	-2.65	-133.8	-153.3	-133.5	-152.2	-152.5
2.25	2	1	--	--	--	--	--	--	--	--
2.50	5	1	-2.63	-2.26	-3.92	-137.0	-156.3	-136.1	-153.8	-155.0
2.75	6	2	0.00	-0.46	3.97	N/A	-130.9*	-146.7*	-149.6	-141.7
3.00	8	3	0.01	-1.57	6.32	N/A	-132.1*	-136.5*	-145.8	-136.2
3.25	11	2	-2.96	-4.33	-2.26	-121.0**	-122.5*	-129.4*	-133.9**	-129.6
3.50	11	2	--	--	--	--	--	--	--	--
3.75	14	3	-3.56	-4.97	-2.59	-121.0**	-127.9*	-132.4*	-136.6**	-132.1
4.00	14	3	--	--	--	--	--	--	--	--
EXP	--	--	--	--	--	--	--	--	--	**-137.4**

[a] The isomeric environments are separated into interior (in.) vs exterior (ex.) and s-*cis* vs s-*trans*, (see Figure 2.3.2a). [b] The number of residues describes the number of residues kept with side chains intact (does not include caps). [c] The number of disconnected peptide chains is denoted by the number of chains. [d] δ_{pred} is the Boltzmann weighted ^{19}F NMR chemical shift for 3-fluorotyrosine at residue Y65 of BRD4 (PDB ID: 4IOR). *Denotes that a hydrogen bond to the carbonyl oxygen of adjacent peptide. **Denotes a hydrogen bond to external water.

Table 2.3.3: Conformer configurations, energetics, and NMR predictions for tyrosine residues in BRD4. Only the fluorinated tyrosine residue is optimized for these models.

Residues				$\Delta E_{(s\text{-}cis\text{-}in)}$	$\Delta E_{(s\text{-}trans\text{-}ex)}$	$\Delta E_{(s\text{-}cis\text{-}ex)}$	^{19}F NMR δ (ppm)[d]					δ_{exp}
AA	# AA[a]	# PP[b]	R	kcal/mol	kcal/mol	kcal/mol	s-*trans*-in.	s-*cis*-in	*s-trans*-ex	s-*cis*-ex.	δ_{pred}	
Y97	13	4	4.00	5.10	6.69	2.32	-137.4	-145.4	-126.5	-129.2	-137.3	**-140.1**
Y118	12	4	4.00	--	0.00	4.39	--	--	-140.8	-140.6	-140.8	**-138.0**
Y65	14	3	4.00	-3.56	-4.97	-2.59	-121.0	-127.9	-132.4	-136.6	-132.1	**-137.4**
Y98	14	3	4.00	-0.13	9.52	10.15	-121.6	-120.1	-121.1	-129.0	-120.8	**-136.6**
Y139	10	3	4.00	-9.41	-13.28	-4.43	-119.0	-117.3	-143.0	-148.9	-142.9	**-136.6**
Y137	11	4	4.00	10.00	6.79	-3.49	-116.3	-119.4	-136.7	-140.8	-140.7	**-134.0**
Y119	14	7	4.00	11.18	--	-0.31	-119.4	-121.0	--	-122.6	-122.0	**-128.0**

Table 2.3.4: Effects of optimizing nearby water molecules on conformer configurations, energetics, and NMR predictions for tyrosine residues in BRD4. The number of directly interacting water molecules is labeled #H_2O, where * means it does not hydrogen bond with the phenol. Chemical shifts in italics are for the most favorable predicted conformers, whereas bold denotes the closest to experimental shifts.

Residues				$\Delta E_{(s\text{-}cis\text{-}in)}$	$\Delta E_{(s\text{-}trans\text{-}ex)}$	$\Delta E_{(s\text{-}cis\text{-}ex)}$	^{19}F NMR δ (ppm)[d]					δ_{exp}
AA	# AA[a]	# PP[b]	#H_2O	kcal/mol	kcal/mol	kcal/mol	s-*trans*-in.	s-*cis*-in	*s-trans*-ex	s-*cis*-ex.	δ_{pred}	
Y97	13	4	0	-2.18	-0.29	6.65	-137.5	***-138.6***	-133.7	-131.9	-138.3	**-140.1**
Y118	12	4	1	--	0.00	4.97	--	--	***-137.4***	-112.7	-137.4	**-138.0**
Y65	14	3	2	-6.32	-8.51	-2.85	-121.5	-129.7	*-135.5*	**-136.5**	-135.4	**-137.4**
Y98	14	3	1	-0.02	7.90	9.97	-120.4	*-120.2*	-120.8	-127.5	-120.4	**-136.6**
Y139	10	3	2	-9.31	-16.65	-5.28	-116.6	-115.3	*-125.2*	**-137.9**	-125.2	**-136.6**
Y137	11	4	2	-23.08	-28.25	-3.49	-114.1	-115.1	*-129.6*	**-134.1**	-129.6	**-134.0**
Y119	14	7	1*	11.26	--	-1.81	-119.4	-121.2	--	***-124.4***	-124.4	**-128.0**

2.3.3 Conclusions

This work has taken the first step to automated prediction of ^{19}F NMR in bromodomain proteins. The machinery has been built and tested to take protein crystal structures, cut down clusters based target residue and desired cluster size, and predict chemical shifts. We have shown that water plays a significant role in the prediction of ^{19}F chemical shifts, and that models must take account of water's influence on tyrosine's phenol to accurately predict chemical shifts. Further work on the benchmarking of conformational energies would greatly benefit this protocol if data were available to unequivocally assign relative configuration energetics. Currently, this method should be able to accurately predict the chemical shifts of 3-fluorotyrosines where no water directly participates in hydrogen bonds with high reliability.

2.3.4 Theoretical Methods

Hydration of Protein and Optimized H Positions. Using the MDWeb online Molecular Dynamics on Web toolset,[164] the following procedure was performed.

1) Select action "Prepare Structure Topology for AMBER ParmFF99SB* (Hornak & Simmerling, including Best & Hummer psi modification)"[165, 166]
2) Select action for structural optimization of 50 or more exterior water molecules using the Classical Molecular Interaction Potentials (CMIP)[167]
3) Select action to energetically minimize hydrogen atom positions using NAMD[168]
4) Select action to export PDB structure
5) File I/O: The resulting PDB exported from MDWeb is missing the column at the end of a regularly formatted PDB file that specifies the actual atom designation for each ATOM type. Opening the .PDB file in OpenBabel[169], and choosing to convert PDB -> PDB fixes this issue.

Cluster Generation. Once the PDB file has been properly formatted, use this file as input for the cluster generation script. Additionally one needs to specify the target residue number and the cut off radius for cluster generation.

The script will create a cluster by searching for protein residues within the cutoff radius of the target residues' non-hydrogenic atoms. Once all clusters have been found, the script keeps these residues, and caps the peptide chains with a neutral cap (either acetyl- or methylamino-group to simulate a polypeptide chain). Note: Ensure that all capping hydrogen atoms have been added prior to optimization. The sample output from the cluster generation script is included in the SI.

Optimization. The target residue is then optimized with Density Functional Theory, within a frozen cluster, i.e. only the fluorinated residue is optimized within a fixed cluster framework. The molecular clusters are optimized using the M06-L[63] density functional with the def2-SVP basis set[170] on all atoms. Gas phase computations of the ^{19}F NMR and protein structure were found to be inaccurate, and have difficulty converging with systems having charge separation, respectively. Thus a solvation method (SMD) which more accurately represents the dipolar exterior solvent was selected for further use.

^{19}F NMR Prediction. After the optimized cluster is obtained, the ^{19}F NMR is predicted. Trifluoroacetate (δ_{exp} = -76.55 ppm relative to $CFCl_3$) is used for the computation of the reference chemical shielding (σ_{ref}) for the computation of the chemical shift

$$\delta_{pred} = (\sigma_{ref} + \delta_{exp}) - \sigma_{pred} \quad (1)$$

To more accurately predict chemical shifts, a linear regression between experimental measurements and prediction protocols is common practice. The benchmark against a training set (see Table 2.3.5) of several 19F NMR prediction protocols; the protocols varied modeling parameters such as 1) gas phase or SMD implicit solvation, 2) density functional choice (B3LYP or PBE0), and 3) basis set size (double zeta or triple zeta quality).

Table 2.3.5: Reference ^{19}F NMR Data

	19F δ (ppm)
3-fluoro-tyrosine (1Water)	-137.6
2-fluoro-phenol[171]	-141.9
2,6-difluoro-phenol[172]	-139.1
2-fluoro-*p*-hydroquinone[171]	-138.7
5-fluoro-indole[173]	-126.55
6-fluoro-indole[173]	-121.83
5-fluoro-tryptophan[173]	-126.15
6-fluoro-tryptophan[173]	-122.85
fluoro-benzene	-113.15
hexafluoro-benzene	-164.9
4-fluoro-phenylalanine	-116.7
o-Penta-fluorobenzene	-139.9
m-Penta-fluorobenzene	-162.1
p-Penta-fluorobenzene	-153.5

In order to accurately reproduce the equilibrium distribution of various fluorine and phenol isomers, a Boltzmann weighting protocol was implemented to weight chemical shifts by their relative free energies.

$$\delta = \sum_{c_i} \delta_{pred}^{c_i} \left(\frac{e^{-\Delta G^{c_i}/RT}}{\sum_{c_i} e^{-\Delta G^{c_i}/RT}} \right) \qquad (2)$$

Software. All optimization, thermochemistry and σ_{orb} computations were accomplished using the Gaussian09 Rev D.01 suite of electronic structure programs.[74]

2.3.5 Acknowledgements

Authors of this work in progress are: Isley III, W. C.; Urick, A.; Pomerantz, W.C.; Cramer, C.J..WCI would like to acknowledge the University of Minnesota Doctoral Dissertation Fellowship for funding.

2.3.6 Notes and references

References have been collected at the end of the thesis.

Chapter 3

Chemical Reactivity at the Macromolecular Scale

3.1 Electrochemical Reduction of 2,4-Dinitrotoluene in Aprotic and pH-Buffered Media[†]

3.1.1 Introduction

The detection of nitroaromatic explosives, such as the widely used 2,4,6-trinitrotoluene (TNT), is a subject of much research in view of both the detection of explosive devices and environmental remediation.[174-194] Due to the extremely low equilibrium vapor pressure of TNT, many detection efforts focus on the more readily vaporizing 2,4-dinitrotoluene (DNT).[174-176] Because the latter results as a byproduct in TNT production due to incomplete nitrification of toluene, DNT is nearly always present in TNT-based explosives.[184, 195] Detection of DNT in aqueous samples is of additional importance because of its hepatocarcinogenicity.[194] The electroactive nature of the nitro substituents allows for the electrochemical detection of DNT.[196] As a result, several explosive sensing devices were presented in recent literature that rely upon electrochemical detection.[180, 186-192, 197-200] However, despite the rather large amount of published work that takes advantage of the electroactivity of DNT, a surprisingly small effort has been made in the past to elucidate the mechanism for DNT reduction.

The polarographic characteristics of DNT in *aqueous* solution were shown to be rather similar to those of nitrobenzene in that each nitro group is reduced to an *N*-hydroxylamino group in a single four-proton, four-electron reduction wave.[196, 201] This observation indicates that the cyclic voltammetry of DNT should also be very similar to that of nitrobenzene, thus providing a good starting point for proposing a mechanism for DNT reduction. Indeed, the electrochemistry of nitrobenzene has been studied quite extensively.[196, 202-206] In anhydrous acetonitrile and *N,N*-dimethylformamide, nitrobenzene is reduced electrochemically to produce a stable radical anion.[204, 205] When liquid anhydrous ammonia is used as a solvent, the radical anion accepts a second electron at a much more negative potential, producing a stable

---

[†] Adapted with permission from:

Olson, E.; **Isley III, W.C.**; Brennan, J.; Cramer, C.; Buhlmann, P. "Electrochemical Reduction of 2,4-Dinitrotoluene in Aprotic and pH-Buffered Media." *J. Phys. Chem. C*, **2015**.*119* (23), pp 13088-13097.
Link: http://dx.doi.org/1 0.1021/acs.jpcc.5b02840

dianion.[202] In the case of 1,4-dinitrobenzene, two individual one-electron transfers are observed; however, it is unclear whether the radical nitrogen is reduced or whether a diradical is formed.[207, 208] In analogy to this work on related compounds, the mechanism for the reduction of DNT shown in Figure 3.1.1 is proposed here for aprotic media.

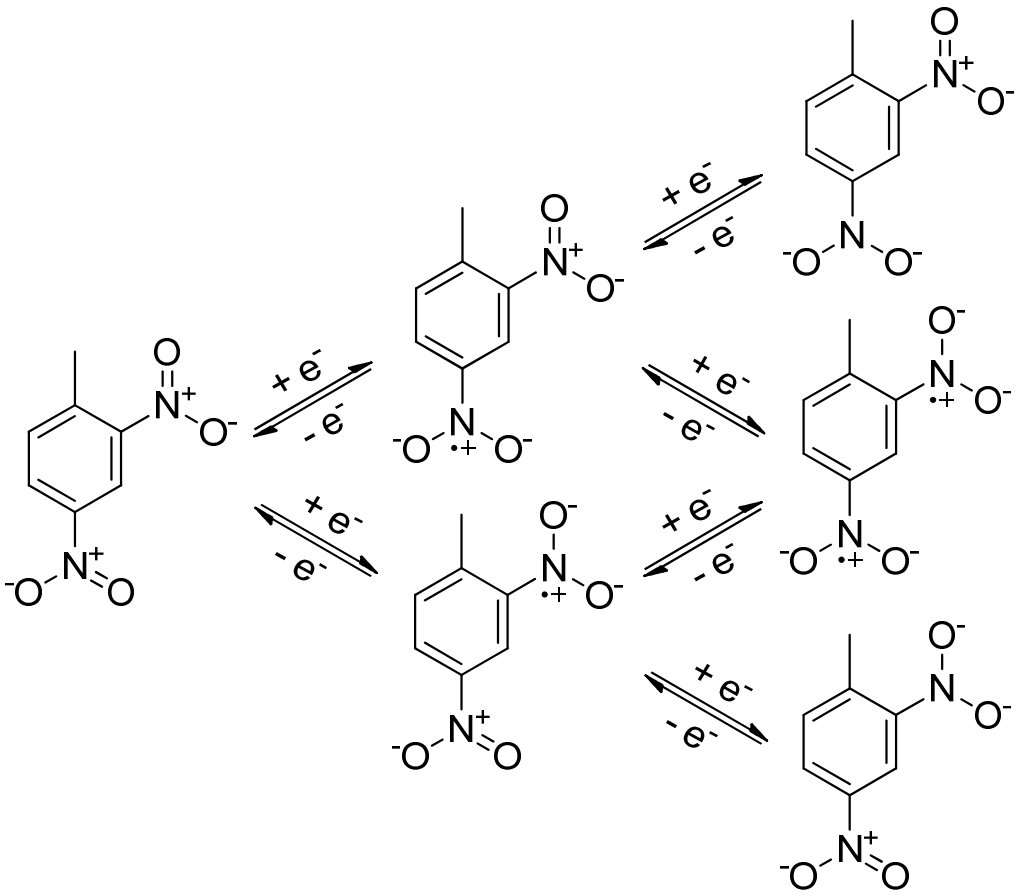

Figure 3.1.1 Proposed mechanism of DNT reduction in aprotic solutions.

The work presented herein also shows that the reduction of DNT in acetonitrile as observed by cyclic voltammetry changes significantly upon the addition of a proton source. Similarly, previously published work showed that in anhydrous *N,N*-dimethylformamide upon the addition of a proton source the polarographic reduction of nitrobenzene to a radical anion decreases in intensity and a new reduction wave occurs that is attributed to the four step, four-electron production of *N*-phenylhydroxylamine.[204] In aqueous media, the reduction of nitrobenzene proceeds directly to the formation of *N*-phenylhydroxylamine, which in acidic solutions undergoes an additional two-proton, two-electron transfer at more negative potential

to produce aniline.[202, 203, 209, 210] Recently, a computational study investigated the electrochemical mechanism and potentials of TNT reduction in aqueous solution, making reference to the literature of experimental electrochemistry of various nitroaromatic compounds.[211] While the authors showed that the nitro group in the 2 position of TNT is most easily reduced, it was not clear whether this is also true for DNT. Therefore, the more general mechanism presented in Figure 3.1.2 is proposed here for the electrochemical reduction of DNT in proton-containing media.

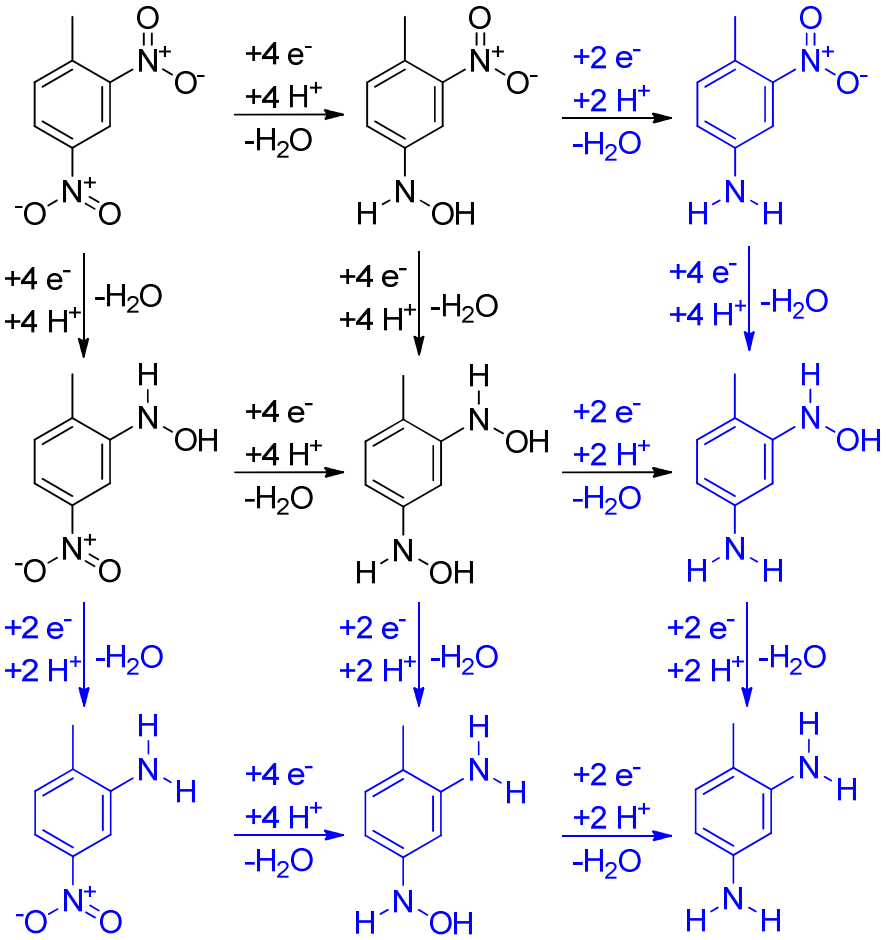

Figure 3.1.2 Possible reduction pathways to electrochemically produce 2,4-diaminotoluene from DNT in solutions with available protons.

The reduction steps in Figure 3.1.2 are representative of the polarographic characteristics previously observed for DNT in aqueous solution[196] while those in blue are representative of the complete reduction of DNT to 2,4-dinitroanailine. For electrochemical reductions such as those depicted in Figure 3.1.1 and Figure 3.1.2, it is important to note that all

chemically reasonable routes to achieve the final product are likely followed simultaneously as competing processes. The total contribution of each path is dependent upon the pH of the solution and the molecular properties of each intermediate.

In this work, we explored the electrochemical reduction mechanism of DNT in unbuffered acetonitrile and pH buffered acetonitrile. We show that DNT undergoes two well-resolved electron transfers in unbuffered acetonitrile as well as basic acetonitrile. The radical anion formed in these solutions by the reduction of DNT is sufficiently basic to deprotonate the slightly acidic DNT, giving rise to an intense blue color indicative of deprotonated DNT.[212] In acetonitrile solutions buffered with a triethylamine/triethylammonium buffer, the two reduction peaks coalesce into one irreversible reduction that is consistent with the production of 2,4-bis(*N*-hydroxylamino)toluene.

3.1.2 Results and discussion

Voltammetry with unbuffered acetonitrile To determine whether, in the absence of a proton source, DNT would produce cyclic voltammograms (CVs) consistent with the two-step, two-electron transfer depicted in Figure 3.1.1, cyclic voltammetry of DNT was performed in unbuffered anhydrous acetonitrile. Typical CVs for DNT in acetonitrile/0.1 M NBu_4ClO_4 such as those shown in Figure 3.1.3 exhibit two redox couples centered at –1.30 and –1.68 V vs. Ag/Ag^+.

At scan rates of 100 mV/s and higher, the CVs of DNT in anhydrous acetonitrile are consistent with the electron transfer mechanism depicted in Figure 3.1.1, although it is impossible to determine from this experimental data which of reduction paths shown in Figure 3.1.1 is followed. The increased separation of the cathodic and anodic peaks at higher scan rates is indicative of moderately slow electron transfer kinetics between the electrode and DNT.[213] When the working electrode was operated at a potential sufficiently negative to reduce DNT, a substance of intense blue color was observed, diffusing away from the electrode surface. This type of coloration was observed previously by Fornazini and co-workers; however, no explanation as to the source of the color was offered.[186] Subsequently, we showed in a non-electrochemical study that the blue color observed for solutions of DNT and basic compounds

in dimethyl sulfoxide arises from the deprotonation of the methyl group of DNT.[212] Because the radical anion and the subsequently formed dianion resulting from the reduction of DNT are both expected to be at least somewhat basic, it appeared likely that neutral, unreacted DNT is deprotonated by electrochemically reduced DNT diffusing away from the electrode. To test this hypothesis, a solution of 10 mM DNT with 100 mM NBu_4ClO_4 was reduced at a constant potential of –2.0 V. The product resulting from this bulk reduction was not sufficiently stable to allow for isolation and purification. However, an aliquot was removed after ten minutes and a visible absorption spectrum was measured of this sample. This resulting spectrum was then compared to the visible spectrum of an acetonitrile solution of 0.2 mM DNT and 10 mM tetrabutylammonium hydroxide (see Figure 3.1.4).

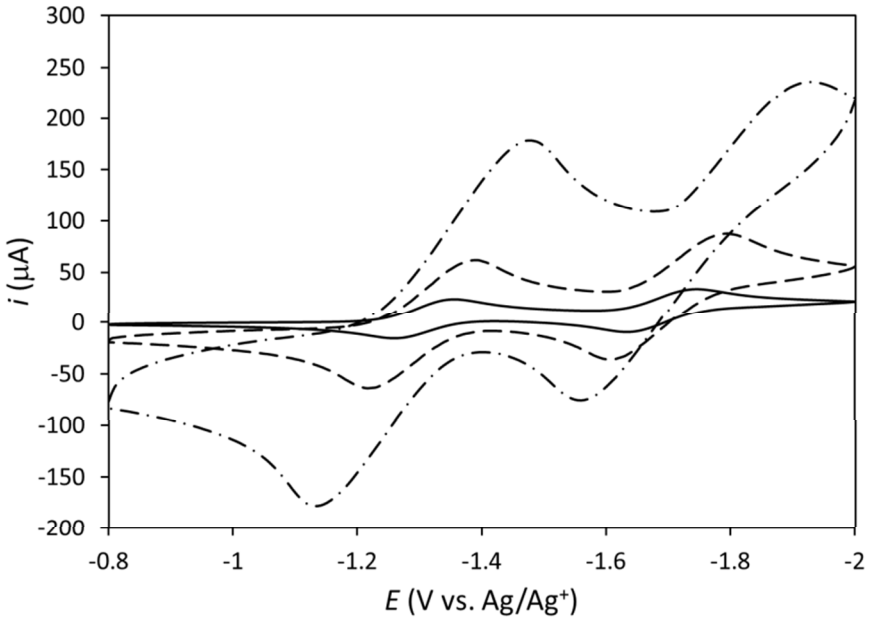

Figure 3.1.3 Cyclic voltammograms of 2.16 mM DNT in acetonitrile/100 mM NBu_4ClO_4 at scan rates of 100 (solid), 1000 (dashed), and 10,000 mV/s (dot-dashed). Working electrode: 1.6 mm diameter Au disk, reference: Ag/10 mM $AgNO_3$, auxiliary: Pt wire. T = 21 °C.

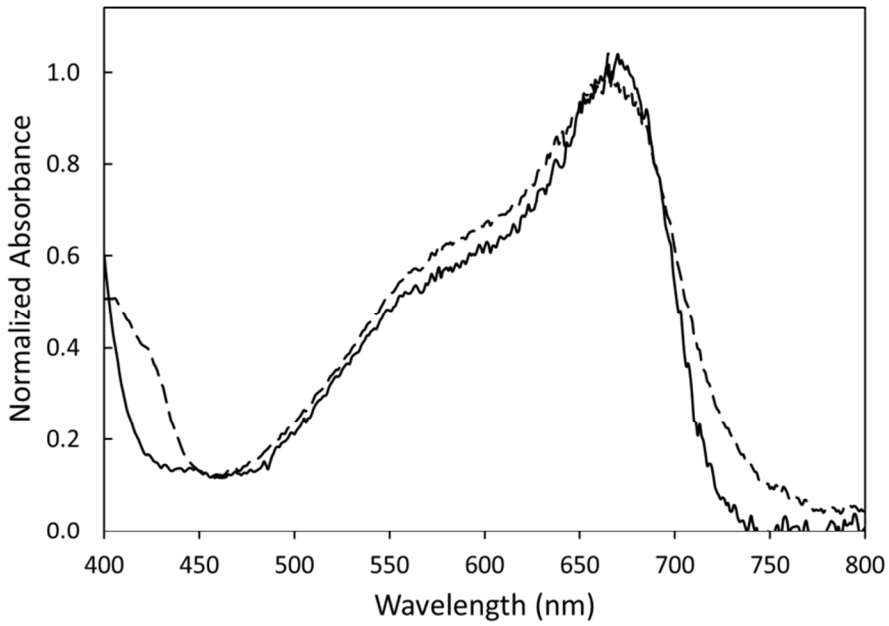

Figure 3.1.4 Visible spectrum for an aliquot removed from an electrochemical cell after bulk reduction of DNT in acetonitrile (solid) and for a solution of 0.20 mM DNT with 10 mM NBu_4OH (dashed). For clarity, absorbances are shown normalized with respect to the absorbance maxima.

The spectra strongly suggest that the blue color emanating from the working electrode is indeed the result of the deprotonation of unreacted DNT. As we show in the following section, protonation of the DNT radical anion results in further electrochemical reduction. Since unreacted DNT may serve as a proton source, the protonated form of electrochemically reduced DNT may undergo the ensuing reactions outlined in Figure 3.1.2. Because the intermediate steps of this complicated mechanism (and their reduction potentials and pK_a values) do not result in identifiable features in CVs, quantitative fitting of CVs for DNT in unbuffered acetonitrile is difficult. Therefore, the electrochemical characteristics of DNT in buffered acetonitrile solutions were considered with more detail instead.

Voltammetry with pH buffered acetonitrile solutions. Because the radical anion formed in the electrochemical reduction of DNT is capable of deprotonating DNT itself, cyclic voltammetry was performed with acetonitrile solutions of known concentrations of available H^+, (added in the form of $HClO_4$, in concentrations up to 8 mM) in order to gain a better

understanding of the electrochemistry of DNT. Since hydrogen is reduced on gold in the potential range of interest,[214] these experiments were carried out with a large excess of triethylamine (exceeding the DNT concentration hundredfold), buffering H^+ in the form of protonated triethylamine and keeping the free H^+ concentration low. Throughout these experiments, in which variable amounts of 70 wt % perchloric acid were added as a source of H^+,, an appropriate amount of water was added in addition to the water introduced with the aqueous $HClO_4$ to maintain a constant water concentration of 19 mM (which is the concentration of water in the 8 mM $HClO_4$ solution, as obtained by addition of 70 wt % perchloric acid but no additional water).. Initial experiments were performed with solutions containing 1.00 mM DNT along with 100 mM triethylamine and no added of H^+. A CV of such a solution is shown in Figure 3.1.5.

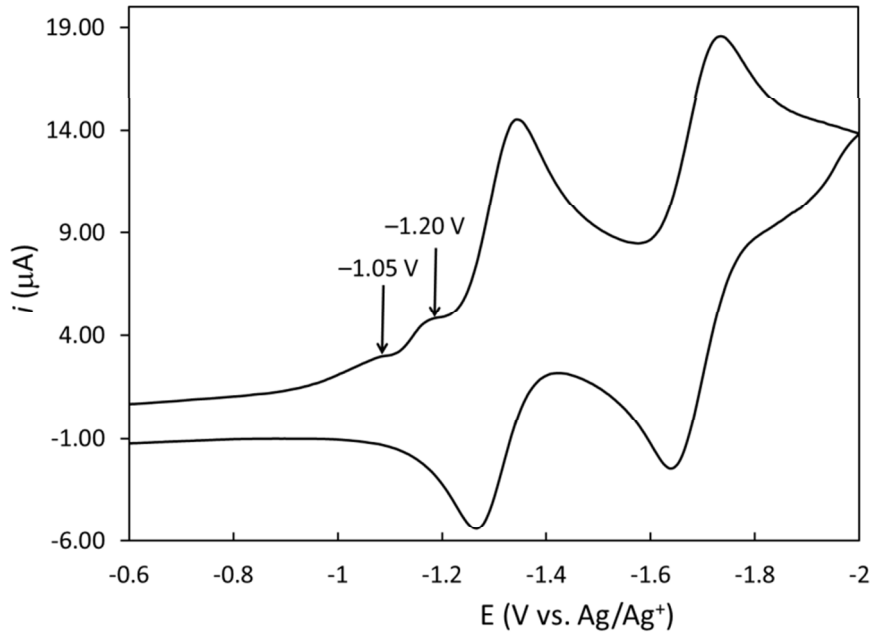

Figure 3.1.5 Cyclic voltammetry of 1.00 mM DNT in acetonitrile/100 mM NBu_4ClO_4 + 100 mM triethylamine and 19 mM water. Working electrode: 1.6 mm diameter Au disk, reference: Ag/10 mM $AgNO_3$, auxiliary: Pt wire. Scan rate = 100 mV/s, T = 21 °C.

The appearance of small reductive current maxima at –1.05 and –1.20 V are the result of a slight increase in the concentration of available protons, likely due to the acidity of the added water (see Figure 3.1.6). Aside from these two small peaks, the remainder of the CV is consistent

with the nonprotic mechanism presented in Figure 3.1.1 in that the oxidative and reductive waves in the voltammogram have similar current magnitudes. As compared to Figure 3.1.3, the potential separation of the oxidative and reductive peaks when scanning with 100 mV/s has decreased from 94 to 62 and from 114 to 80 mV for the peaks centered at –1.30 and –1.68 V, respectively. More importantly, no blue-colored products were observed during these experiments, an expected result due to the presence of water, which has a higher acidity than DNT.

Subsequent experiments were performed with increasing concentrations of $HClO_4$, a well-known strong acid in acetonitrile ($pK_a = -8.8$),[215] to determine the effect of H^+ addition to the solution and the stoichiometry of the reaction of DNT with H^+. Cyclic voltammograms of 1.00 mM DNT in 100 mM triethylamine solutions containing a varying concentration of $HClO_4$ are presented in Figure 3.1.6A. For clarity, only the first cycle of each CV is shown.

As the concentration of added H^+ and, thereby, the ratio of triethylammonium to triethylamine is increased, a sharp increase in the magnitude of the irreversible peak located at –1.05 V is observed, as shown in Figure 3.1.6B. The peaks located at –1.30 and –1.68 V slowly decrease in intensity until, at 8 equivalents of H^+, they become negligible in intensity. At concentrations of H^+ that are less than 7-fold excess to the concentration of DNT, a nearly linear relationship is observed between the concentration of available H^+ and the peak current observed at –1.05 V. No further substantial increase in peak current is observed when the concentration of available H^+ exceeds the DNT concentration more than eightfold. This indicates that the overall reduction of DNT in the presence of the pH buffer triethylammonium/triethylamine requires 8 protons to progress to completion. In order to reduce DNT to 2,4-diaminotoluene, as laid out in the scheme presented in Figure 3.1.2, a total of 12 electrons and 12 protons would be required. In fact, the only routes that utilize a total of 8 protons all stop with the production of 2,4-bis(*N*-hydroxylamino)toluene. Therefore, we conclude that, at the potentials accessible in acetonitrile and in the presence of triethylammonium/triethylamine buffers, DNT is reduced only to 2,4-bis(*N*-hydroxylamino)toluene, as it was similarly observed for DNT by polarography in aqueous solutions of neutral or alkaline pH.[196]

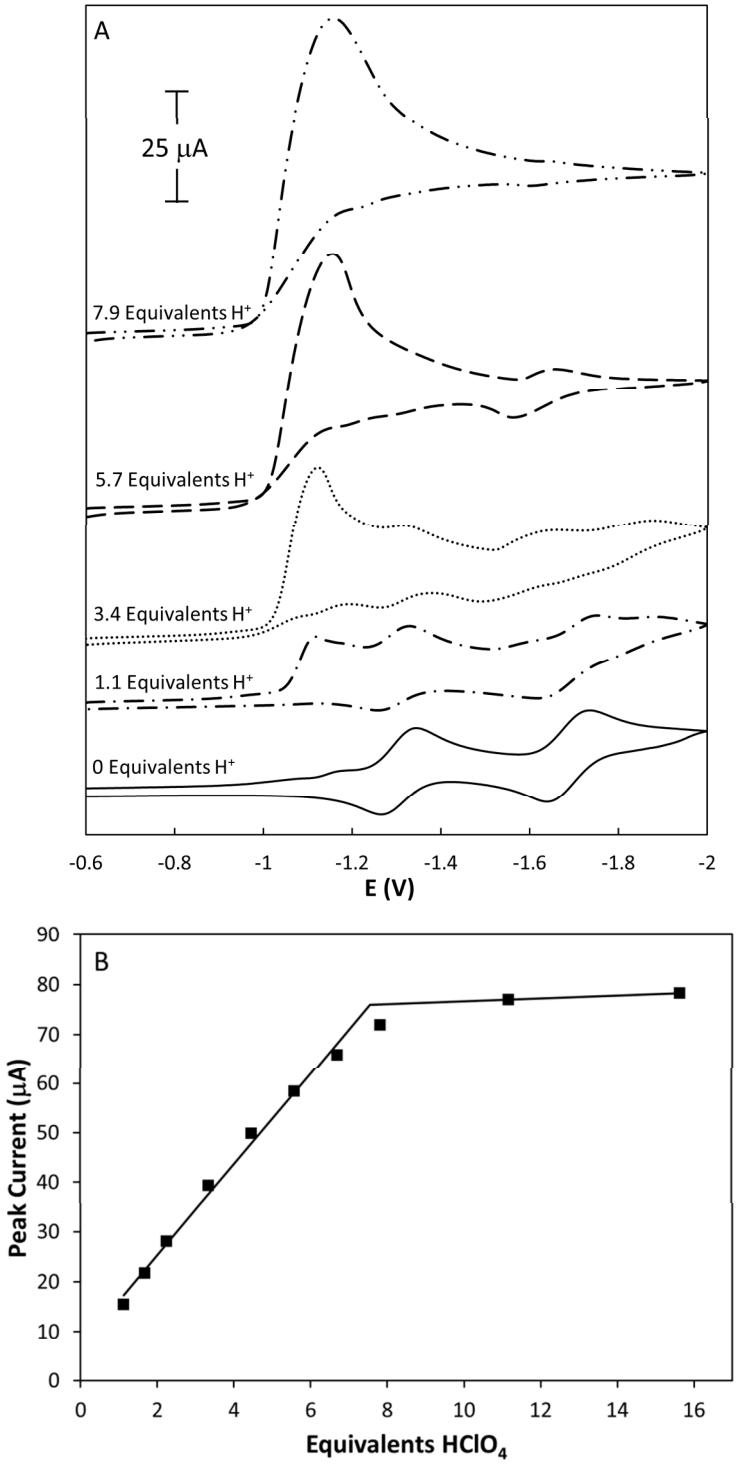

Figure 3.1.6 Cyclic voltammograms for 0–8 mM equivalents of $HClO_4$ relative to DNT (A) and plot of the peak current at –1.1 V with respect to the $HClO_4$ concentration (B) for acetonitrile solutions containing 1.00 mM DNT, 100 mM NBu_4ClO_4, and 100 mM triethylamine. Working electrode: 1.6 mm diameter Au disk, reference: Ag/10 mM $AgNO_3$; auxiliary electrode: Pt wire. Scan rate = 100 mV/s, T = 21°C.

The reduction of DNT in the presence of triethylammonium/triethylamine buffer occurs at a potential substantially less negative than is observed in aprotic conditions. This indicates that the species that is reduced is not free DNT but is rather a product of the interaction of DNT with triethylammonium, likely the DNT–triethylammonium hydrogen bond complex. A similar effect was also observed for the reduction of nitrobenzene in DMF at a dropping mercury electrode upon the introduction of a proton source.[205] Conversely, if the reduction of DNT occurred before protonation, the onset of reduction would not occur until the applied potential has reached approximately –1.25 V (the potential at which DNT reduction is first observed in the aprotic experiments). In that case, an increase in the current observed at –1.30 V would be observed rather than the formation of a new discrete peak. Such alternative pathways to the complete reduction of DNT are likely the source of several much smaller peaks observed at intermediate potentials in Figure 3.1.6 for additions of 1–6 proton equivalents.

It is important to point out that, at triethylammonium concentrations less than 8 equivalents relative to DNT, the observed CVs are characteristic of both protic and aprotic environments. This is most clearly evident in the CV measured with 1 equivalent added $HClO_4$. In this voltammogram, the peak at –1.05 V has increased substantially over that for aprotic environment while the reductions centered at –1.30 and –1.68 V are still clearly present. This may be explained as follows: upon the initial reduction of the DNT–triethylammonium complex, excess protons are rapidly consumed by the electrochemical reduction products. Because the electrochemical reduction products are localized near the electrode surface, a local pH change in the volume immediately adjacent to the electrode is observed. Once all of the triethylammonium available in this limited volume is deprotonated, the voltammogram begins to show characteristics similar to those of an unbuffered aprotic environment.

Lastly, it is interesting to note that the reduction of DNT to 2,4-bis(*N*-hydroxylamino)toluene in *aqueous* solutions takes place as two discrete reductions separated by approximately 100 mV in a polarographic experiment.[196] Moreover, the *chemical* reduction of DNT with Na_2S in aqueous solution results predominantly in the formation of 2-nitro-4-aminotoluene, supporting the conclusion that in aqueous solution the first reduction of DNT is thermodynamically more favorable than the second reduction.[216] By contrast, a single concerted

reduction peak associated with this same reduction in acetonitrile is observed. Clearly, the difference in solvation between these two environments has a substantial effect on the mechanism of DNT reduction.

Density Functional Theory Studies. In order to gain further insight into the reduction mechanism for DNT, we considered by computational means the stability of intermediate compounds formed during the reduction of DNT to 2,4-bis(hydroxylamino)toluene, 2-amino-4-nitrotoluene, and 4-amino-2-nitrotoluene. The molecular structure and geometry of each likely intermediate along the reduction pathway was optimized using the M06-2X/6-31+G(d) level of density functional theory (DFT; see Methods Section for full details). After initial optimization, improved electronic energies were calculated as single-point calculations by replacing 6-31+G(d) with 6-311+G(2df,p) for all atoms. For greatest relevance to environmental conditions, the solvation effects of water were considered using the SMD continuum solvation model.[217]

To evaluate the different reaction pathways, the energies of a total of 103 structures were computed. The presentation of these results in a clear manner that readily permits the reader to distinguish between important reaction pathways and energetically unfavourable side reactions is not a trivial task. Neither tables nor conventional schematics labelled with numerical ΔG values are suitable for this purpose. To better visualize the computed energetics of the reduction of DNT, we are representing in Figure 3.1.7 and Figure 3.1.8 the reduction paths in an energy landscape, with the ΔG of each step of the reaction represented on the vertical axis. As a reference point, the energy level of DNT has been represented in each figure as a horizontal yellow line. Energetically favorable reactions are represented by a downward shift while unfavorable reactions are represented by an upward shift. To improve the readability of these graphs further, electron transfer, protonation, and dehydration reactions are represented by dashed, dotted, and dot-dashed lines, respectively, connecting the energy levels of the respective reactants and products. For greatest relevance to environmental conditions, the apparent ΔG at pH 7 is plotted, where $\Delta G_{pH=7} = \Delta G^0 - RT \ln[H^+]$. Moreover, for each step the functional group that reacts next is highlighted in color. Arrows on the right hand side of panels A to C point towards further reactions of intermediates on subsequent panels.

These computational results reveal a multitude of pathways that exhibit similar thermodynamics. The most favorable pathways for the ortho and para reaction routes are highlighted in bold. While this pathway is not the most favorable route *overall*, each step was considered individually when determining the most likely product of the electrochemistry of DNT. It is important to note that once the electrode potential is sufficient to cause initial reduction, all subsequent electron transfer reactions of equal or lesser potential also become thermodynamically favorable. This pathway, which begins with the reduction of the para nitro group, eventually proceeds to the formation of 2,4-bis(hydroxylamino)toluene, an eight electron, eight proton net reaction. This finding is consistent with the titration results shown in Figure 3.1.6B, where the reductive current reaches a maximum upon addition of approximately an eight-fold excess of protons relative to the DNT concentration.

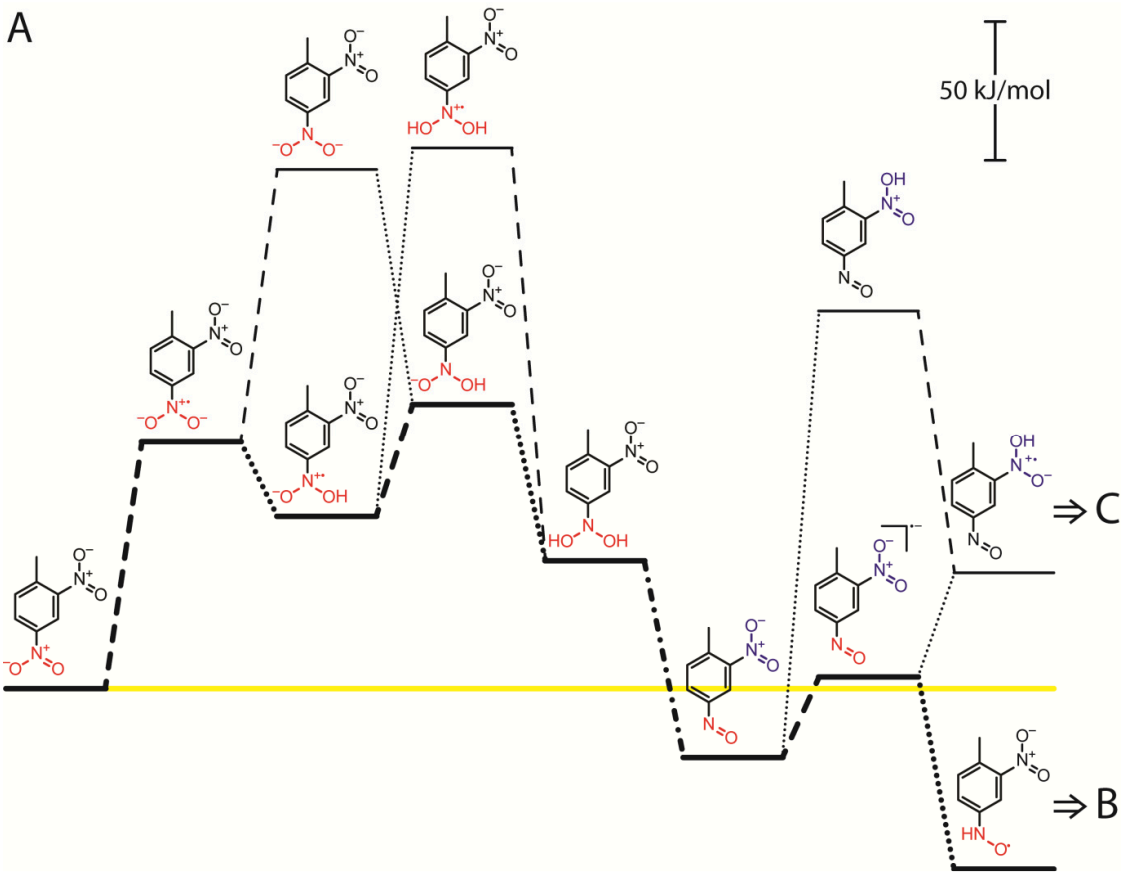

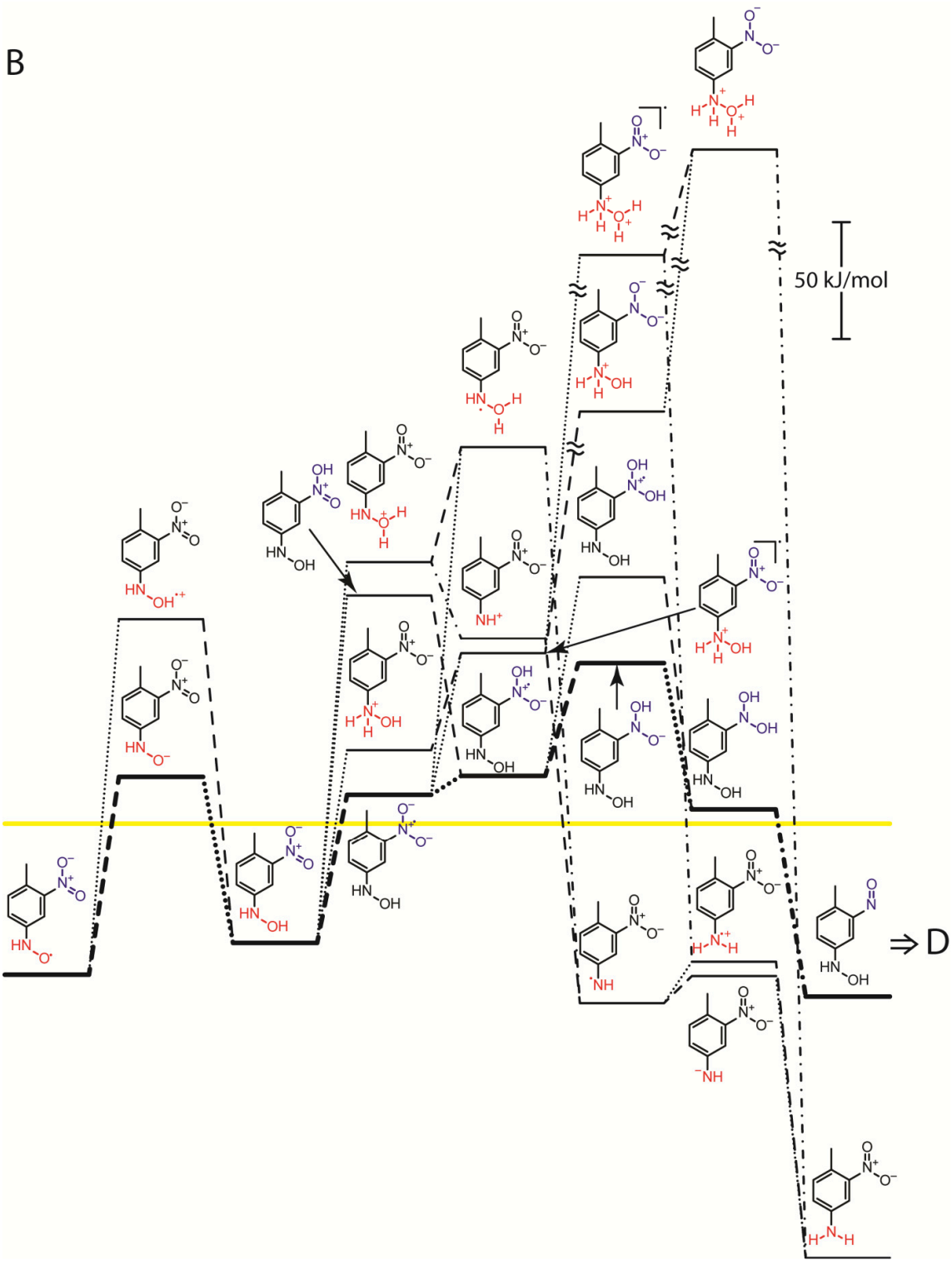
B
50 kJ/mol
⇒ D

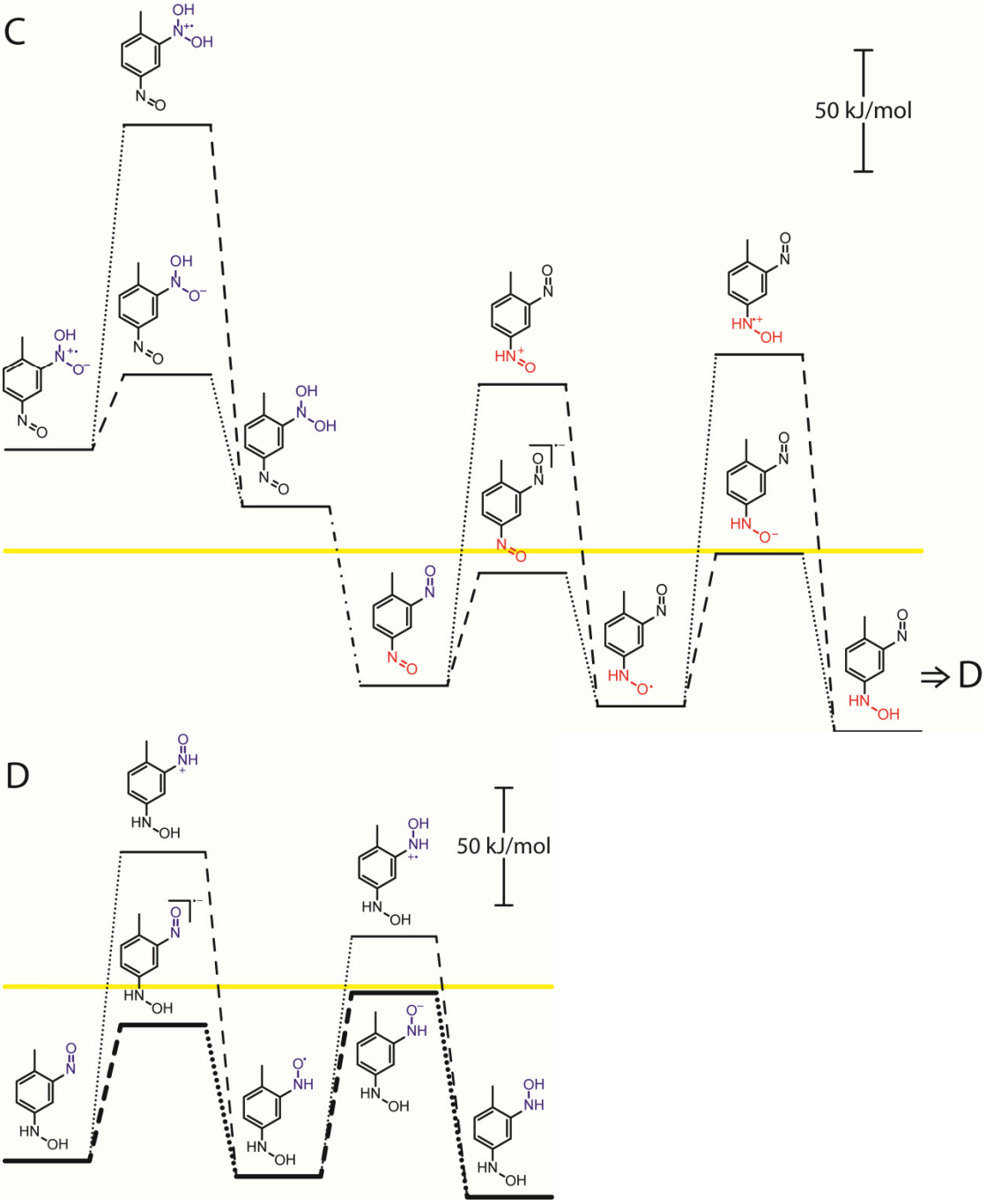

Figure 3.1.7 Reduction pathways for DNT proceeding initially through the para nitro group. Electron transfers are indicated by dashed, proton transfers by dotted, and dehydration reactions by dot-dashed lines. The functional group reacting next is highlighted for each step in color.

Briefly, the energetics of the most favourable pathway suggest the transfer of two electrons and two protons to the para nitro group (Figure 3.1.7A) according to an ECEC mechanism (where the transfer of the second electron is energetically more favourable than the first one), followed by dehydration to give a nitroso group. The latter is still very reactive and reacts with another two electrons and two protons according to another ECEC mechanism (where the transfer of both electrons is energetically more favourable than the transfer of the first electron to the para nitro group) to give a hydroxylamino group in the third column of Figure 3.1.7B. This is followed by another two sets of analogous ECEC transfer reactions at the ortho nitro group, giving toluene with two hydroxylamino substituents as the final product.

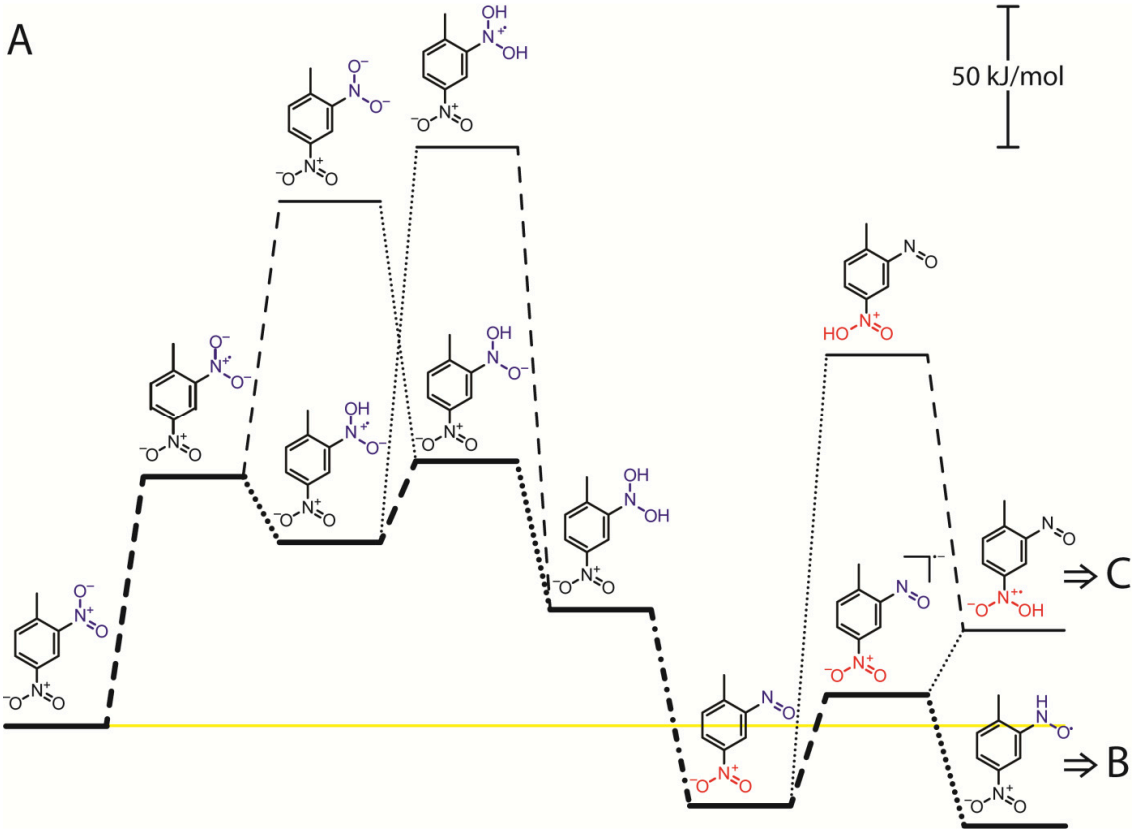

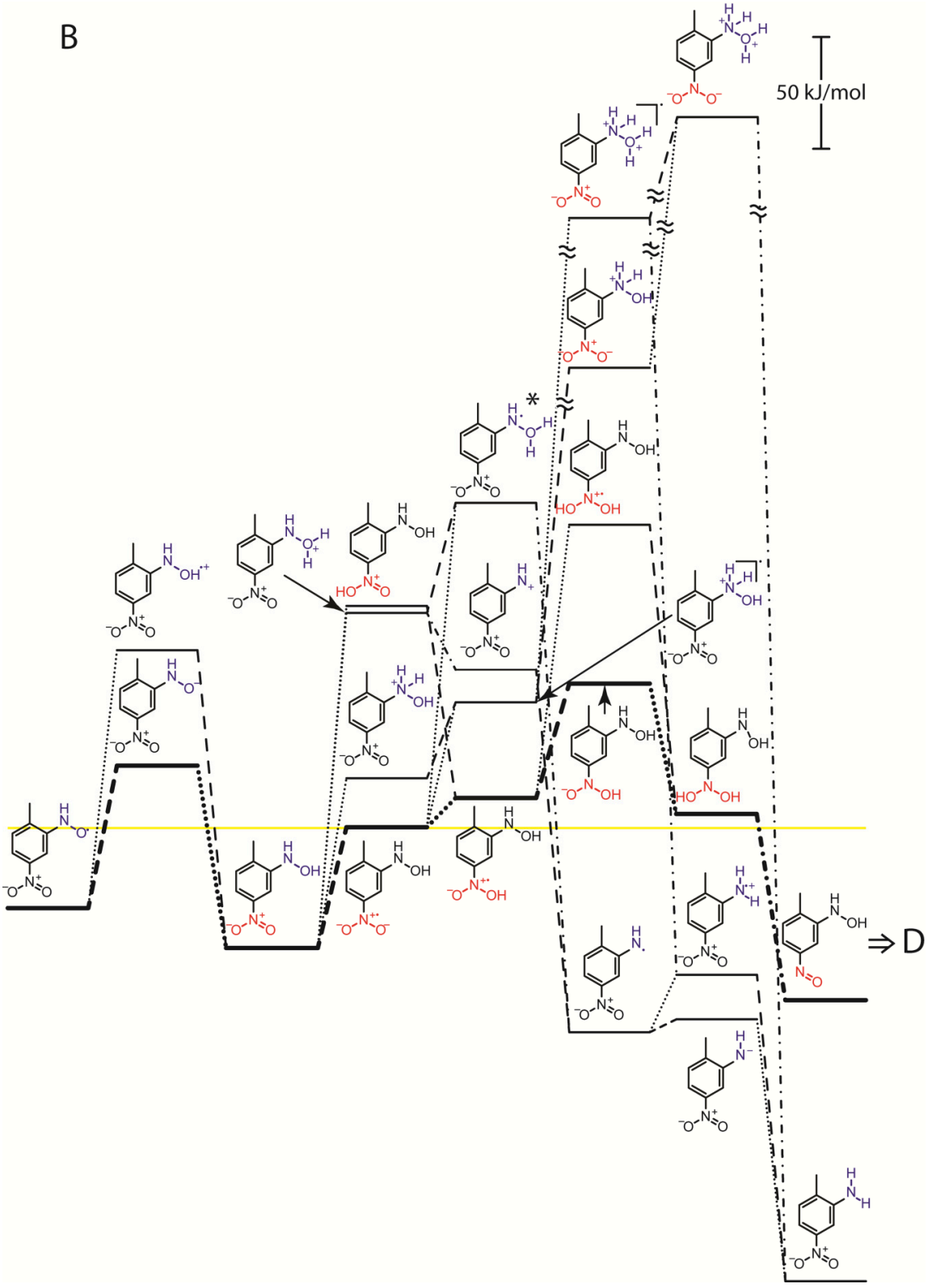
B
50 kJ/mol
⇒ D

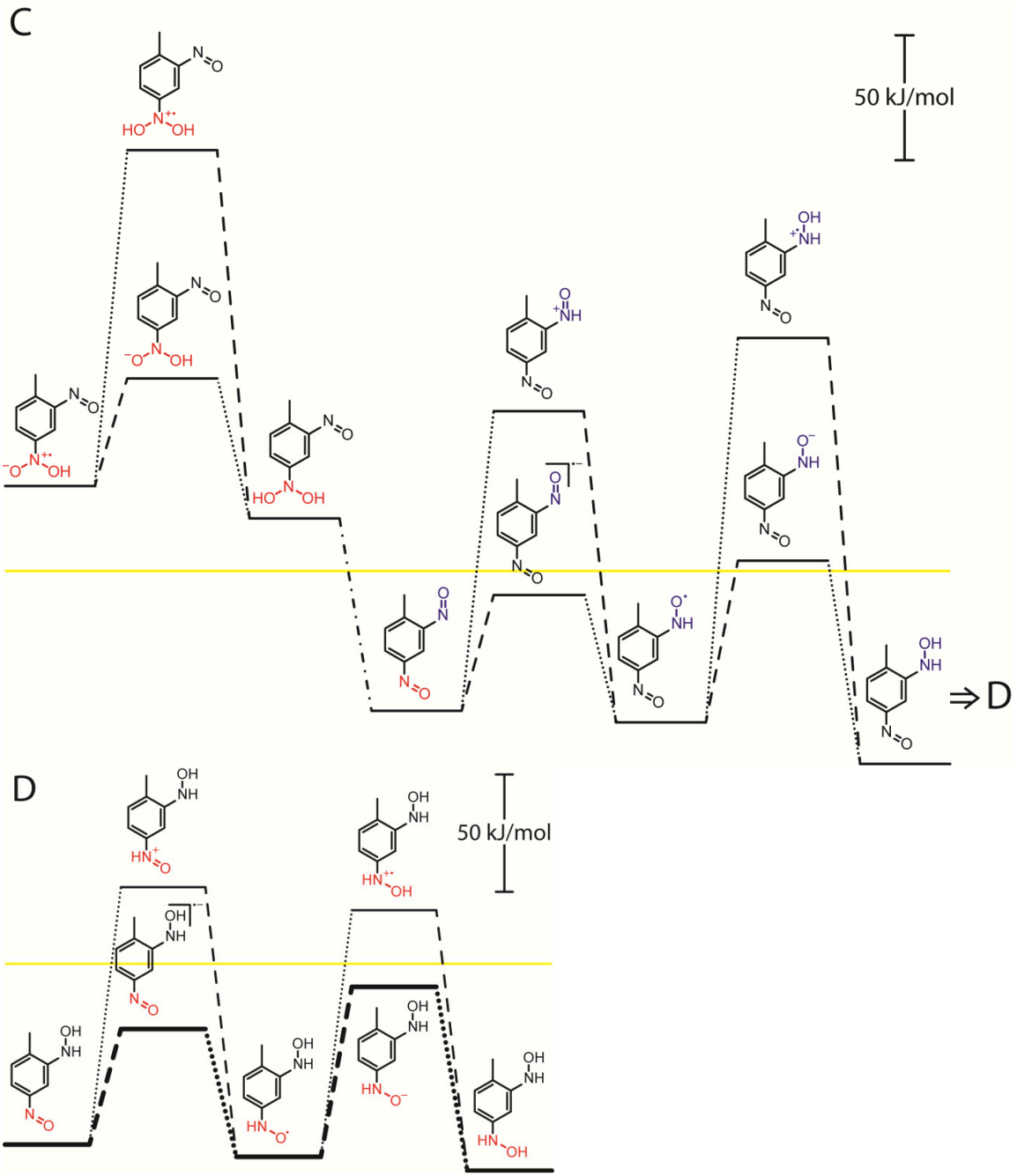

Figure 3.1.8 Reduction pathways for DNT proceeding initially through the ortho nitro group. Electron transfers are indicated by dashed, proton transfers by dotted, and dehydration reactions by dot-dashed lines. The functional group reacting next is highlighted for each step in color. Note that the structure in panel B marked with * dissociated upon geometric optimization, and that its energy level used here is an approximation taken from the energy of the analogous compound in Figure 3.1.7.

The alternative pathway starting with an ECEC reduction of the ortho nitro group of DNT and resulting first in the ortho nitroso compound is energetically very similar to the corresponding steps of the para pathway. The thermodynamic similarity suggests that the two routes provide nearly identical contributions to the overall reduction pathway of DNT. Some doubt is cast on this conclusion by results from a computational discussion of solvation effects on the reduction of DNT and the experimental observation that the reduction of DNT with bisulfide in an aqueous medium gives 4-amino-2-nitrotoluene and 2-amino-4-nitrotoluene in a ratio 12:88.[216] It was argued that thermodynamics alone cannot explain the regioselectivity observed in the reduction of the two nitro groups of DNT.[216] While this may be true, it should be noted that the kinetic bottleneck explaining the ratio of the observed ratio of 4-amino-2-nitrotoluene and 2-amino-4-nitrotoluene could also be much further down the para and ortho pathways in the reduction of the two different *N*-hydroxylamino-nitrotoluene isomers. Indeed, consistent with the shorter timescale of voltammetry as opposed to the chemical reaction, the voltammetric observation in this study of a 8 e^-, 8 H^+ reduction of DNT in acetonitrile to form 2,4-bis(*N*-hydroxylamino)toluene rather than the formation of amino groups suggests that the reduction of *N*-hydroxylamino groups to amino groups is a comparatively slow reaction. This would also be consistent with unidentified peaks detected by HPLC for the chemical reduction of some substituted dinitrobenzenes, which were speculated to be hydroxylamine or nitroso intermediates.

It is important that, among all eight electron transfers for both the para and the ortho pathways, the first electron insertion into the nitro group is the least energetically favorable transfer for the entire reduction pathway. As a result, upon reaching an electrode potential sufficient to reduce DNT, all of the subsequent reductions to the bis(hydroxylamino) become energetically favorable. Moreover, at pH = 7, all of the protonation steps are thermodynamically favorable with the exception of panel B of both Figure 3.1.7 and Figure 3.1.8, columns 4 to 5; the pK_a of this reaction is calculated to be 5.7, resulting in approximately 5% of the species in column 4 being protonated at equilibrium. This protonated species is then available for further reduction. Since protonation is expected to be kinetically facile, this step does not represent a significant bottleneck to the overall reduction of DNT to bis(hydroxylamino)toluene.

Secondly, the pathways to produce aminonitrotoluene in Figs 7B and 8B must also be considered. While the formation of aminonitrotoluene is the more favorable overall pathway, the protonation reaction moving from column 4 to column 5 is extremely unfavorable (pK_a = –2.9 and –3.6 for the ortho- and para- pathway, respectively). As a result, at pH = 7 an extremely small fraction ($\approx 10^{-8}$ %) will be protonated at equilibrium, severely limiting the efficiency of this pathway.

Lastly, the reduction pathway to produce 2,4-diaminotoluene from 2,4-bis(*N*-hydroxylamino)toluene was also considered by DFT simulation. Figure 3.1.9 shows part of this pathway, i.e., the reduction of 2,4-bis(*N*-hydroxylamino)toluene to produce 4-amino-2-hydroxylamino-toluene. For the alternative path to 2-amino-4-hydroxylaminotoluene and the subsequent paths to 2,4-diaminotoluene, see the Supporting Information. Figure 3.1.9 illustrates that the initial reduction of a hydroxylamino to an amino group is predicted on the basis of thermodynamics to occur quite readily. As similarly mentioned above in the discussion of the (lack of) amino-4-nitrotoluene formation, the absence of 2,4-diaminotoluene formation may again be either related to solvation effects or slow kinetics. The last column of Figure 3.1.9 also indicates that the continuation of this pathway from 2-amino-4-hydroxylaminotoluene to 2,4-diaminotoluene is unexpected due to the extremely unfavorable thermodynamics of both the reduction and protonation of 2-amino-4-hydroxylaminotoluene.

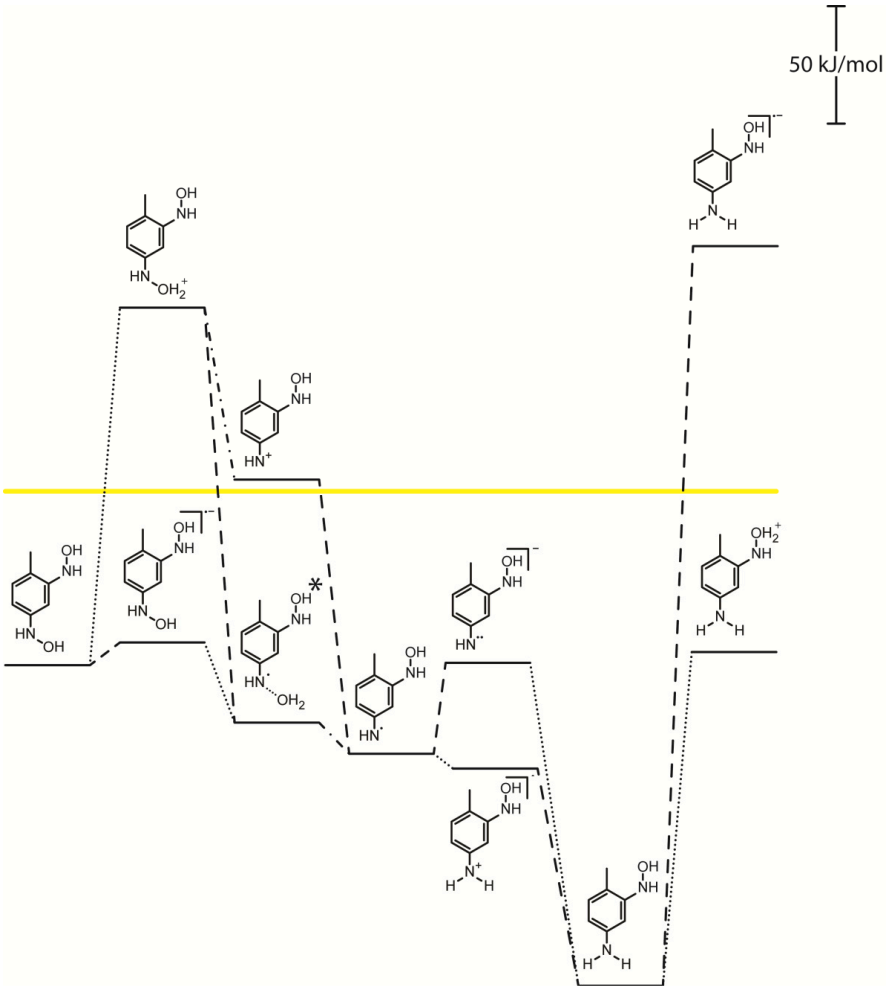

Figure 3.1.9 Reduction pathway to produce 4-amino-2-hydroxylamino-toluene from 2,4-bis(*N*-hydroxylamino)toluene. Electron transfers are indicated by dashed, proton transfers by dotted, and dehydration reactions by dot-dashed lines. Note that the structure marked with * dissociated upon geometric optimization and has been arbitrarily placed.

3.1.3 Conclusions.

In this work, we have shown that, in anhydrous acetonitrile, 2,4-dinitrotoluene undergoes two individual one-electron transfers that are readily resolved by cyclic voltammetry. The product of the electrochemical DNT reduction is capable of deprotonating a second uncharged DNT molecule, producing the blue color indicative of deprotonated DNT. After abstracting a proton from DNT, the protonated species then undergoes further reduction, making quantitative mechanistic interpretation of the cyclic voltammograms difficult. Upon addition of triethylammonium/triethylamine as a pH buffer to the acetonitrile solution, the two reduction waves gradually decrease in intensity while one large reduction wave at a less negative

potential than the waves associated with formation of the radical anion begins to form. This new reduction wave increases in intensity with the addition of additional protons until a triethylammonium concentration 8 times the concentration of DNT is present in the solution. This concentration of triethylammonium is consistent with the 8 e^-, 8 H^+ reduction of DNT to form 2,4-bis(*N*-hydroxylamino)toluene. To further understand the observed electrochemical properties of DNT, DFT simulations were performed. Their result further support the formation of 2,4-bis(hydroxylamino)toluene in the presence of a proton source.

Furthering the understanding the reduction mechanism of DNT will assist in the development and implementation of electrochemical sensors for DNT. For example, taking advantage of the 8-electron transfer for DNT reduction in solutions containing a source of readily available protons will improve the sensitivity of electrochemical DNT sensors. Moreover, a better understanding of the reduction mechanism and products of the reduction process may provide further insight into the decomposition of DNT under environmental conditions. Such insight should prove highly beneficial in assisting attempts to better understand and optimize the remediation of DNT-contaminated soils.[218]

3.1.4 Methods

Experimental Methods Caution: Extreme care must be taken with organic solutions of tetrabutylammonium perchlorate and perchloric acid as these solutions may explode when heated or evaporated to dryness. All reagents were used as received without further purification unless otherwise noted. Anhydrous acetonitrile, electrochemical grade tetrabutylammonium perchlorate (NBu_4ClO_4), and 2,4-dinitrotoluene (97%) were obtained from Sigma-Aldrich (St. Louis, MO). pH-buffered acetonitrile solutions were prepared by adding appropriate amounts of reagent grade 70% $HClO_4$ from Fisher Scientific (Pittsburgh, PA) to a solution of 100 mM triethylamine (Sigma-Aldrich) in anhydrous acetonitrile/100 mM NBu_4ClO_4. $HClO_4$ was titrated prior to solution preparation to determine the analytical concentration of the acid. Using this determined concentration, an appropriate amount of water was added to all solutions to maintain a constant water concentration throughout the course of the experiment. Cyclic voltammetry experiments with acetonitrile were carried out with a CHI600C Potentiostat (CH

Instruments, Austin, TX). All electrochemical experiments were carried out using a three-electrode setup with a 1.6 mm-diameter Au disk (BAS, West Lafayette, IN) working electrode, a 0.25 mm Pt wire coil (99.998 %, Alfa Aesar, Ward Hill, MA) auxiliary electrode, and either a Ag/AgCl/saturated KCl reference electrode (BAS) for aqueous experiments or a Ag/(10 mM $AgNO_3$ + 100 mM NBu_4ClO_4) reference electrode (BAS) for acetonitrile experiments. The Au working electrode was polished on Microcloth polishing pads using 5.0 μm Micropolish II deagglomerated alumina, both from Buehler (Lake Bluff, IL). After polishing, the electrode was rinsed thoroughly with deionized water and then ethanol, followed by drying under a stream of Ar. Prior to measurements, all voltammetry solutions were purged with high purity argon for 15 minutes while stirring vigorously to remove oxygen. UV–Vis spectra were measured with an Agilent 8453 UV–Vis spectrometer. All potentials referenced herein are with respect to Ag/10 mM Ag^+ for acetonitrile solutions.

Computational Methods

Optimization and Thermochemistry Geometry optimizations were performed for all species at the M06-2X[63] level of density functional theory. The 6-31+G(d) basis was used for C, N, O, and H atoms during optimization. The nature of stationary points was assessed in all cases by computation of analytic vibrational frequencies, which were also used to compute the molecular partition functions necessary to predict 298 K thermochemical quantities using the conventional ideal-gas, rigid-rotator, quantum-mechanical quasi-harmonic-oscillator[137] approximation.[219] Improved electronic energies were computed as single-point calculations by replacing 6-31+G(d) with 6-311+G(2df,p) for all atoms.

Solvation and standard reduction potentials. The effects of aqueous solvation were included during optimization using the SMD continuum solvation model.[217] A 1 M standard state was used for all species in aqueous solution except for water, which has a 55.6 M standard state concentration. For all molecules, excluding water, the free energy in aqueous solution is computed as the sum of the 1 atm gas-phase free energy, the standard state concentration adjustment to 1 M (equivalent to $RT\ln[24.5]$), and the 1 M to 1 M solvation free energy computed by the SMD model. For water, the 1 atm gas-phase free energy is added to the standard state concentration change (1 atm to 55.6 M), and the experimental 1 M to 1 M

solvation free energy (-6.3 kcal mol^{-1}). The gas phase free energy of a proton is taken to be 0.00999 a.u. The standard state concentration of 1 M is used for protons (pH = 0). The 1 M to 1 M solvation free energy of the proton was taken from experiment as -265.9 kcal mol^{-1}.[220-223]

Standard reduction potentials were calculated to assess the likelihood of accessing various intermediate oxidation states. For a general redox reaction,

$$\mathrm{O}_{(aq)} + \mathrm{n}\, e^-_{(g)} \rightarrow \mathrm{R}_{(aq)}$$

where O and R denote the oxidized and reduced states of a redox reaction, respectively, and n is the number of electrons involved in the redox reaction, the reduction potential $E^0_{\mathrm{O|R}}$ relative to the standard hydrogen electrode (SHE) was computed as

$$E^0_{\mathrm{O|R}} = -\frac{\Delta G^0_{\mathrm{O|R}} - \Delta G^0_{\mathrm{SHE}}}{\mathrm{n}F}$$

where $\Delta G^0_{O|R}$ is the free energy associated with the redox couple above, and $\Delta G^0_{\mathrm{SHE}}$ is the free energy change for the SHE which is -4.28 eV.[222, 224] For a general acid dissociation reaction,

$$\mathrm{HA}_{(aq)} \rightarrow \mathrm{H}^+_{(aq)} + \mathrm{A}^-_{(aq)}$$

where $\mathrm{HA}_{(aq)}$ and $\mathrm{A}^-_{(aq)}$ respectively denote the acid and conjugate base, the acid dissociation constant can be written as

$$\mathrm{p}K_a = \frac{-\Delta G_a}{2.303\, RT}$$

where ΔG_a is the free energy change for the acid dissociation reaction, R is the gas constant, and T is temperature (298.15 K at standard state).

Software All optimization and thermochemistry computations were accomplished using the Gaussian09 Rev C.01 suite of electronic structure programs.[225]

3.1.5 Notes and References

References have been collected at the end of the thesis.

Acknowledgments

This work was supported by the National Science Foundation (EXP-SA 0730437 and CHE-1361595). The authors thank R. Lee Penn for measurement time on the UV–Vis spectrometer and thankfully acknowledge a Kenneth E. And Marion S. Owens Endowed

Fellowship through the Department of Chemistry and a Doctoral Dissertation Fellowship from the University of Minnesota to W.C.I.

Supporting Information

The alternative path to 2-amino-4-hydroxylaminotoluene and the subsequent paths to 2,4-diaminotoluene comparable to Figure 3.1.9 along with reaction schemes corresponding to Figure 3.1.7, Figure 3.1.8, and Figure 3.1.9 are available in the Supporting Information. This material is available free of charge via the Internet at http://pubs.acs.org.

3.2 Decomposing Chemical Warfare Agents Utilizing Metal–Organic Frameworks[†]

3.2.1 Introduction

MOFs constitute a remarkably broad, and very rapidly growing, class of crystalline materials; at their simplest, they constitute uniformly arrayed metal-containing nodes separated by organic linkers.[26] Their exceptional surface areas as well as high porosity, their amenability to modular design and construction, and their ability to present high concentrations of metal ions (or clusters) dispersed in structurally well-defined matrices make MOFs singularly attractive as solid sorbents and heterogeneous catalysts.[25] In this regard, we, and others, have demonstrated that the nodes of selected MOFs can catalytically hydrolyze phosphate ester-containing compounds,[35] a key step in the degradation of many chemical warfare agents. For example, using the well-known twelve-connected Zr_6-based MOF UiO-66, we were able to catalytically hydrolyze the nerve agent simulant dimethyl 4-nitrophenyl phosphate (DMNP, see Figure 3.2.2a).[37] Given their known outstanding thermal,[226] mechanical,[227] and hydrolytic stability,[228] MOFs containing Zr_6 nodes and multi-topic carboxylated linkers are among the most promising classes of potentially catalytic materials for deployment in personal chemical protection. Further motivating our earlier selection of UiO-66 was its presentation of multiple Zr–OH–Zr moieties—potential mimics of the Lewis-acidic Zn–OH–Zn active site found in G-agent destroying enzymes such as phosphotriesterase. (Given the small pore aperture present in UiO-66 the catalysis is accomplished mainly at the surface of the MOF and presumably at defect sites, *i.e.*, missing-linker sites on the nodes.) Despite the success of these initial studies, to date MOFs have exhibited unacceptably slow kinetics for capture and destruction of nerve agents and their simulants.[35]

[†] Adapted with permission from:
Mondloch, Joe; Katz, Michael J.; Isley III, W. C.; Gosh, Pritha; Liao, Peilin; Bury, Wojciech; Wagner, George W.; Hall, Morgan G.; DeCoste, Jared B.; Peterson, Gregory W.; Snurr, Randall Q.; Cramer, Christopher J.; Hupp, Joseph T.; Farha, Omar K. *Nature Materials.* **2015**, 14, pp 512-516.
Link: http://dx.doi.org/10.1038/NMAT4238

A key issue in exploiting MOFs for the hydrolysis of chemical warfare agents has been that their pore apertures have been too small to admit agents to the interior spaces where the vast majority of potential active sites are located. In other words, nearly all of the sorptive capacity and resultant hydrolysis activity was restricted to sites on the exterior of the MOF crystallites. A related issue, specifically with UiO-66, is that the most desirable reaction sites are already occupied by linkers. To overcome these challenges we turned our attention towards the recently reported Zr_6-based MOF NU-1000 (Figure 3.2.1).[229] NU-1000 is built up from *eight* (rather than twelve) connected $Zr_6(\mu_3\text{-}O)_4(\mu_3\text{-}OH)_4(H_2O)_4(OH)_4$ nodes and tetratopic 1,3,6,8(*p*-benzoate)pyrene linkers ($TBAPy^{4-}$).[230] The resulting structure directs a total of four terminal-zirconium ligated aquo and hydroxo groups per node into exceptionally wide (31 Å) channels, and an additional four into smaller 10 Å channels (versus zero for defect-free UiO-66). The ultra-wide channels allow bulky phosphate-ester molecules to permeate the entire framework, including the vast MOF interior. Here we demonstrate that NU-1000 is highly active for the destruction of the nerve agent simulant DMNP and more importantly the highly toxic chemical warfare agent GD (*O*-pinacolyl methylphosphonofluoridate, also known as Soman).

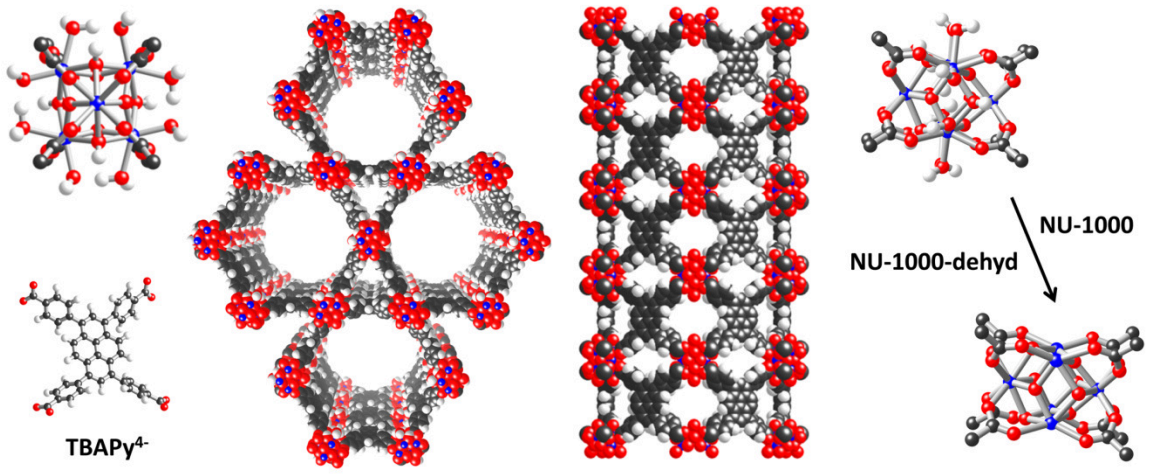

Figure 3.2.1: Molecular representations of the NU-1000 node and linker (left), MOF topology (two views, center), and its dehydrated node (NU-1000-dehyd, right). Color code: Zr (blue); O (red); C (black); H (white).

3.2.2 Results and Discussion

To probe the efficacy of NU-1000 for the catalytic destruction of phosphate ester bonds we first investigated the simulant DMNP. Nerve agent simulants are an essential tool and precautionary measure for assessing phosphate ester decomposition in nearly all laboratories given the highly toxic nature of chemical warfare agents. Simulants (such as DMNP) also allow rigorous physical characterization as well as mechanistic investigations of key catalytic systems that can help drive the development of superior decontamination catalysts. Catalytic hydrolysis of DMNP was carried out using NU-1000 in an aqueous *N*-ethylmorpholine buffered solution at pH 10 (Figure 3.2.2a). Hydrolysis of the phosphorous nitrophenyl bond was observed by ^{31}P NMR (Figure S3). The kinetics of the hydrolysis reaction were followed by monitoring the formation of *p*-nitrophenoxide via visible-region absorption spectroscopy (λ_{max} = 407 nm); see the example in Figure 3.2.2b. It is notable that the *p*-nitrophenoxide anion forms exclusively at pH 10. We observed 77% conversion over the course of 60 min (Figure 3.2.2c, red circles) while the measured half-life, *i.e.*, 50% conversion, was found to be 15 min. This corresponds to an initial turnover frequency (TOF) of 0.06 s^{-1} assuming the entire framework is accessible to DMNP (additional details regarding the calculation of TOFs are reported in the Supporting Information). The observed half-life represents the fastest known decomposition of a phosphate ester nerve agent simulant by a MOF to date, *vide infra*. Notably the background reaction is negligible over the same time course (3% conversion after 60 min; see Figure 3.2.2c, black diamonds). Finally NU-1000 is completely recyclable for the hydrolysis of DMNP over three runs (Figure S6).

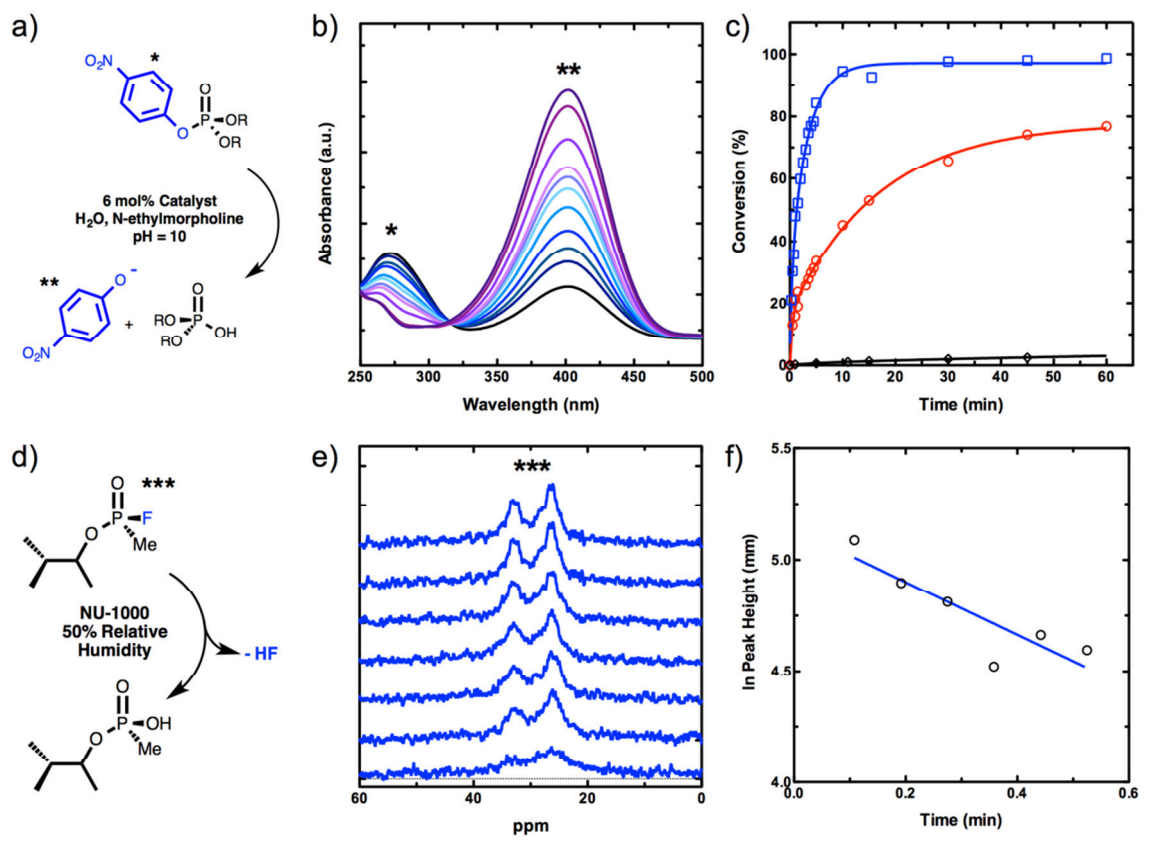

Figure 3.2.2: Hydrolysis data and reactions for DMNP and GD. (a) Reaction conditions for the catalytic decomposition of DMNP using NU-1000, (b) UV-Vis monitoring of the formation of *para*-nitrophenoxide, (c) percent conversion to para-nitrophenoxide vs. time for the background reaction (black diamonds), NU-1000 (red circles), and NU-1000-dehyd (blue squares), (d) reaction conditions for the decomposition of GD, (e) ^{31}P NMR spectra of GD, and (f) loss of GD vs time monitored via ^{31}P NMR.

To establish that the observed catalysis is indeed heterogeneous, we filtered NU-1000 from the reaction mixture and resumed monitoring to formation of the *p*-nitrophenoxide anion. No further conversion was observed (Figure S4). Powder X-ray diffraction (PXRD) measurements showed that NU-1000 remains crystalline after service as a catalyst (Figure S5). We also investigated a soluble, molecular, zirconium-based cluster, $Zr_6(O)_4(OH)_4(BzA)_{12}$;[231] over the course of 60 min the hydrolysis reaction goes only toward 20% completion, Figure S7. Clearly, soluble homogeneous Zr_6-based clusters are not as potent as the corresponding site-isolated, eight-connected clusters within the highly porous NU-1000 scaffold. As an additional control, we examined $Zr(OH)_4$ which has been shown to be effective for the destruction of

phosphate-based nerve agents.[232] Under our experimental conditions, the hydrolysis of DMNP by $Zr(OH)_4$ is negligible (Figure S8). Overall, our results demonstrate the heterogeneous nature of NU-1000, as well as the advantages of presenting Zr_6-based clusters within a highly porous network for the catalytic hydrolysis of phosphoester bonds.

To gain insight into the potential mechanism(s) of DMNP hydrolysis in NU-1000 we turned to quantum chemical calculations based on density functional theory (DFT). We found two classes of favorable binding modes for DMNP at the $Zr_6(\mu_3\text{-}O)_4(\mu_3\text{-}OH)_4(H_2O)_4(OH)_4$ node of NU-1000. In the first, DMNP forms hydrogen bonds with the node-ligated water and hydroxide moieties. An example is shown in Figure 3.2.3a, with a full list of investigated binding modes given in Table S1. The lowest-energy configuration has a binding free energy (ΔG°_{assoc}) of -26 kJ mol^{-1} and in addition to hydrogen bonding is stabilized by π-π stacking interactions between the phenyl ring of DMNP and the benzene ring of the $TBAPy^{4-}$ linkers from NU-1000 (not shown for clarity in Figure 3.2.3). The π-π stacking interactions occur at 3.1 Å which is near the optimal distance for π-π association.[233]

Next we removed a terminal water molecule from the node of NU-1000 to simulate ligand dissociation followed by DMNP substrate binding (Tables S2 and S3). Here DMNP was able to directly interact with Lewis-acidic Zr^{IV} sites in the Zr_6 cluster of NU-1000. The electrostatic interaction between the P=O moiety of DMNP and Zr takes precedence, while the π-π stacking interactions between the linker and DMNP are no longer present. This most stable DMNP–Zr^{IV} coordinated configuration is 22 kJ mol^{-1} uphill in free energy relative to the separated agent and NU-1000; its geometry includes hydrogen bonding interactions between an $-OCH_3$ of DMNP and a μ_3-O of the NU-1000 node. The strong propensity for catalysis is driven by the stability of the hydrolyzed product which is 48 kJ mol^{-1} downhill in free energy, again relative to separated reactants (Table S5). Remarkably our simulations are very similar to those calculated for the interaction and hydrolysis of DMNP by the active site of the phosphotriesterase enzyme.[38] In the enzyme, hydrolysis (from a bound Zn^{2+} center) is approximately 52.9 kJ mol^{-1} downhill. In addition, the optimized Zn–O=P distances are 2.24 Å and 1.50 Å, while the Zr–O=P distances in our simulations are 2.22 Å and 1.49 Å respectively.[234]

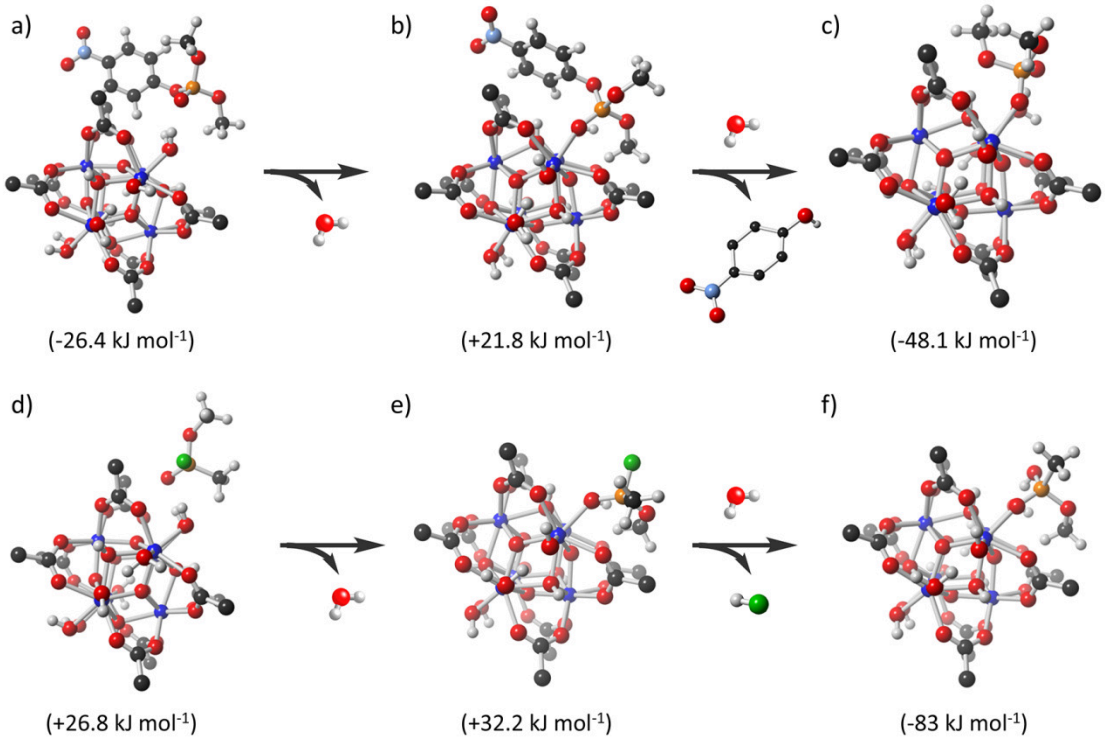

Figure 3.2.3: Key ΔG°_{assoc} (a and d) and ΔG°_{rxn} (b, c, e and f) values for the interaction of DMNP and GD analog with the node of NU-1000. (a) DMNP binding, (b) DMNP replacing a H_2O molecule, (c) hydrolysis of DMNP, (d) GD analog binding, (e) GD analog replacing a H_2O molecule, (f) hydrolysis of GD. Color code: Zr (blue); O (red); C (black); H (white); P (orange); N (light blue); F (green); S (yellow).

To experimentally probe the Lewis-acid activation pathway, we thermally treated NU-1000 at 300 °C to remove terminal aquo and hydroxo ligands and convert bridging hydroxos to oxos (NU-1000-dehyd, Figure 3.2.1). It is well known in metal-oxide chemistry that thermal treatment removes coordinating H_2O molecules as well as anionic hydroxide ligands (through condensation) to leave behind coordinatively unsaturated metal sites.[232] PXRD, diffuse reflectance infrared Fourier transform spectroscopy (DRIFTS) and thermogravimetric analysis (TGA) are all consistent with NU-1000-dehyd having the molecular formula $Zr_6(\mu_3\text{–}O)_8(TBAPy)_2$ (Figures S9–S12). Structurally, upon dehydration four of the six Zr^{IV} ions are six-coordinate, coordinatively unsaturated, Lewis-acidic ions (Figure 3.2.1, NU-1000-dehyd). Thus, two-thirds of the metal ions within NU-1000 platform are potentially available and

functional as catalyst active sites, versus only a tiny percentage for either UiO-66 or nanoparticulate $Zr(OH)_4$. Under identical reaction conditions to those for NU-1000, NU-1000-dehyd is remarkably active for the hydrolysis of DMNP, yielding a half-life of only 1.5 min and exhibiting 100% conversion after approximately 10 minutes (Figure 3.2.2c, blue squares). This in turn yields an initial TOF of 0.11 s^{-1} for the hydrolysis of DMNP by NU-1000-dehyd. We find that the node does not re-hydrate to its original configuration over the time course of simulant hydrolysis. Additional experiments indicate activity similar to that observed for NU-1000 are obtained when NU-1000-dehyd is exposed for two weeks or four months to ambient laboratory atmosphere (Figure S12). Like the parent material, NU-1000-dehyd functions heterogeneously and remains crystalline after use as a catalyst (Figures S16 and S17). Clearly opening up Zr^{IV} sites substantially enhances the hydrolysis of DMNP, data that is consistent with a mechanism involving P=O binding at these sites as well as with the rate retardation that is predicted from theory for displacement of water from the hydrated node. These results are also supportive of our global hypothesis that selected MOFs may function as solid-state mimics of the well-known phosphotriesterase enzyme that utilizes a pair of Lewis-acidic sites.

Because MOFs are crystallographically defined, we were able to carry out predictive simulations regarding the interactions of the simulant DMNP with the node of NU-1000. We also analyzed computationally the binding of analogs of the chemical warfare agents GD and *O*-ethyl S-[2-ethyl] methylphosphonothioate (VX). In contrast to the simulations for DMNP, the hydrogen-bonding interactions that were present are not thermodynamically favorable for the GD and VX analogs (*e.g.*, Figure 3.2.3d, additional information is given in Table S6). We also find that the interactions of the P=O moieties of the GD and VX analogs directly with the Zr^{IV} ions are uphill in free energy by 32 and 22 kJ mol^{-1}, respectively. However, upon coordinative binding, there are sizable driving forces for hydrolysis of the GD and VX analogs. Our simulations suggest selective hydrolysis of the P–F bond of GD is 83 kJ mol^{-1} downhill, while hydrolysis of the P–S bond of VX is 123 kJ mol^{-1} downhill and is predicted to be favored over hydrolysis of P–O at 79 kJ mol^{-1} downhill (additional information is provided in the online Supporting Information).

Inspired by the catalysis results for DMNP, as well as the favorable thermodynamics uncovered computationally, we decided to see if NU-1000 could catalyze the hydrolysis of the chemical warfare agent GD. (***Caution! Experiments should be run by trained personnel using appropriate safety procedures only.***) To start we utilized ^{31}P NMR to investigate the decomposition of GD with NU-1000 in an *N*-ethylmorpholine buffered solution under conditions similar to those utilized for DMNP (Figure 3.2.2 d-f). Remarkably the observed half-life was found to be just 3 min, while the initial TOF was 0.013 s^{-1}. The ^{31}P NMR spectra are dominated by the presence of the product, pinacolyl methylphosphate (PMPA) near 25 ppm, while the twin resonances for the GD isomers (near 31 and 38 ppm) are strongly depleted by the time we measure the initial data point. We also measured the decomposition of GD under 50% relative humidity utilizing ^{31}P SS-NMR; the P–F coupled resonances at 26 and 34 ppm disappear (Figure S19).[232] Under these conditions NU-1000 yields a reaction half-life of 36 min (Figure S19), nearly 80-fold more active than the best MOF to date for the destruction of GD and comparable to the best existing solid-state materials for chemical threat protection (Table 1, *vide infra*).[35, 232] It is also worth noting that typically hundreds of milligrams of metal oxide are needed to observe similar decomposition rates for GD while only thirty milligrams of NU-1000 was needed.[232]

Table 3.2.1: Comparison of Phosphate Ester Degradation by MOFs

MOF	Substrate [a]	$t_{1/2}$ (min)	Ref
Simulants			
NU-1000-dehyd	DMNP	1.5	This Work
NU-1000	DMNP	15	This Work
UiO-66	DMNP	45	[37]
MIL-101(Cr)-DAAP [b]	DENP	300	[235]
$\{[Ho_4(dpdo)_8(H_2O)_{16}BiW_{12}O_{40}](H_2O)_2\}^{7+}$	BNPP	295,000	[236]
Chemical Warfare Agents			
NU-1000	GD	36	This Work
HKUST-1	GD	2880	[237]

[a] Dimethyl 4-nitrophenyl phosphate (DMNP); diethyl 4-nitrophenyl phosphate (DENP); Bis(4-nitrophenyl) phosphate (BNPP); [b]dialkylaminopyridine (DAAP)

3.2.3 Conclusion

In Table 3.2.1 (top), we have benchmarked NU-1000 and NU-1000-dehyd vs. other known MOFs that catalytically degrade phosphoester-containing compounds. NU-1000 and NU-1000-dehyd represent the fastest known phosphoester-containing hydrolysis catalysts to date: 3-fold and 30-fold faster than found in our previous work with UiO-66,[37] and 20-fold and 200-fold faster than the well-known Cr-MIL-101 that contains coordinatively unsaturated Cr^{III} ions linked by benzene dicarboxylates.[235] NU-1000 is also the fastest known MOF-based catalyst for the hydrolysis of GD (Table 1, bottom): 80-fold faster than the MOF HKUST-1 (under similar conditions and 960-fold faster in our buffered solution) which contains Cu^{II} paddlewheel based nodes and trimesic acid linkers.[237] Finally, NU-1000 is among the most active solid heterogeneous catalysts known for the hydrolysis of GD.[232] Our experimental and computational results suggest that the extraordinary activity of NU-1000 and NU-1000-dehyd is engendered by the unique eight-connected $Zr_6(\mu_3\text{-}O)_4(\mu_3\text{-}OH)_4(H_2O)_4(OH)_4$ node and weak intermolecular interactions (p-stacking for DMNP, more general attractive van der Waals interactions between linker and alkyl groups in GD or its analog) that direct orientations

between the substrate and catalyst-linker components along with mesoporous channels that allow substrates access to highly Lewis-acidic Zr^{IV} sites. Given these exciting results, coupled with a) the highly modular nature of these unique solids and b) the ability to computationally select and experimentally install other metals and other potential substrate recognition sites, we anticipate further progress in using MOFs for the hydrolytic degradation of other chemical warfare agents (*e.g.,* VX) and their simulants and for the destruction of toxic industrial chemicals, which are potential improvised chemical threats.

3.2.4 Acknowledgments

O.K.F, R.Q.S. and J.T.H. gratefully acknowledge DTRA for financial support (grant HDTRA-1-10-0023). C.J.C. gratefully acknowledges funding from the U.S. DOE, Office of Basic Energy Sciences, Division of Chemical Sciences, Geosciences and Biosciences (Award DE-FG02-12ER16362). R.Q.S. acknowledges the National Energy Research Scientific Computing Center (NERSC) for computational resources. J.B.D. and G.W.P. gratefully acknowledge Joint Science and Technology Office for Chemical Biological Defense (JSTO–CBD) for funding (Project Number BA13PHM210).

J.E.M., M.J.K., J.T.H. and O.K.F. developed the concept. J.E.M., M.J.K., K.Z., and W.B. carried out the materials synthesis, characterization, and catalysis with the simulant DMNP under the supervision of O.K.F. and J.T.H.; P.G. and P.L. carried out DFT simulations with DMNP under the supervision of R.Q.S.; W.C.I. carried out DFT simulations with GD and VX under the supervision of C.J.C.; G.W.W. and M.G.H. carried out GD NMR degradation experiments under the guidance of J.B.D. and G.W.P.; J.E.M., M.J.K., J.T.H., and O.K.F. wrote the manuscript first draft and the rest of the authors contributed to the editing.

3.2.5 Notes and References

References have been collected at the end of the thesis.

Supplementary Information is available in the online version of this paper.
http://dx.doi.org/10.1038/NMAT4238

References

1. Cramer, C. J., *Essentials of Computational Chemistry: Theories and Models*, John Wiley & Sons, Chichester, 2004.

2. Moon, S. and Patchkovskii, S., *First-Principles Calculations of Paramagnetic NMR Shifts*, Wiley-VCH2004.

3. Kervern, G., Pintacuda, G., Zhang, Y., Oldfield, E., Roukoss, C., Kuntz, E., Herdtweck, E., Basset, J. M., Cadars, S., Lesage, A., Coperet, C. and Emsley, L., "Solid-state NMR of a paramagnetic DIAD-FeII catalyst: sensitivity, resolution enhancement, and structure-based assignments," *J. Am. Chem. Soc.*, **2006**, (128), 13545-13552.

4. Mao, J., Zhang, Y. and Oldfield, E., "Nuclear magnetic resonance shifts in paramagnetic metalloporphyrins and metalloproteins," *J. Am. Chem. Soc.*, **2002**, (124), 13911-13920.

5. Kruck, M., Sauer, D. C., Enders, M., Wadepohl, H. and Gade, L. H., "Bis(2-pyridylimino)isoindolato iron(II) and cobalt(II) complexes: structural chemistry and paramagnetic NMR spectroscopy," *Dalton Trans.*, **2011**, (40), 10406-10415.

6. Rastrelli, F. and Bagno, A., "Predicting the NMR spectra of paramagnetic molecules by DFT: application to organic free radicals and transition-metal complexes," *Chem. Eur. J.*, **2009**, (15), 7990-8004.

7. Zhang, Y., Sun, H. and Oldfield, E., "Solid-state NMR fermi contact and dipolar shifts in organometallic complexes and metalloporphyrins," *J. Am. Chem. Soc.*, **2005**, (127), 3652-3653.

8. Marenich, A. V., Cramer, C. J. and Truhlar, D. G., "Universal solvation model based on solute electron density and on a continuum model of the solvent defined by the bulk dielectric constant and atomic surface tensions," *J. Phys. Chem. B*, **2009**, (113), 6378-6396.

9. Swart, M., "Accurate Spin-State Energies for Iron Complexes," *J. Chem. Theory Comput.*, **2008**, (4), 2057-2066.

10. Neese, F., "Efficient and accurate approximations to the molecular spin-orbit coupling operator and their use in molecular g-tensor calculations," *J. Chem. Phys.*, **2005**, (122), 34107.

11. Kurland, R. J. and McGarvey, B. R., "Isotropic NMR shifts in transition metal complexes: The calculation of the fermi contact and pseudocontact terms," *J. Magn. Reson.*, **1970**, (2), 286-301.

12. Hrobarik, P., Reviakine, R., Arbuznikov, A. V., Malkina, O. L., Malkin, V. G., Kohler, F. H. and Kaupp, M., "Density functional calculations of NMR shielding tensors for paramagnetic systems with arbitrary spin multiplicity: validation on 3d metallocenes," *J. Chem. Phys.*, **2007**, (126), 024107.

13. Pennanen, T. O. and Vaara, J., "Nuclear Magnetic Resonance Chemical Shift in an Arbitrary Electronic Spin State," *Phys. Rev. Lett.*, **2008**, (100), 133002.

14. Neese, F., "Calculation of the zero-field splitting tensor on the basis of hybrid density functional and Hartree-Fock theory," *J. Chem. Phys.*, **2007**, (127), 164112.

15. Kubica, A., Kowalewski, J., Kruk, D. and Odelius, M., "Zero-field splitting in nickel(II) complexes: a comparison of DFT and multi-configurational wavefunction calculations," *J. Chem. Phys.*, **2013**, (138), 064304.

16. Duboc, C., Ganyushin, D., Sivalingam, K., Collomb, M. N. and Neese, F., "Systematic theoretical study of the zero-field splitting in coordination complexes of Mn(III). Density functional theory versus multireference wave function approaches," *J. Phys. Chem. A*, **2010**, (114), 10750-10758.

17. Mueller, U., Schubert, M., Teich, F., Puetter, H., Schierle-Arndt, K. and Pastre, J., "Metal-organic frameworks-prospective industrial applications," *J. Mat. Chem.*, **2006**, (16), 626-636.

18. Davis, M. E. and Lobo, R. F., "Zeolite and molecular sieve synthesis," *Chem. Mat.*, **1992**, (4), 756-768.

19. Nikolakis, V., Xomeritakis, G., Abibi, A., Dickson, M., Tsapatsis, M. and Vlachos, D. G., "Growth of a faujasite-type zeolite membrane and its application in the separation of saturated/unsaturated hydrocarbon mixtures," *J. Memb. Sci.*, **2001**, (184), 209-219.

20. Tanaka, K., Yoshikawa, R., Ying, C., Kita, H. and Okamoto, K.-i., "Application of zeolite membranes to esterification reactions," *Catalysis Today*, **2001**, (67), 121-125.

21. Montalvo, S., Guerrero, L., Borja, R., Sánchez, E., Milán, Z., Cortés, I. and Angeles de la la Rubia, M., "Application of natural zeolites in anaerobic digestion processes: A review," *Applied Clay Science*, **2012**, (58), 125-133.

22. Kesraoui-Ouki, S., Cheeseman, C. R. and Perry, R., "Natural zeolite utilisation in pollution control: A review of applications to metals' effluents," *J. Chem. Tech. Biotech.*, **1994**, (59), 121-126.

23. Duren, T., Bae, Y.-S. and Snurr, R. Q., "Using molecular simulation to characterise metal-organic frameworks for adsorption applications," *Chem. Soc. Rev.*, **2009**, (38), 1237-1247.

24. Li, J.-R., Kuppler, R. J. and Zhou, H.-C., "Selective gas adsorption and separation in metal-organic frameworks," *Chem. Soc. Rev.*, **2009**, (38), 1477-1504.

25. Lee, J., Farha, O. K., Roberts, J., Scheidt, K. A., Nguyen, S. T. and Hupp, J. T., "Metal–organic framework materials as catalysts," *Chem. Soc. Rev.*, **2009**, (38), 1450.

26. Furukawa, H., Cordova, K. E., O'Keeffe, M. and Yaghi, O. M., "The chemistry and applications of metal-organic frameworks," *Science*, **2013**, (341), 1230444-1230444.

27. Mal, P., Schultz, D., Beyeh, K., Rissanen, K. and Nitschke, J. R., "An unlockable-relockable iron cage by subcomponent self-assembly," *Angew. Chem. Int. Ed.*, **2008**, (47), 8297-8301.

28. Breiner, B., Clegg, J. K. and Nitschke, J. R., "Reactivity modulation in container molecules," *Chem. Sci.*, **2011**, (2), 51.

29. Jenuwein, T. and Allis, C. D., "Translating the Histone Code," *Science*, **2001**, (293), 1074-1080.

30. Belkina, A. C. and Denis, G. V., "BET domain co-regulators in obesity, inflammation and cancer," *Nat Rev Cancer*, **2012**, (12), 465-477.

31. Lee, K., Isley, W. C., Dzubak, A. L., Verma, P., Stoneburner, S. J., Lin, L.-C., Howe, J. D., Bloch, E. D., Reed, D. A., Hudson, M. R., Brown, C. M., Long, J. R., Neaton, J. B., Smit, B., Cramer, C. J., Truhlar, D. G. and Gagliardi, L., "Design of a Metal–Organic Framework with Enhanced Back Bonding for Separation of N2 and CH4," *J. Am. Chem. Soc.*, **2013**, (136), 698-704.

32. Isley III, W. C., Zarra, S., Carlson, R. K., Bilbeisi, R. A., Ronson, T. K., Nitschke, J. R., Gagliardi, L. and Cramer, C. J., "Predicting paramagnetic 1H NMR chemical shifts and state-energy separations in spin-crossover host-guest systems," *Phys. Chem. Chem. Phys.*, **2014**, (16), 10620-10628.

33. Olson, E. J., Isley, W. C., Brennan, J. E., Cramer, C. J. and Bühlmann, P., "Electrochemical Reduction of 2,4-Dinitrotoluene in Aprotic and pH-Buffered Media," *J. Phys. Chem. C*, **2015**, (119), 13088-13097.

34. López-Maya, E., Montoro, C., Rodríguez-Albelo, L. M., Aznar Cervantes, S. D., Lozano-Pérez, A. A., Cenís, J. L., Barea, E. and Navarro, J. A. R., "Textile/Metal–Organic-Framework Composites as Self-Detoxifying Filters for Chemical-Warfare Agents," *Angew. Chem., Int. Ed.*, **2015**, (54), 6790-6794.

35. Decoste, J. B. and Peterson, G. W., "Metal–Organic Frameworks for Air Purification of Toxic Chemicals," *Chem Rev*, **2014**, (114), 5695-5727.

36. Mondloch, J. E., Katz, M. J., Isley Iii, W. C., Ghosh, P., Liao, P., Bury, W., Wagner, G. W., Hall, M. G., DeCoste, J. B., Peterson, G. W., Snurr, R. Q., Cramer, C. J., Hupp, J. T. and Farha, O. K., "Destruction of chemical warfare agents using metal–organic frameworks," *Nat Mater*, **2015**, (14), 512-516.

37. Katz, M. J., Mondloch, J. E., Totten, R. K., Park, J. K., Nguyen, S. T., Farha, O. K. and Hupp, J. T., "Simple and Compelling Biomimetic Metal-Organic Framework Catalyst for the Degradation of Nerve Agent Simulants," *Angew. Chem., Int. Ed.*, **2013**, (53), 497-501.

38. Chen, S.-L., Feng, W.-H. and Himo, F., "Theoretical Study of the Phosphotriesterase Reaction Mechanism," *J. Phys. Chem. B*, **2007**, (111), 1253-1255.

39. Moon, S.-Y., Liu, Y., Hupp, J. T. and Farha, O. K., "Instantaneous Hydrolysis of Nerve-Agent Simulants with a Six-Connected Zirconium-Based Metal–Organic Framework," *Angew. Chem., Int. Ed.*, **2015**, (54), 6795-6799.

40. Katz, M. J., Moon, S.-Y., Mondloch, J. E., Beyzavi, M. H., Stephenson, C. J., Hupp, J. T. and Farha, O. K., "Exploiting parameter space in MOFs: a 20-fold enhancement of phosphate-ester hydrolysis with UiO-66-NH2," *Chem. Sci.*, **2015**, (6), 2286-2291.

41. Moon, S.-Y., Wagner, G. W., Mondloch, J. E., Peterson, G. W., Decoste, J. B., Hupp, J. T. and Farha, O. K., "Effective, Facile, and Selective Hydrolysis of the Chemical Warfare Agent VX Using Zr6-Based MOFs," *Unpublished*, **2015**.

42. Allen, A. D. and Senoff, C. V., "Nitrogenopentammineruthenium(II) complexes," *Chem. Comm. (London)*, **1965**, 621-622.

43. Fryzuk, M. D. and Johnson, S. A., "The continuing story of dinitrogen activation," *Coord. Chem. Rev.*, **2000**, (200-202), 379-409.

44. Allen, A. D., Harris, R. O., Loescher, B. R., Stevens, J. R. and Whiteley, R. N., "Dinitrogen complexes of the transition metals," *Chem. Rev.*, **1973**, (73), 11-20.

45. Lokhandwala, K. A., Pinnau, I., He, Z., Amo, K. D., DaCosta, A. R., Wijmans, J. G. and Baker, R. W., "Membrane separation of nitrogen from natural gas: A case study from membrane synthesis to commercial deployment," *J. Membr. Sci.*, **2010**, (346), 270-279.

46. McDonald, T. M., Lee, W. R., Mason, J. A., Wiers, B. M., Hong, C. S. and Long, J. R., "Capture of Carbon Dioxide from Air and Flue Gas in the Alkylamine-Appended Metal-Organic Framework mmen-Mg2(dobpdc)," *J. Am. Chem. Soc.*, **2012**, (134), 7056-7065.

47. Rosi, N. L., Kim, J., Eddaoudi, M., Chen, B., O'Keeffe, M. and Yaghi, O. M., "Rod Packings and Metal-Organic Frameworks Constructed from Rod-Shaped Secondary Building Units," *J. Am. Chem. Soc.*, **2005**, (127), 1504-1518.

48. Dietzel, P. D. C., Morita, Y., Blom, R. and Fjellvaag, H., "An in situ high-temperature single-crystal investigation of a dehydrated metal-organic framework compound and field-induced magnetization of one-dimensional metal-oxygen chains," *Angew. Chem., Int. Ed.*, **2005**, (44), 6354-6358.

49. Dietzel, P. D. C., Panella, B., Hirscher, M., Blom, R. and Fjellvag, H., "Hydrogen adsorption in a nickel based coordination polymer with open metal sites in the cylindrical cavities of the desolvated framework," *Chem. Commun. (Cambridge, U. K.)*, **2006**, 959-961.

50. Nijem, N., Veyan, J.-F., Kong, L., Li, K., Pramanik, S., Zhao, Y., Li, J., Langreth, D. and Chabal, Y. J., "Interaction of Molecular Hydrogen with Microporous Metal Organic Framework Materials at Room Temperature," *J. Am. Chem. Soc.*, **2010**, (132), 1654-1664.

51. Bloch, E. D., Murray, L. J., Queen, W. L., Chavan, S., Maximoff, S. N., Bigi, J. P., Krishna, R., Peterson, V. K., Grandjean, F., Long, G. J., Smit, B., Bordiga, S., Brown, C. M. and Long, J. R., "Selective Binding of O2 over N2 in a Redox-Active Metal-Organic Framework with Open Iron(II) Coordination Sites," *J. Am. Chem. Soc.*, **2011**, (133), 14814-14822.

52. Verma, P., Xu, X. and Truhlar, D. G., "Adsorption on Fe-MOF-74 for C1-C3 Hydrocarbon Separation," *J. Phys. Chem. C*, **2013**, (117), 12648-12660.

53. Wu, H., Zhou, W. and Yildirim, T., "High-Capacity Methane Storage in Metal-Organic Frameworks M2(dhtp): The Important Role of Open Metal Sites," *J. Am. Chem. Soc.*, **2009**, (131), 4995-5000.

54. Valenzano, L., Civalleri, B., Chavan, S., Palomino, G. T., Arean, C. O. and Bordiga, S., "Computational and Experimental Studies on the Adsorption of CO, N2, and CO2 on Mg-MOF-74," *J. Phys. Chem. C*, **2010**, (114), 11185-11191.

55. Yamamoto, A., *Organotrasnition Metal Chemistry*, Wiley, New York, 2986.

56. Crabtree, R. H., *The Organometallic Chemistry of the Transition Metals*, Wiley, New York, 1994.

57. Kohn, W., Becke, A. D. and Parr, R. G., "Density Functional Theory of Electronic Structure," *J. Phys. Chem.*, **1996**, (100), 12974-12980.

58. Dion, M., Rydberg, H., Schroder, E., Langreth, D. C. and Lundqvist, B. I., "van der Waals density functional for general geometries," *Phys Rev Lett*, **2004**, (92), 246401.

59. Lee, K., Murray, É. D., Kong, L., Lundqvist, B. I. and Langreth, D. C., "Higher-accuracy van der Waals density functional," *Phys. Rev. B*, **2010**, (82), 081101.

60. Liechtenstein, A. I., Anisimov, V. I. and Zaanen, J., "Density-functional theory and strong interactions: orbital ordering in Mott-Hubbard insulators," *Phys. Rev. B*, **1995**, (52), R5467-R5470.

61. Zhao, Y. and Truhlar, D. G., "Density Functionals with Broad Applicability in Chemistry," *Acc. Chem. Res.*, **2008**, (41), 157-167.

62. Zhao, Y. and Truhlar, D. G., "Applications and validations of the Minnesota density functionals," *Chem. Phys. Lett.*, **2011**, (502), 1-13.

63. Zhao, Y. and Truhlar, D. G., "A new local density functional for main-group thermochemistry, transition metal bonding, thermochemical kinetics, and noncovalent interactions," *J. Chem. Phys.*, **2006**, (125), 194101.

64. Zhao, Y. and Truhlar, D. G., "The M06 suite of density functionals for main group thermochemistry, thermochemical kinetics, noncovalent interactions, excited states, and transition elements: two new functionals and systematic testing of four M06-class functionals and 12 other functionals," *Theor. Chem. Acc.*, **2008**, (120), 215-241.

65. Peverati, R. and Truhlar, D. G., "M11-L: A Local Density Functional That Provides Improved Accuracy for Electronic Structure Calculations in Chemistry and Physics," *J. Phys. Chem. Lett.*, **2012**, (3), 117-124.

66. Becke, A. D., "A new mixing of Hartree-Fock and local-density-functional theories," *J. Chem. Phys.*, **1993**, (98), 1372-1377.

67. Neese, F., Hansen, A. and Liakos, D. G., "Efficient and accurate approximations to the local coupled cluster singles doubles method using a truncated pair natural orbital basis," *J. Chem. Phys.*, **2009**, (131), 064103.

68. Andersson, K., Malmqvist, P. A. and Roos, B. O., "Second-order perturbation theory with a complete active space self-consistent field

reference function," *J. Chem. Phys.*, **1992**, (96), 1218-1226.

69. Fohlmeister, L., Liu, S., Schulten, C., Moubaraki, B., Stasch, A., Cashion, J. D., Murray, K. S., Gagliardi, L. and Jones, C., "Low-Coordinate Iron(I) and Manganese(I) Dimers: Kinetic Stabilization of an Exceptionally Short Fe-Fe Multiple Bond," *Angew. Chem., Int. Ed.*, **2012**, (51), 8294-8298, S8294/8291-S8294/8233.

70. Li Manni, G., Dzubak, A. L., Mulla, A., Brogden, D. W., Berry, J. F. and Gagliardi, L., "Assessing Metal-Metal Multiple Bonds in Cr-Cr, Mo-Mo, and W-W Compounds and a Hypothetical U-U Compound: A Quantum Chemical Study Comparing DFT and Multireference Methods," *Chem. - Eur. J.*, **2012**, (18), 1737-1749, S1737/1731-S1737/1748.

71. Sanz, R., Martinez, F., Orcajo, G., Wojtas, L. and Briones, D., "Synthesis of a honeycomb-like Cu-based metal-organic framework and its carbon dioxide adsorption behaviour," *Dalton Trans.*, **2013**, (42), 2392-2398.

72. Marenich, A. V., Jerome, S. V., Cramer, C. J. and Truhlar, D. G., "Charge Model 5: An Extension of Hirshfeld Population Analysis for the Accurate Description of Molecular Interactions in Gaseous and Condensed Phases," *J. Chem. Theory Comput.*, **2012**, (8), 527-541.

73. Marenich, A. V., Cramer, C. J. and Truhlar, D. G., *CM5PAC*, University of Minnesota, Minneapolis, 2011.

74. M. J. Frisch, G. W. Trucks, *et al.*, *Gaussian09*, Gaussian Inc., Wallingford CT 2009.

75. Zhao, Y., Peverati, R., Yang, K. and Truhlar, D. G., *MN-GFM 6.4*, University of Minnesota, Minneapolis, 2012.

76. Kresse, G. and Furthmueller, J., "Efficient iterative schemes for ab initio total-energy calculations using a plane-wave basis set," *Phys. Rev. B*, **1996**, (54), 11169-11186.

77. Neese, F., "The ORCA program system," *WIREs Comput. Mol. Sci.*, **2012**, (2), 73-78.

78. Aquilante, F., De Vico, L., Ferre, N., Ghigo, G., Malmqvist, P.-a., Neogrady, P., Pedersen, T. B., Pitonak, M., Reiher, M., Roos, B. O., Serrano-Andres, L., Urban, M., Veryazov, V. and Lindh, R., "MOLCAS 7: The Next Generation," *J. Comput. Chem.*, **2010**, (31), 224-247.

79. E.J. Baerends, T. Ziegler, *et al.*, *ADF2013*, SCM, Theoretical Chemistry, Vrije Universiteit, Amdsterdam, The Netherlands, http://www.scm.com.

80. Te Velde, G., Bickelhaupt, F. M., Baerends, E. J., Fonseca Guerra, C., Van Gisbergen, S. J. A., Snijders, J. G. and Ziegler, T., "Chemistry with ADF," *J. Comput. Chem.*, **2001**, (22), 931-967.

81. Fonseca Guerra, C., Snijders, J. G., te Velde, G. and Baerends, E. J., "Towards an order-N DFT method," *Theor Chem Acc*, **1998**, (99), 391-403.

82. Kresse, G., Gil, A. and Sautet, P., "Significance of single-electron energies for the description of CO on Pt(111)," *Phys. Rev. B*, **2003**, (68), 073401.

83. Bloch, E. D., Queen, W. L., Krishna, R., Zadrozny, J. M., Brown, C. M. and Long, J. R., "Hydrocarbon Separations in a Metal-Organic Framework with Open Iron(II) Coordination Sites," *Science*, **2012**, (335), 1606-1610.

84. Mitoraj, M. P., Michalak, A. and Ziegler, T., "A Combined Charge and Energy Decomposition Scheme for Bond Analysis," *J. Chem. Theory Comput.*, **2009**, (5), 962-975.

85. Reed, A. E., Curtiss, L. A. and Weinhold, F., "Intermolecular interactions from a natural bond orbital, donor-acceptor viewpoint," *Chem Rev*, **1988**, (88), 899-926.

86. Crans, D. C., Yang, L., Gaidamauskas, E., Khan, R., Jin, W. and Simonis, U., in *Paramagnetic Resonance of Metallobiomolecules*, American

Chemical Society2003, vol. 858, ch. 17, pp. 304-326.

87. Rocks, S. S., Brennessel, W. W., Machonkin, T. E. and Holland, P. L., "Solid-state and proton NMR characterization of an iron(II) complex of a tridentate, facially coordinating N,N,O donor ligand," *Inorg. Chim. Acta*, **2009**, (362), 1387-1390.

88. Turega, S., Whitehead, M., Hall, B. R., Haddow, M. F., Hunter, C. A. and Ward, M. D., "Selective guest recognition by a self-assembled paramagnetic cage complex," *Chem. Comm.*, **2012**, (48), 2752-2754.

89. Nadaud, P. S., Helmus, J. J., Kall, S. L. and Jaroniec, C. P., "Paramagnetic ions enable tuning of nuclear relaxation rates and provide long-range structural restraints in solid-state NMR of proteins," *J. Am. Chem. Soc.*, **2009**, (131), 8108-8120.

90. Kaupp, M. and Kohler, F. H., "Combining NMR spectroscopy and quantum chemistry as tools to quantify spin density distributions in molecular magnetic compounds," *Coord. Chem. Rev.*, **2009**, (253), 2376-2386.

91. Shaibat, M. A., Casabianca, L. B., Wickramasinghe, N. P., Guggenheim, S., de Dios, A. C. and Ishii, Y., "Characterization of polymorphs and solid-state reactions for paramagnetic systems by 13C solid-state NMR and ab initio calculations," *J. Am. Chem. Soc.*, **2007**, (129), 10968-10969.

92. Amouri, H., Desmarets, C. and Moussa, J., "Confined Nanospaces in Metallocages: Guest Molecules, Weakly Encapsulated Anions, and Catalyst Sequestration," *Chem. Rev.*, **2012**, (112), 2015-2041.

93. Fabbrizzi, L. and Poggi, A., "Anion recognition by coordinative interactions: metal-amine complexes as receptors," *Chem. Soc. Rev.*, **2013**, (42), 1681-1699.

94. Amendola, V. and Fabbrizzi, L., "Anion receptors that contain metals as structural units," *Chem. Comm.*, **2009**, 513-531.

95. Ono, K., Yoshizawa, M., Akita, M., Kato, T., Tsunobuchi, Y., Ohkoshi, S.-i. and Fujita, M., "Spin Crossover by Encapsulation," *J. Am. Chem. Soc.*, **2009**, (131), 2782-2783.

96. Olguín, J. and Brooker, S., in *Spin-Crossover Materials*, John Wiley & Sons Ltd2013, pp. 77-120.

97. Halcrow, M. A., "Structure:function relationships in molecular spin-crossover complexes," *Chem. Soc. Rev.*, **2011**, (40), 4119-4142.

98. Bousseksou, A., Molnár, G., Real, J. A. and Tanaka, K., "Spin crossover and photomagnetism in dinuclear iron(II) compounds," *Coord. Chem. Rev.*, **2007**, (251), 1822-1833.

99. Aromí, G., Barrios, L. A., Roubeau, O. and Gamez, P., "Triazoles and tetrazoles: Prime ligands to generate remarkable coordination materials," *Coord. Chem. Rev.*, **2011**, (255), 485-546.

100. Murray, K. S. and Kepert, C. J., in *Spin Crossover in Transition Metal Compounds I*, eds. Gütlich, P. and Goodwin, H. A., Springer Berlin Heidelberg2004, vol. 233, ch. 8, pp. 195-228.

101. Gütlich, P. and Goodwin, H. A., in *Spin Crossover in Transition Metal Compounds I*, eds. Gütlich, P. and Goodwin, H. A., Springer Berlin Heidelberg2004, vol. 233, ch. 1, pp. 1-47.

102. Létard, J.-F., Guionneau, P. and Goux-Capes, L., in *Spin Crossover in Transition Metal Compounds III*, Springer Berlin Heidelberg2004, vol. 235, ch. 10, pp. 221-249.

103. Hauser, A., Jeftić, J., Romstedt, H., Hinek, R. and Spiering, H., "Cooperative phenomena and light-induced bistability in iron(II) spin-

crossover compounds," *Coord. Chem. Rev.*, **1999**, (190-192), 471-491.

104. Kahn, O. and Martinez, C. J., "Spin-Transition Polymers: From Molecular Materials Toward Memory Devices," *Science*, **1998**, (279), 44-48.

105. Kitchen, J. A., Olguín, J., Kulmaczewski, R., White, N. G., Milway, V. A., Jameson, G. N. L., Tallon, J. L. and Brooker, S., "Effect of N4-Substituent Choice on Spin Crossover in Dinuclear Iron(II) Complexes of Bis-Terdentate 1,2,4-Triazole-Based Ligands," *Inorg. Chem.*, **2013**, (52), 11185-11199.

106. Bilbeisi, R. A., Zarra, S., Feltham, H. L., Jameson, G. N., Clegg, J. K., Brooker, S. and Nitschke, J. R., "Guest binding subtly influences spin crossover in an FeII(4)L(4) capsule," *Chem. Eur. J.*, **2013**, (19), 8058-8062.

107. Kitchen, J. A., White, N. G., Boyd, M., Moubaraki, B., Murray, K. S., Boyd, P. D. W. and Brooker, S., "Iron(II) Tris-[N4-substituted-3,5-di(2-pyridyl)-1,2,4-triazole] Complexes: Structural, Magnetic, NMR, and Density Functional Theory Studies," *Inorg. Chem.*, **2009**, (48), 6670-6679.

108. Bhattacharjee, A., Roy, M., Ksenofontov, V., Kitchen, J. A., Brooker, S. and Gütlich, P., "Pressure Effect Studies on the Spin-Transition Behavior of a Dinuclear Iron(II) Compound," *Eur. J. Inorg. Chem.*, **2013**, (2013), 843-849.

109. Cowan, M. G., Olguín, J., Narayanaswamy, S., Tallon, J. L. and Brooker, S., "Reversible Switching of a Cobalt Complex by Thermal, Pressure, and Electrochemical Stimuli: Abrupt, Complete, Hysteretic Spin Crossover," *J. Am. Chem. Soc.*, **2011**, (134), 2892-2894.

110. Chakraborty, P., Boillot, M.-L., Tissot, A. and Hauser, A., "Photoinduced Relaxation Dynamics in Iron(II) Spin-Crossover Nanoparticles: The Significance of Crystallinity," *Angew. Chem., Int. Ed.*, **2013**, (52), 7139-7142.

111. Mal, P., Schultz, D., Beyeh, K., Rissanen, K. and Nitschke, J. R., "An unlockable-relockable iron cage by subcomponent self-assembly," *Angew. Chem., Int. Ed.*, **2008**, (47), 8297-8301.

112. Wolny, J. A., Paulsen, H., Trautwein, A. X. and Schünemann, V., "Density functional theory calculations and vibrational spectroscopy on iron spin-crossover compounds," *Coord. Chem. Rev.*, **2009**, (253), 2423-2431.

113. Kepenekian, M., Robert, V., Le Guennic, B. and De Graaf, C., "Energetics of [Fe(NCH)6]2+ via CASPT2 calculations: A spin-crossover perspective," *J. Comp. Chem.*, **2009**, (30), 2327-2333.

114. Bowman, D. N. and Jakubikova, E., "Low-spin versus high-spin ground state in pseudo-octahedral iron complexes," *Inorg. Chem.*, **2012**, (51), 6011-6019.

115. Reiher, M., Salomon, O. and Artur Hess, B., "Reparameterization of hybrid functionals based on energy differences of states of different multiplicity," *Theor Chem Acc*, **2001**, (107), 48-55.

116. Droghetti, A., Alfè, D. and Sanvito, S., "Assessment of density functional theory for iron(II) molecules across the spin-crossover transition," *J. Chem. Phys.*, **2012**, (137), -.

117. Fouqueau, A., Mer, S., Casida, M. E., Lawson Daku, L. M., Hauser, A., Mineva, T. and Neese, F., "Comparison of density functionals for energy and structural differences between the high- [5T2g: (t2g)4(eg)2] and low- [1A1g: (t2g)6(eg)0] spin states of the hexaquoferrous cation [Fe(H2O)6]2+," *J. Chem. Phys.*, **2004**, (120), 9473-9486.

118. Deeth, R. J. and Fey, N., "The performance of nonhybrid density functionals for calculating the structures and spin states of Fe(II) and Fe(III) complexes," *J. Comp. Chem.*, **2004**, (25), 1840-1848.

119. Lawson Daku, L. M., Vargas, A., Hauser, A., Fouqueau, A. and Casida, M. E., "Assessment of Density Functionals for the High-Spin/Low-Spin Energy Difference in the Low-Spin Iron(II)

Tris(2,2′-bipyridine) Complex," *Chem. Phys. Chem.*, **2005**, (6), 1393-1410.

120. Kepp, K. P., "Consistent descriptions of metal–ligand bonds and spin-crossover in inorganic chemistry," *Coord. Chem. Rev.*, **2013**, (257), 196-209.

121. Pierloot, K. and Vancoillie, S., "Relative energy of the high-(5T2g) and low-(1A1g) spin states of [Fe(H2O)6]2+, [Fe(NH3)6]2+, and [Fe(bpy)3]2+: CASPT2 versus density functional theory," *J. Chem. Phys.*, **2006**, (125), 124303.

122. Paulsen, H., Schünemann, V. and Wolny, J. A., "Progress in Electronic Structure Calculations on Spin-Crossover Complexes," *Eur. J. Inorg. Chem.*, **2013**, (2013), 628-641.

123. Herchel, R. and Travnicek, Z., "5-Aminotetrazole induces spin crossover in iron(iii) pentadentate Schiff base complexes: experimental and theoretical investigations," *Dalton Trans.*, **2013**, (42), 16279-16288.

124. Le Guennic, B., Floyd, T., Galan, B. R., Autschbach, J. and Keister, J. B., "Paramagnetic Effects on the NMR Spectra of "Diamagnetic" Ruthenium(bis-phosphine)(bis-semiquinone) Complexes," *Inorg. Chem.*, **2009**, (48), 5504-5511.

125. Brewer, G., Olida, M. J., Schmiedekamp, A. M., Viragh, C. and Zavalij, P. Y., "A DFT computational study of spin crossover in iron(iii) and iron(ii) tripodal imidazole complexes. A comparison of experiment with calculations," *Dalton Trans.*, **2006**, 5617-5629.

126. Smulders, M. M., Zarra, S. and Nitschke, J. R., "Quantitative understanding of guest binding enables the design of complex host-guest behavior," *J. Am. Chem. Soc.*, **2013**, (135), 7039-7046.

127. Ronson, T. K., Giri, C., Beyeh, N. K., Minkkinen, A., Topic, F., Holstein, J. J., Rissanen, K. and Nitschke, J. R., "Size-selective encapsulation of hydrophobic guests by self-assembled M4L6 cobalt and nickel cages," *Chem. Eur. J.*, **2013**, (19), 3374-3382.

128. Faust, T. B., Tuna, F., Timco, G. A., Affronte, M., Bellini, V., Wernsdorfer, W. and Winpenny, R. E. P., "Controlling magnetic communication through aromatic bridges by variation in torsion angle," *Dalton Trans.*, **2012**, (41), 13626-13631.

129. Riddell, I. A., Smulders, M. M., Clegg, J. K., Hristova, Y. R., Breiner, B., Thoburn, J. D. and Nitschke, J. R., "Anion-induced reconstitution of a self-assembling system to express a chloride-binding Co10L15 pentagonal prism," *Nat. Chem.*, **2012**, (4), 751-756.

130. Hedegård, E. D., Kongsted, J. and Sauer, S. P. A., "Validating and Analyzing EPR Hyperfine Coupling Constants with Density Functional Theory," *J. Chem. Theory Comp.*, **2013**, (9), 2380-2388.

131. Klaeui, W., Eberspach, W. and Guetlich, P., "Spin-crossover cobalt(III) complexes: steric and electronic control of spin state," *Inorg. Chem.*, **1987**, (26), 3977-3982.

132. Grimme, S., Ehrlich, S. and Goerigk, L., "Effect of the damping function in dispersion corrected density functional theory," *J. Comp. Chem.*, **2011**, (32), 1456-1465.

133. Shannon, R. D., "Revised Effective Ionic-Radii and Systematic Studies of Interatomic Distances in Halides and Chalcogenides," *Acta Crystallographica Section A*, **1976**, (32), 751-767.

134. Dolg, M., Wedig, U., Stoll, H. and Preuss, H., "Energy-adjusted *ab initio* pseudopotentials for the first row transition elements," *J. Chem. Phys.*, **1987**, (86), 866-872.

135. Martin, J. M. L. and Sundermann, A., "Correlation consistent valence basis sets for use with the Stuttgart–Dresden–Bonn relativistic effective core potentials: The atoms Ga–Kr and In–Xe," *J. Chem. Phys.*, **2001**, (114), 3408-3420.

136. Easton, R. E., Giesen, D. J., Welch, A., Cramer, C. J. and Truhlar, D. G., "The MIDI! basis set for quantum mechanical calculations of molecular geometries and partial charges," *Theor. Chem. Acta*, **1996**, (93), 281-301.

137. Ribeiro, R. F., Marenich, A. V., Cramer, C. J. and Truhlar, D. G., "Use of Solution-Phase Vibrational Frequencies in Continuum Models for the Free Energy of Solvation," *J. Phys. Chem. B*, **2011**, (115), 14556-14562.

138. Pritchard, B. and Autschbach, J., "Theoretical Investigation of Paramagnetic NMR Shifts in Transition Metal Acetylacetonato Complexes: Analysis of Signs, Magnitudes, and the Role of the Covalency of Ligand–Metal Bonding," *Inorg. Chem.*, **2012**, (51), 8340-8351.

139. Cheeseman, J. R., Trucks, G. W., Keith, T. A. and Frisch, M. J., "A comparison of models for calculating nuclear magnetic resonance shielding tensors," *J. Chem. Phys.*, **1996**, (104), 5497-5509.

140. Rinkevicius, Z., Vaara, J., Telyatnyk, L. and Vahtras, O., "Calculations of nuclear magnetic shielding in paramagnetic molecules," *J. Chem. Phys.*, **2003**, (118), 2550-2561.

141. Wachters, A. J. H., "Gaussian Basis Set for Molecular Wavefunctions Containing Third-Row Atoms," *J. Chem. Phys.*, **1970**, (52), 1033-1036.

142. Hay, P. J., "Gaussian basis sets for molecular calculations. The representation of 3d orbitals in transition-metal atoms," *J. Chem. Phys.*, **1977**, (66), 4377-4384.

143. Barone, V., in *Recent Advances in Density Functional Methods, Part I*, ed. Chong, D. P., World Scientific Publ. Co., Singapore1996.

144. McLean, A. D. and Chandler, G. S., "Contracted Gaussian basis sets for molecular calculations. I. Second row atoms, Z=11–18," *J. Chem. Phys.*, **1980**, (72), 5639-5648.

145. Krishnan, R., Binkley, J. S., Seeger, R. and Pople, J. A., "Self-consistent molecular orbital methods. XX. A basis set for correlated wave functions," *J. Chem. Phys.*, **1980**, (72), 650-654.

146. Neese, F., "The ORCA program system," *WIREs Comput. Mol. Sci.*, **2012**, (2), 73-78.

147. Strahl, B. D. and Allis, C. D., "The language of covalent histone modifications," *Nature*, **2000**, (403), 41-45.

148. Filippakopoulos, P. and Knapp, S., "Targeting bromodomains: epigenetic readers of lysine acetylation," *Nat Rev Drug Discov*, **2014**, (13), 337-356.

149. Filippakopoulos, P., Qi, J., *et al.*, "Selective inhibition of BET bromodomains," *Nature*, **2010**, (468), 1067-1073.

150. Nicodeme, E., Jeffrey, K. L., Schaefer, U., Beinke, S., Dewell, S., Chung, C.-w., Chandwani, R., Marazzi, I., Wilson, P., Coste, H., White, J., Kirilovsky, J., Rice, C. M., Lora, J. M., Prinjha, R. K., Lee, K. and Tarakhovsky, A., "Suppression of inflammation by a synthetic histone mimic," *Nature*, **2010**, (468), 1119-1123.

151. Vidler, L. R., Brown, N., Knapp, S. and Hoelder, S., "Druggability Analysis and Structural Classification of Bromodomain Acetyl-lysine Binding Sites," *J. Med. Chem.*, **2012**, (55), 7346-7359.

152. Thompson, A. D., Dugan, A., Gestwicki, J. E. and Mapp, A. K., "Fine-Tuning Multiprotein Complexes Using Small Molecules," *ACS Chem. Bio.*, **2012**, (7), 1311-1320.

153. Pomerantz, W. C., Wang, N., Lipinski, A. K., Wang, R., Cierpicki, T. and Mapp, A. K., "Profiling the Dynamic Interfaces of Fluorinated Transcription Complexes for Ligand Discovery and Characterization," *ACS Chem. Bio.*, **2012**, (7), 1345-1350.

154. Mishra, N. K., Urick, A. K., Ember, S. W. J., Schönbrunn, E. and Pomerantz, W. C., "Fluorinated Aromatic Amino Acids Are

Sensitive 19F NMR Probes for Bromodomain-Ligand Interactions," *ACS Chemical Biology*, **2014**, (9), 2755-2760.

155. Gee, C. T., Koleski, E. J. and Pomerantz, W. C. K., "Fragment Screening and Druggability Assessment for the CBP/p300 KIX Domain through Protein-Observed 19F NMR Spectroscopy," *Angew. Chem., Int. Ed.*, **2015**, (54), 3735-3739.

156. Marsh, E. N. G. and Suzuki, Y., "Using 19F NMR to Probe Biological Interactions of Proteins and Peptides," *ACS Chem. Bio.*, **2014**, (9), 1242-1250.

157. Dhalluin, C., Carlson, J. E., Zeng, L., He, C., Aggarwal, A. K., Zhou, M.-M. and Zhou, M.-M., "Structure and ligand of a histone acetyltransferase bromodomain," *Nature*, **1999**, (399), 491-496.

158. Leung, E. W. W., Yagi, H., Harjani, J. R., Mulcair, M. D., Scanlon, M. J., Baell, J. B. and Norton, R. S., "19F NMR as a Probe of Ligand Interactions with the iNOS Binding site of SPRY Domain-Containing SOCS Box Protein 2," *Chem. Bio. Drug Des.*, **2014**, (84), 616-625.

159. Adamo, C. and Barone, V., "Toward reliable density functional methods without adjustable parameters: The PBE0 model," *The Journal of Chemical Physics*, **1999**, (110), 6158-6170.

160. Becke, A. D., "Density-functional thermochemistry. III. The role of exact exchange," *The Journal of Chemical Physics*, **1993**, (98), 5648.

161. Chong, D. P., *Recent advances in density functional methods*, World Scientific, Singapore ; River Edge, N.J., 1995.

162. Krishnan, R., Binkley, J. S., Seeger, R. and Pople, J. A., "Self-consistent molecular orbital methods. XX. A basis set for correlated wave functions," *The Journal of Chemical Physics*, **1980**, (72), 650-654.

163. Sanders, L. K. and Oldfield, E., "Theoretical Investigation of 19F NMR Chemical Shielding Tensors in Fluorobenzenes," *The Journal of Physical Chemistry A*, **2001**, (105), 8098-8104.

164. Hospital, A., Andrio, P., Fenollosa, C., Cicin-Sain, D., Orozco, M. and Gelpí, J. L., "MDWeb and MDMoby: an integrated web-based platform for molecular dynamics simulations," *Bioinformatics*, **2012**, (28), 1278-1279.

165. Hornak, V., Abel, R., Okur, A., Strockbine, B., Roitberg, A. and Simmerling, C., "Comparison of multiple Amber force fields and development of improved protein backbone parameters," *Proteins: Structure, Function, and Bioinformatics*, **2006**, (65), 712-725.

166. Best, R. B. and Hummer, G., "Optimized Molecular Dynamics Force Fields Applied to the Helix−Coil Transition of Polypeptides," *J. Phys. Chem. B*, **2009**, (113), 9004-9015.

167. Gelpí, J. L., Kalko, S. G., Barril, X., Cirera, J., de la Cruz, X., Luque, F. J. and Orozco, M., "Classical molecular interaction potentials: Improved setup procedure in molecular dynamics simulations of proteins," *Proteins: Structure, Function, and Bioinformatics*, **2001**, (45), 428-437.

168. Phillips, J. C., Braun, R., Wang, W., Gumbart, J., Tajkhorshid, E., Villa, E., Chipot, C., Skeel, R. D., Kalé, L. and Schulten, K., "Scalable molecular dynamics with NAMD," *J. Comp. Chem.*, **2005**, (26), 1781-1802.

169. O'Boyle, N., Banck, M., James, C., Morley, C., Vandermeersch, T. and Hutchison, G., "Open Babel: An open chemical toolbox," *J. Cheminfo.*, **2011**, (3), 33.

170. Weigend, F. and Ahlrichs, R., "Balanced basis sets of split valence, triple zeta valence and quadruple zeta valence quality for H to Rn: Design and assessment of accuracy," *Phys. Chem. Chem. Phys.*, **2005**, (7), 3297-3305.

171. Rietjens, I. M. C. M., Soffers, A. E. M. F., Veeger, C. and Vervoort, J., "Regioselectivity of

cytochrome P-450 catalyzed hydroxylation of fluorobenzenes predicted by calculated frontier orbital substrate characteristics," *Biochemistry*, **1993**, (32), 4801-4812.

172. Peelen, S., Rietjens, I. M. C. M., Boersma, M. G. and Vervoort, J., "Conversion of Phenol Derivatives to Hydroxylated Products by Phenol Hydroxylase from Trichosporon cutaneum," *European Journal of Biochemistry*, **1995**, (227), 284-291.

173. Božilović, J., Bats, J. W. and Engels, J. W., "Synthesis and structure of fluoroindole nucleosides," *Canadian Journal of Chemistry*, **2007**, (85), 283-292.

174. Yinon, J., "Field Detection and Monitoring of Explosives," *Trends Anal. Chem.*, **2002**, (22), 292-300.

175. Steinfield, J. I. and Wormhoudt, J., "Explosives Detection: A Challenge for Physical Chemistry," *Annu. Rev. Phys. Chem.*, **1998**, (49), 203-232.

176. Moore, D. S., "Instrumentation for Trace Detection of High Explosives," *Rev. Sci. Instrum.*, **2004**, (75), 2499-2512.

177. Zang, J., Guo, C. X., Hu, F., Yu, L. and Li, C. M., "Electrochemical Detection of Ultratrace Nitroaromatic Explosives Using Ordered Mesoporous Carbon," *Anal. Chim. Acta*, **2011**, (683), 187-191.

178. Yinon, J., "Detection of Explosives by Electronic Noses," *Anal. Chem.*, **2003**, (75), 99A-105A.

179. Sohn, H., Sailor, M. J., Magde, D. and Trogler, W. C., "Detection of Nitroaromatic Explosives Based on Photoluminescent Polymers Containing Metallones," *J. Am. Chem. Soc.*, **2003**, (125), 3821-3830.

180. Saravanan, N. P., Venugopalan, S., Senthilkumar, N., Santhosh, P., Kavita, B. and Prabu, H. G., "Voltammetric Determination of Nitroaromatic and Nitramine Explosives Contamination in Soil," *Talanta*, **2006**, (69), 656-662.

181. Ponnu, A., Edwards, N. Y. and Anslyn, E. V., "Pattern Recognition Based Identification of Nitrated Explosives," *New J. Chem.*, **2008**, (32), 848-855.

182. Naddo, T., Che, Y., Zhang, W., Balakrishnan, K., Yang, X., Yen, M., Zhao, J., Moore, J. S. and Zang, L., "Detection of Explosives with a Fluorescent Nanofibril Film," *J. Am. Chem. Soc.*, **2007**, (129), 6978-6979.

183. Krausa, M., Doll, J., Schorb, K., Böke, W. and Hambitzer, G., "Fast Electrochemical Detection of Nitro- and Aminoaromates in Soils and Liquids," *Propellants, Explosives, Pyrotechnics*, **1997**, (22), 156-159.

184. Harper, R. J., Almirall, J. R. and Furton, K. G., "Identification of Dominant Odor Chemicals Emanating from Explosives for Use in Developing Optimal Training Aid Combinations and Mimics for Canine Detection," *Talanta*, **2005**, (67), 313-327.

185. Haderlein, S. B., Weissmahr, K. W. and Schwarzenbach, R. P., "Specific Adsorption of Nitroaromatic Explosives and Pesticides to Clay Materials," *Environ. Sci. Technol.*, **1996**, (30), 612-622.

186. Forzani, E. S., Lu, D., Leright, M. J., Aguilar, A. D., Tsow, F., Inglesias, R. A., Zhang, Q., Lu, J., Li, J. and Tao, N., "A Hybrid Electrochemical-Colorimetric Sensing Platform for Detection of Explosives," *J. Am. Chem. Soc*, **2009**, (131), 1390-1391.

187. Agüí, L., Vega-Montenegro, D., Yáñez-Sedeño, P. and Pingarrón, J. M., "Rapid Voltammetric Detection of Nitroaromatic Explosives at Electrochemically Activated Carbon-Fibre Surfaces," *Anal. Bioanal. Chem.*, **2005**, (382), 381-387.

188. Yuan, C.-X., Fan, Y.-R., Tao, Z., Guo, H.-X., Zhang, J.-X., Wang, Y.-L., Shan, D.-L. and Lu, X.-Q., "A New Electrochemical Sensor of Nitro Aromatic Compound Based on Three-Dimensional Porous Pt–Pd Nanoparticles

Supported by Graphene–Multiwalled Carbon Nanotube Composite," *Biosens. Bioelectron.*, **2014**, (58), 85-91.

189. Seah, T. H., Poh, H. L., Chua, C. K., Sofer, Z. and Pumera, M., "Towards Graphane Applications in Security: The Electrochemical Detection of Trinitrotoluene in Seawater on Hydrogenated Graphene," *Electroanalysis*, **2014**, (26), 62-68.

190. Toh, H. S., Ambrosi, A. and Pumera, M., "Electrocatalytic Effect of ZnO Nanoparticles on Reduction of Nitroaromatic Compounds," *Catalysis Science & Technology*, **2013**, (3), 123-127.

191. O'Mahony, A. M. and Wang, J., "Nanomaterial-Based Electrochemical Detection of Explosives: A Review of Recent Developments," *Analytical Methods*, **2013**, (5), 4296-4309.

192. Ong, B. K., Poh, H. L., Chua, C. K. and Pumera, M., "Graphenes Prepared by Hummers, Staudenmaier and Hofmann Methods for Analysis of TNT-Based Nitroaromatic Explosives in Seawater," *Electroanalysis*, **2012**, (24), 2085-2093.

193. Casey, M. C. and Cliffel, D. E., "Surface Adsorption and Electrochemical Reduction of 2,4,6-Trinitrotoluene on Vanadium Dioxide," *Anal. Chem.*, **2015**, (87), 334-337.

194. Bond, J. A. and Rickert, D. E., "Metabolism of 2,4-Dinitro[14C]toluene by Freshly Isolated Fischer-344 Rat Primary Hepatocytes," *Drug Metab. Disp.*, **1981**, (9), 10-14.

195. Phelan, J. M. and Barnett, J. L., "Chemical Sensing Thresholds for Mine Detection Dogs," *Proceedings of SPIE*, **2002**, (4742), 532-543.

196. Pearson, J., "The Reduction of Nitrocompounds at the Dropping-Mercury Cathode," *Trans. Faraday Soc.*, **1948**, (44), 683-697.

197. Zhang, H.-X. and Zhang, J.-H., "Voltammetric Detection of Nitroaromatic Compounds Using Carbon-Nanomaterials-Based Electrodes," *Can. J. Chem.*, **2011**, (89), 8-12.

198. Zhang, H.-X., Cao, A.-M., Hu, J.-S., Wan, L.-J. and Lee, S.-T., "Electrochemical Sensor for Detecting Ultratrace Nitroaromatic Compounds Using Mesoporous SiO_2-Modified Electrode," *Anal. Chem.*, **2006**, (78), 1967-1971.

199. Nie, D., Li, P., Zhang, D., Zhou, T., Liang, Y. and Shi, G., "Simultaneous Determination of Nitroaromatic Compounds in Water Using Capillary Electrophoresis with Amperometric Detection on an Electrode Modified with a Mesoporous Nano-Structured Carbon Material," *Electrophoresis*, **2010**, (31), 2981-2988.

200. Masunaga, K., Hayama, K., Onodera, T., Hayashi, K., Miura, N., Matsumoto, K. and Toko, K., "Detection of Aromatic Nitro Compounds with Electrode Polarization Controlling Sensor," *Sens. Actuators B*, **2005**, (108), 427-434.

201. Bratin, K., Kissinger, P. T., Briner, R. C. and Bruntlett, C. S., "Determination of Nitro Aromatic, Nitramine, and Nitrate Ester Explosive Compounds in Explosive Mixtures and Gunshot Residue by Liquid Chromatography and Reductive Electrochemical Detection," *Anal. Chim. Acta*, **1981**, (130), 295-311.

202. Smith, W. H. and Bard, A. J., "Electrochemical Reactions of Organic Compounds in Liquid Ammonia. II. Nitrobenzene and Nitrosobenzene," *J. Am. Chem. Soc.*, **1975**, (97), 5203-5210.

203. Cyr, A., Hout, P., Marcoux, J.-F., Belot, G., Laviron, E. and Lessard, J., "The Electrochemical Reduction of Nitrobenzene and Azoxybenzene in Neutral and Basic Aqueous Methanolic Solutions at Polycrystalline Copper and Nickel Electrodes," *Electrochim. Acta*, **1989**, (34), 439-445.

204. Geske, D. H. and Maki, A. H., "Electrochemical Generation of Free Radicals and Their Study by Electron Spin Resonance Spectroscopy; the Nitrobenzene Anion Radical," *J. Am. Chem. Soc.*, **1960**, (82), 2671-2676.

205. Carre, B. and Belin, P., "Etude de la Reduction Polargraphique du Nitrobenzene en Solution Dan le Dimethylformamide (DMF) en Presence de Donneurs de Protons," *C. R. Acad. Sci. Serie C*, **1973**, (276), 1365-1368.

206. Zuman, P., Fijalek, Z., Dumanovic, D. and Suznjevic, D., "Polarographic and Electrochemical Studies of Some Aromatic and Heterocyclic Nitro Compounds, Part I: General Mechanistic Aspects," *Electroanalysis*, **1992**, (4), 783-794.

207. Macias-Ruvalcaba, N. A. and Evans, D. H., "Study of the Effects of Ion Pairing and Activity Coefficients on the Separation in Standard Potentials for Two-Step Reduction of Dinitroaromatics," *J. Phys. Chem. B*, **2005**, (109), 14642-14647.

208. Fry, A. J., "Strong Ion-Pairing Effects in a Room Temperature Ionic Liquid," *J. Electroanal. Chem.*, **2003**, (546), 35-39.

209. Sadek, H. and Abd-El-Nabey, B. A., "Polarography of Nitrobenzene in Aqueous Solutions and in Water-Alcohol Mixtures," *Electrochim. Acta*, **1972**, (17), 2065-2075.

210. Vijayalakshamma, S. K. and Subrahmanya, R. S., "Studies of the Polarographic and Coulometric Behaviour of Aromatic Nitro-Compounds: I. Nitrobenzene in Ethanol," *Journal of Electroanalytical Chemistry and Interfacial Electrochemistry*, **1969**, (23), 99-114.

211. Chua, C. K., Pumera, M. and Rulíšek, L., "Reduction Pathways of 2,4,6-Trinitrotoluene: An Electrochemical and Theoretical Study," *J. Phys. Chem. C*, **2012**, (116), 4243-4251.

212. Olson, E. J., Xiong, T. T., Cramer, C. J. and Bühlmann, P., "Interaction of a Weakly Acidic Dinitroaromatic with Alkylamines: Avoiding the Meisenheimer Trap," *J. Am. Chem. Soc.*, **2011**, (133), 12858-12865.

213. Bard, A. J. and Faulkner, L. R., *Electrochemical Methods: Fundamentals and Applications*, Wiley, New York, 2001.

214. Ciordano, M. C., Macagno, V. A. and Sereno, R., "Kinetics and Mechanism of Reaction of Hydrogen Evolution on Platinum and Gold Electrodes in Acetonitrile," *An. Asoc. Quim. Argent.*, **1977**, (65), 71-84.

215. Barrette, W. C., Johnson, H. W. and Sawyer, D. T., "Voltammetric Evaluation of the Effective Acidities (pKa) for Bronsted Acids in Aprotic Solvents," *Anal. Chem.*, **1984**, (56), 1890-1898.

216. Barrows, S. E., Cramer, C. J., Truhlar, D. G., Elovitz, M. S. and Weber, E. J., "Factors Controlling Regioselectivity in the Reduction of Polynitroaromatics in Aqueous Solution," *Environ. Sci. Technol.*, **1996**, (30), 3028-3038.

217. Marenich, A. V., Cramer, C. J. and Truhlar, D. G., "Universal Solvation Model Based on Solute Electron Density and a Continuum Model of the Solvent Defined by the Bulk Dielectric Constant and Atomic Surface Tensions," *J. Phys. Chem. B*, **2009**, (113), 6378-6396.

218. Hofstetter, T. B., Neumann, A., Arnold, W. A., Hartenbach, A. E., Bolotin, J., Cramer, C. J. and Schwarzenbach, R. P., "Substituent Effects on Nitrogen Isotope Fractionation During Abiotic Reduction of Nitroaromatic Compounds," *Environ. Sci. Technol.*, **2008**, (42), 1997-2003.

219. Cramer, C. J., *Essentials of Computational Chemistry: Theories and Models*, John Wiley & Sons, Chinchester, 2004.

220. Tissandier, M. D., Cowen, K. A., Feng, W. Y., Gundlach, E., Cohen, M. H., Earhart, A. D., Coe, J. V. and Tuttle, T. R., "The Proton's Absolute Aqueous Enthalpy and Gibbs Free Energy of Solvation from Cluster-Ion Solvation Data," *J. Phys. Chem. A*, **1998**, (102), 7787-7794.

221. Camaioni, D. M. and Schwerdtfeger, C. A., "Comment on “Accurate Experimental Values for the Free Energies of Hydration of H+, OH-, and H3O+”," *J. Phys. Chem. A*, **2005**, (109), 10795-10797.

222. Kelly, C. P., Cramer, C. J. and Truhlar, D. G., "Aqueous Solvation Free Energies of Ions and Ion–Water Clusters Based on an Accurate Value for the Absolute Aqueous Solvation Free Energy of the Proton," *J. Phys. Chem. B*, **2006**, (110), 16066-16081.

223. Bryantsev, V. S., Diallo, M. S. and Goddard III, W. A., "Calculation of Solvation Free Energies of Charged Solutes Using Mixed Cluster/Continuum Models," *J. Phys. Chem. B*, **2008**, (112), 9709-9719.

224. Winget, P., Cramer, C. J. and Truhlar, D. G., "Computation of Equilibrium Oxidation and Reduction Potentials for Reversible and Dissociative Electron-Transfer Reactions in Solution," *Theor. Chem. Acc.*, **2004**, (112), 217-227.

225. M. J. Frisch, G. W. Trucks*, et al.*, *Gaussian09*, Gaussian Inc., Wallingford CT 2009.

226. Cavka, J. H., Jakobsen, S., Olsbye, U., Guillou, N., Lamberti, C., Bordiga, S. and Lillerud, K. P., "A New Zirconium Inorganic Building Brick Forming Metal Organic Frameworks with Exceptional Stability," *J. Am. Chem. Soc.*, **2008**, (130), 13850-13851.

227. Wu, H., Yildirim, T. and Zhou, W., "Exceptional Mechanical Stability of Highly Porous Zirconium Metal–Organic Framework UiO-66 and Its Important Implications," *J. Phys. Chem. Lett.*, **2013**, (4), 925-930.

228. Mondloch, J. E., Katz, M. J., Planas, N., Semrouni, D., Gagliardi, L., Hupp, J. T. and Farha, O. K., "Are Zr6-based MOFs water stable? Linker hydrolysis vs. capillary-force-driven channel collapse," *Chem. Comm.*, **2014**, (50), 8944.

229. Mondloch, J. E., Bury, W., Fairen-Jimenez, D., Kwon, S., DeMarco, E. J., Weston, M. H., Sarjeant, A. A., Nguyen, S. T., Stair, P. C., Snurr, R. Q., Farha, O. K. and Hupp, J. T., "Vapor-Phase Metalation by Atomic Layer Deposition in a Metal–Organic Framework," *J. Am. Chem. Soc.*, **2013**, (135), 10294-10297.

230. Planas, N., Mondloch, J. E., Tussupbayev, S., Borycz, J., Gagliardi, L., Hupp, J. T., Farha, O. K. and Cramer, C. J., "Defining the Proton Topology of the Zr6-Based Metal–Organic Framework NU-1000," *J. Phys. Chem. Lett.*, **2014**, (5), 3716-3723.

231. Kickelbick, G., Wiede, P. and Schubert, U., "Variations in capping the Zr6O4(OH)(4) cluster core. X-ray structure analyses of [Zr-6(OH)(4)O-4(OOC-CH=CH2)(10)](2)(mu-OOC-CH=CH2)(4) and Zr-6(OH)(4)O-4(OOCR)(12)(PrOH) (R = Ph, CMe = CH2)," *Inorg Chim Acta*, **1999**, (284), 1-7.

232. Bandosz, T. J., Laskoski, M., Mahle, J., Mogilevsky, G., Peterson, G. W., Rossin, J. A. and Wagner, G. W., "Reactions of VX, GD, and HD with Zr(OH) 4: Near Instantaneous Decontamination of VX," *J. Phys. Chem. C*, **2012**, (116), 11606-11614.

233. Rai, N. and Siepmann, J. I., "Transferable Potentials for Phase Equilibria. 9. Explicit Hydrogen Description of Benzene and Five-Membered and Six-Membered Heterocyclic Aromatic Compounds," *J. Phys. Chem. B*, **2007**, (111), 10790-10799.

234. Parkin, G., "Synthetic Analogues Relevant to the Structure and Function of Zinc Enzymes," *Chem Rev*, **2004**, (104), 699-768.

235. Wang, S., Bromberg, L., Schreuder-Gibson, H. and Hatton, T. A., "Organophophorous Ester Degradation by Chromium(III) Terephthalate Metal–Organic Framework (MIL-101) Chelated to N, N-Dimethylaminopyridine and Related Aminopyridines," *ACS Appl. Mater. Interfaces*, **2013**, (5), 1269-1278.

236. Dang, D., Bai, Y., He, C., Wang, J., Duan, C. and Niu, J., "Structural and Catalytic Performance of a Polyoxometalate-Based Metal–Organic Framework Having a Lanthanide Nanocage as a Secondary Building Block," *Inorg Chem*, **2010**, (49), 1280-1282.

237. Peterson, G. W. and Wagner, G. W., "Detoxification of chemical warfare agents by CuBTC," *J Porous Mater*, **2013**, (21), 121-126.